AD-A277 903

‖‖‖‖‖‖‖‖‖‖‖

The Pennsylvania State University
APPLIED RESEARCH LABORATORY
P.O. Box 30
State College, PA 16804

LASER PROCESSING OF DISCONTINUOUSLY
REINFORCED ALUMINUM COMPOSITES

by

K. C. Meinert, Jr.
R. B. Bhagat
R. P. Martukanitz

DTIC
S ELECTE
APR 0 7 1994
E **D**

Technical Report No. TR 94-02
March 1994

94-10563

‖‖‖‖‖‖‖‖‖‖‖‖‖‖‖

L.R. Hettche, Director
Applied Research Laboratory

94 4 6 089

REPORT DOCUMENTATION PAGE

1. AGENCY USE ONLY (Leave blank)	2. REPORT DATE March 1994	3. REPORT TYPE AND DATES COVERED

4. TITLE AND SUBTITLE

Laser Processing of Discontinuously Reinforced Aluminum Composites

5. FUNDING NUMBERS

6. AUTHOR(S)

K. C. Meinert, Jr., R. B. Bhagat, R. P. Martukanitz

7. PERFORMING ORGANIZATION NAME(S) AND ADDRESS(ES)

Applied Research Laboratory
P. O. Box 30
State College, PA 16804

8. PERFORMING ORGANIZATION REPORT NUMBER

TR-94-02

9. SPONSORING/MONITORING AGENCY NAME(S) AND ADDRESS(ES)

Space and Naval Warfare Systems Command
2451 Crystal Drive
Arlington, VA 22245-5200

10. SPONSORING/MONITORING AGENCY REPORT NUMBER

N00039-92-C-0100

11. SUPPLEMENTARY NOTES

12a. DISTRIBUTION/AVAILABILITY STATEMENT

Unlimited

12b. DISTRIBUTION CODE

13. ABSTRACT (Maximum 200 words)

Discontinuously reinforced aluminum (DRA) composites have attractive potential as engineering materials due to the combination of good mechanical properties and relatively low cost; however utilization of these composites requires improved machining and joining procedures. In this study, the feasibility of laser cutting and laser beam welding of DRA composites was investigated. It was found that the DRA composites could be cut at rates faster than that of unreinforced aluminum. The SiC and Al_2O_3 reinforcement materials absorbed more energy than the monolithic aluminum at the CO_2 laser beam wavelength of 10.6 μm. The improved energy absorption leads to an increase in laser cutting rates and greater weld penetration over unreinforced aluminum, except in the case of silicon carbide whisker reinforced composites. The formation of aluminum carbide and the difficulties in removing the viscous dross lead to a lower cutting rate than of unreinforced aluminum. The focus of the laser beam welding experimentation dealt with eliminating the formation of aluminum carbide by filler metal additions. Appropriate filler metals and their respective carbides were analyzed for thermodynamic stability and compatibility in the weld. A computer program that determines the equilibrium of chemical systems was employed to predict the amount of titanium necessary to prevent the formation of aluminum carbide in the fusion zone of a Al/SiC/20 composite. The analysis determined that a 22 wt% addition of titanium to the fusion zone was necessary to prevent the formation of aluminum carbide. Titanium and zirconium shims were placed between two thin plates of a 6061/SiC/20w composite and were laser beam welded to produce welds having filler metal additions. The laser beam welds were analyzed by electron probe microanalysis (EPMA) and optical microscopy. The analysis showed the titanium and zirconium additions successfully prevented the formation of aluminum carbide in the fusion zone. A comparison of the results of microstructure observed in the experimental welds indicated that the computer predictions for the level of filler metal addition to the fusion zone were reasonably accurate.

14. SUBJECT TERMS

laser processing, composites, reinforced aluminum, machining joining, cutting welding, DRA

15. NUMBER OF PAGES

113

16. PRICE CODE

17. SECURITY CLASSIFICATION OF REPORT	18. SECURITY CLASSIFICATION OF THIS PAGE	19. SECURITY CLASSIFICATION OF ABSTRACT	20. LIMITATION OF ABSTRACT
Unclassified	Unclassified	Unclassified	Unlimited

TABLE OF CONTENTS

Accesion For		
NTIS CRA&I	X	
DTIC TAB	☐	
Unannounced	☐	
Justification		
By		
Distribution /		
Availability Codes		
Dist	Avail and / or Special	
A-1		

LIST OF TABLES

LIST OF FIGURES

Chapter 1

INTRODUCTION

Metal matrix composites (MMCs) have attractive potential as engineering materials because of the improved mechanical performance over unreinforced metals. Some of the properties include: increased strength, stiffness, and improved wear resistance, and high temperature performance. Despite improved properties, the materials generally have lower ductility and fracture toughness in comparison to the unreinforced matrix. The DRA composites are attractive materials because they combine good mechanical properties, the ability to be formed by standard metalworking techniques, and lower cost than continuous fiber reinforced MMCs. Although most applications to date have been in the aerospace industry, new applications are being found, particularly in the automotive industry [1, 2]. Utilization of these materials will require machining and welding processes that, as yet, have not been fully investigated. The properties of DRA composites often make machining and joining difficult to achieve by the processes commonly used for aluminum.

Difficulties in machining can be attributed to the hardness of the reinforcement. The hardness of the reinforcement is often greater than that of the cutting tools used for contact machining methods, such as drilling and milling. Laser cutting offers an advantage, as it is a non-contact process it is unaffected by the hardness of the material. One of the factors that determines the effectiveness of laser processing is the absorptivity of the material. It has been found that DRA composites absorb more energy than unreinforced aluminum. The improved energy absorption is attributable to the higher energy absorption of the silicon carbide and aluminum oxide reinforcement. Laser beam welding offers the advantages of lower overall heat input, narrower heat affected zones, faster cooling rates, and faster welding rates than most conventional welding processes, such as arc welding.

The objective of this investigation was to determine the feasibility of laser processing of selected DRA composites. The experimentation on laser cutting involved determining the parameters and the effects of cutting on the composites. Cutting rates for the different composites were determined and cuts were characterized by microstructural analysis and microhardness. A comparison of the laser cutting rate to the calculated absorptivity of the composites was developed. Laser beam welds were made on the materials without the use of filler metal (autogenous) to determine the effects on the material. A comparison of the weld penetration depth to the calculated absorptivity was generated. The focus of the laser beam welding investigation however; was the prevention of the formation of aluminum carbide during welding of silicon carbide reinforced aluminum composites. In the interest of preventing aluminum carbide formation, titanium and zirconium can be used. These two metals form carbides that are more thermodynamically stable than aluminum carbide based on free energy. The SOLGASMIX computer program, used to determine the chemical equilibrium of a system, was used to predict the amount of titanium necessary to prevent formation of aluminum carbide in the fusion zone of the weld. Titanium and zirconium were added to the fusion zone of a 6061/SiC/20w composite weld to prevent the formation of aluminum carbide through the formation of the more stable carbide compounds.

Chapter 2 presents a review of the relevant literature on laser processing of the composites. In addition to this, difficulties involved with cutting and joining of DRA composites are discussed. The processes, equipment, and materials used for the experimental work will be discussed in Chapter 3, followed by the results of the experimentation and discussion in Chapter 4. The conclusions of the investigation will be given in Chapter 5. Finally, Chapter 6 includes recommendations for future work in the area of laser processing of metal matrix composites.

Chapter 2
LITERATURE REVIEW

The interest in DRA composites has led to a significant amount of research for these materials. This research has led to an increased understanding of the effects of the constituent materials, fabrication procedures, and secondary processing on the mechanical properties. Early DRA composites used standard wrought alloys with good properties, such as 6061 and 2024. Microstructural and chemical analysis of the composites often found that large intermetallic particles contributed to composite failure [3]. The intermetallic particles were attributed to the high solute concentrations of standard wrought alloys that were used for the matrix [4]. The problems associated with the formation of these intermetallic particles has led to the development of new matrices, such as 2009, X2080, and 6090, which are designed specifically for composites [5]. The use of new matrix alloys has resulted in improved ductility and fracture toughness of the composites through the elimination of the brittle intermetallic particles [3]. Improvements in ductility and fracture toughness have also been achieved through secondary processing techniques such as rolling and extrusion [4, 6]. The improvements observed after secondary processing have been attributed to increased homogeneity in the microstructure. Research is currently improving the properties offered by DRA composites; however many obstacles must be overcome to enable wide utilization of these materials. These obstacles include the development of effective cutting and welding techniques.

2.1. Cutting and Machining

The high hardness of the reinforcing phases used in DRA composites has been a prominent technical challenge for the processing of these materials. Standard metalworking techniques, such as extrusion, rolling, superplastic forming, and forging have been demonstrated [7-10]; however the hardness of the reinforcement has required modifications to many of these processes. The reinforcements commonly used rival or exceed the hardness of most common cutting tools. To effectively machine and cut DRA composites ultra hard materials, such as polycrystalline diamond or cubic boron nitride tools, are required [11]. The use of non-traditional and non-contact techniques such as abrasive waterjets [12] and lasers [13] have been shown to be effective in cutting metal matrix composites.

2.2. Welding

Interactions between molten matrix and the reinforcing phase have lead to difficulties during fusion welding of DRA composites. These difficulties include: an increase in the weld pool viscosity, porosity in the welds, dewetting of the reinforcement, and chemical reactions between the reinforcement and the matrix.

The increased viscosity of the weld pool occurs because the reinforcements, which are usually ceramic, generally remain solid during welding. The presence of the solid reinforcement in the molten metal results in an increase in viscosity [14, 15]. The increased viscosity creates a sluggish weld pool which may lead to a rough weld bead, porosity within the weld, or lack of fusion.

Powder metallurgy (P/M) fabrication methods can also contribute to porosity often observed in the fusion and heat affected zones of welded DRA composites [16, 17]. One step of the P/M fabrication process (for monolithic aluminum alloys or DRA composites) is

a heating/degassing cycle. This preparation is necessary to remove water that is chemically bound to the aluminum and that is adsorbed by the reinforcement, in addition to any additives used during the mixing and compaction steps. For the water that is chemically bound to the aluminum powder, the chemical reactions that occur during heating are shown in Table 1 [18].

Table 1. Chemical Reactions Occurring During Heating of Aluminum Powders [18].

Reaction			Temperature
$2Al + 6H_2O$	$\rightarrow$	$Al_2O_3 \cdot 3H_2O + 3H_2(g)$	
$Al_2O_3 \cdot 3H_2O$	$\rightarrow$	$Al_2O_3 \cdot H_2O + H_2O$ [sic]	$> 100^\circ$ C
$2Al + 3H_2O$	$\rightarrow$	$Al_2O_3 + 3H_2(g)$	$> 200^\circ$ C
$Al_2O_3 \cdot H_2O$	$\rightarrow$	$Al_2O_3 + H_2O$	$> 400^\circ$ C

The degassing cycles used are very complex and sensitive to many aspects of the powder mixture, including surface chemistry of both the reinforcement and the aluminum [18]. As a result it is unlikely that all the water and other additives are fully removed during the cycle. It has been observed that the porosity evident in the welds made on P/M aluminum alloys has decreased as improvements have been made to fabrication processes of the material [19]. Degassing experiments on a 6061/SiC/15w and 6061/SiC/20w composite showed that the primary gas emanating from the composite was molecular hydrogen at temperatures between 650 to 670°C and greater [16]. Analysis for a 6061 Al sample produced in the same manner as the composite indicated that the aluminum is the source of the hydrogen, not the silicon carbide or any reaction between reinforcement and matrix. Studies by Ahearn [16] suggest that the rapid heating of the material during welding results in pore formation, because there is little time for the hydrogen to diffuse from the material. Porosity can also be problem for cast aluminum alloys, as molten aluminum has a relatively

high solubility for hydrogen [20]. As a result, gas porosity can occur in the casting if the melt is not properly fluxed.

In addition to the problems related to porosity are the problems associated with wettability [21]. Most ceramic reinforcements are not wet by molten metals. This requires the use of techniques during fabrication to promote wetting. When the composite is melted, the matrix may reject the reinforcement, thereby reducing the reinforcement. To alleviate the problem, filler alloys containing additions that promote wetting are generally used [14]. It has been determined that magnesium can prevent dewetting of the aluminum oxide particles during arc welding of 6061/Al$_2$O$_3$p composites [22, 23]. The use of filler metals may be necessary for welding; however, the added metal dilutes the amount of reinforcement in the weld pool. The reduction in the volume fraction of the reinforcement lowers the mechanical properties of the weld when compared to the base material.

Chemical reactions between the matrix or alloying additions and the reinforcement are also possible during welding. The chemical reaction between molten aluminum and silicon carbide to form a deleterious aluminum carbide during fusion joining of Al/SiC composites has been widely documented [16, 24-30]. The formation of aluminum carbide has been the major obstacle when welding silicon carbide reinforced aluminum composites. The formation of aluminum carbide interferes with the welding process, changes the composition of the weld, and results in poor weld properties. Molten aluminum reportedly reacts with the silicon carbide resulting in the formation of aluminum carbide and silicon by the following reaction [16, 24-31].

$$4Al + 3SiC \rightarrow Al_4C_3 + 3Si \tag{1}$$

The reaction has been found to occur rapidly [16, 31], and affects the welding process and the properties of the joint. This reaction results in a substantial increase in the viscosity of the weld pool. Increased viscosity interferes with the welding process by inhibiting the

formation of an adequate joint. The silicon produced in the reaction changes the chemical composition of the weld with respect to the base material. Although some of the silicon will go into solution with aluminum, the presence of free silicon in the fusion zone microstructure is quite common [24-30]. The high hardness and strength of a carbide can provide improvements in properties (as silicon carbide does in aluminum); however, the morphology and the mechanical and chemical properties of aluminum carbide phase impact the engineering properties of the weld. Aluminum carbide forms large platelets within the fusion zone. These brittle aluminum carbide platelets lead to the failure of the joint at low strains. Because of its low density, the formation of aluminum carbide (by reaction 1) results in a twenty-five percent increase over the initial volume. This increase in volume is most likely responsible for the excessive weld crown often observed in welds. In the presence of water or even moist environments, the aluminum carbide platelets decompose, creating voids within the weld. Aluminum carbide reacts with water, producing methane and aluminum hydroxide by following reaction [32].

$$Al_4C_3 + 12H_2O \rightarrow 4Al(OH)_3 + 3CH_4 \qquad (2)$$

One method of suppressing the formation of aluminum carbide during welding and fabrication of DRA composites is the use of silicon additions. Research by Isaikin et al. [33] provided one the first analyses of the reaction between aluminum and silicon carbide, resulting in an equation for the free energy of the reaction and its relationship to the activity of silicon and temperature. The relation shows that the formation of aluminum carbide is favored when silicon levels are low and temperatures are high. Iseki et al. [34] provided experimental verification for the suppression of aluminum carbide by silicon additions in a study on joining aluminum to silicon carbide. In the study, two types of silicon carbide, one containing free silicon and one containing no free silicon, were joined to aluminum. Characterization showed that aluminum carbide formed at the joint between the aluminum

and silicon carbide containing no free silicon. In contrast, the free silicon present in the other silicon carbide sample prevented the formation of aluminum carbide at the joint. Thermodynamic control of the formation of aluminum carbide by silicon has led to fabrication of castable silicon carbide reinforced aluminum composites by ingot metallurgy techniques [35]. The levels of silicon necessary to prevent the formation of aluminum carbide are provided by aluminum casting alloys. A study by Lloyd [31] determined the amount of silicon that must be present to prevent the formation of aluminum carbide as a function of temperature. At 600°C, approximately 8 atomic percentage of silicon necessary to prevent the formation of aluminum carbide; the amount increases linearly to approximately 13 atomic percentage at 850°C. Lloyd [31] also determined that the amount of aluminum carbide formed increases with higher temperatures and longer contact time between the aluminum and silicon carbide. If the formation of aluminum carbide does occur, a substantial increase in the viscosity results, which can prevent casting of the composite [15, 31, 35]. Arc welding of the materials without the formation of aluminum carbide is possible provided the heat input to the weld is kept sufficiently low [14]. The use of filler alloys containing silicon is recommended during arc welding processes to inhibit formation of aluminum carbide [14]. Silicon additions are commonly used to suppress the formation of aluminum carbide in Al/SiC composites; however the addition of other metals has also be shown to prevent the formation of aluminum carbide.

One area of metallurgy that has provided information for the prevention of aluminum carbide formation is the grain refinement of aluminum alloys. Grain refiners, such as titanium diboride, are often added to aluminum castings to provide improved performance by controlling the grain structure. Several transitional metals, in particular titanium, zirconium and niobium, are able to refine the grain structure of aluminum alloys by the formation of carbides that act as nucleation sites [36]. Thermodynamic analysis and microstructural observations for the addition of titanium to aluminum for grain refinement

have shown that titanium carbide is more stable than either aluminum carbide or titanium aluminide (TiAl$_3$) [37-41]. Studies of the Al-Ti-C system by Jarfors, Fredricksson, and Froyen [38] have shown that although several compounds can form in the system (Al$_4$C$_3$, TiAl$_3$, Ti$_2$AlC, and TiC), for the levels of titanium studied ($\leq$6 wt%), TiC is the most stable compound. The thermodynamic stability of the titanium carbide phase and its ability to act as a strengthening phase has been used for in-situ fabrication of composites. A process developed by Sahoo and Koczak [42] forms titanium carbide particulates up to 2 μm in size in an aluminum alloy matrix. Characterization and testing of the material demonstrated that the TiC particulates were more stable than either Al$_4$C$_3$ or TiAl$_3$ up to at least 750°C. Titanium and zirconium have also been used in joining silicon carbide reinforced aluminum composites by a low pressure plasma coating process [43]. A powder mixture containing silicon carbide particles, aluminum, and small amount of either titanium or zirconium was used to join 1100 Al-30 wt% SiCp composites. Electron probe micro-analysis (EPMA) of the welds showed that the titanium and zirconium reacted with the surface of the silicon carbide particle, forming a thin layer of the respective carbide. Due to the thermodynamic stability, the TiC and ZrC formed a barrier layer prevented the formation of aluminum carbide. EPMA of the joints determined that no aluminum carbide was present in the welds.

2.3. Laser Theory

Laser is an acronym for light amplification by stimulated emission of radiation. The laser has become a valuable tool in many areas of science due to its unique properties. Lasers are a source of intense, collimated, monochromatic light that can be focused to obtain a high energy density [44]. One of the fundamental principles of the laser is the theory of stimulated emission, proposed by Einstein in 1916 [45]. The theory of

stimulated emission is too complex to be discussed here; however, a simplified version can be explained in Figures 1 and 2. Consider an atom (or molecule) in an excited energy level. The excited atom will emit a photon as it undergoes a transition to a lower energy level. In this case, known as a spontaneous emission, the excited atom emits a photon as it moves to a lower energy level, Figure 1. If an emitted photon passes close enough to a second excited atom (or molecule), the spontaneously emitted photon can stimulate the excited atom to release a photon, Figure 2. The stimulated photon has the same energy, phase, polarization, and travels in the same direction as the stimulating photon.

The theory of stimulated emission was proposed in 1916; however, it was not until 1960 that the theory was reduced to practice [45]. Several requirements are necessary to obtain a laser beam [44]. The first requirement is the atom or molecule capable of photon emission, known as the lasing medium. Also necessary is a means of exciting the lasing medium to higher energy levels. An optical resonator reflects the photons through the lasing medium so that stimulated emission can be sustained. A lasing medium (CO_2), means of excitation (DC current), and the mirrors that make up the optical resonator for a carbon dioxide laser can be seen in Figure 3.

When in the excited state, the CO_2 molecule will emit photons spontaneously in random directions, Figure 4.1. Due to the large number of emissions, one (or more) of the photons will travel down the axis of the optical resonator. This photon(s) will initiate the laser beam by starting the process of stimulated emission, Figure 4.2. The photons will resonate between the two mirrors, stimulating other excited CO_2 molecules to release photons, Figure 4.3. The process continues, each stimulated photon becoming a stimulating photon, until the photons exit the partially reflective mirror, forming a laser beam, Figure 4.4.
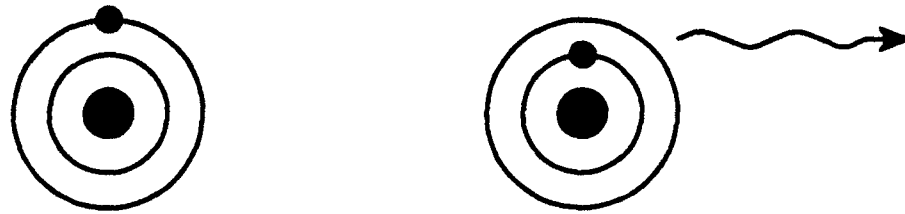
Figure 1. Spontaneous emission of a photon due to the transition of an electron to a lower energy state.

Figure 2. Incoming photon stimulating the emission of a photon from an excited atom.
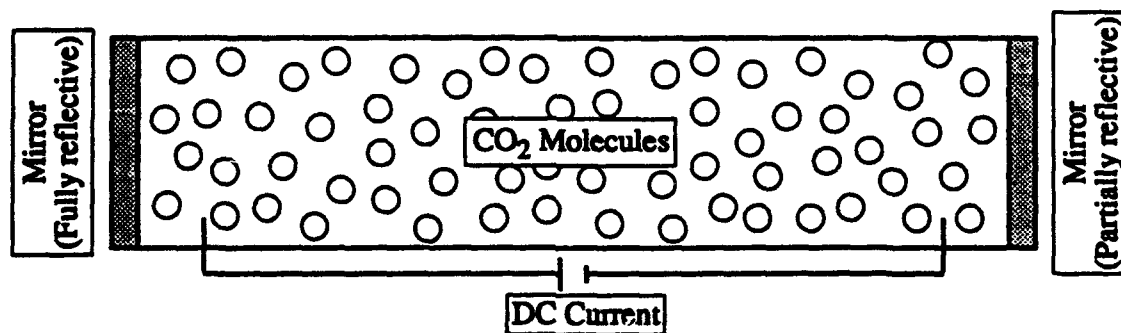
Figure 3. Lasing medium, means of excitation, and optical resonator for a CO_2 laser.
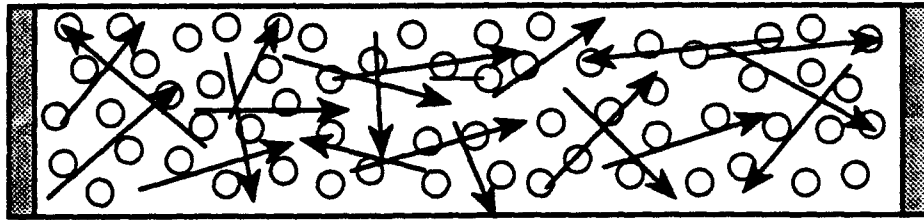
Figure 4.1. Spontaneous emission of photons from the excited carbon dioxide molecules.
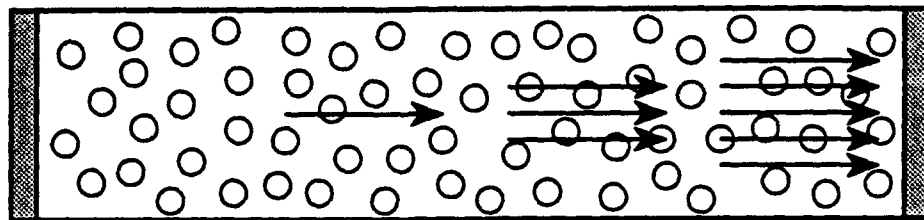
Figure 4.2. Photon traveling down the axis of the resonator.
Initiation of the process of stimulated emission.
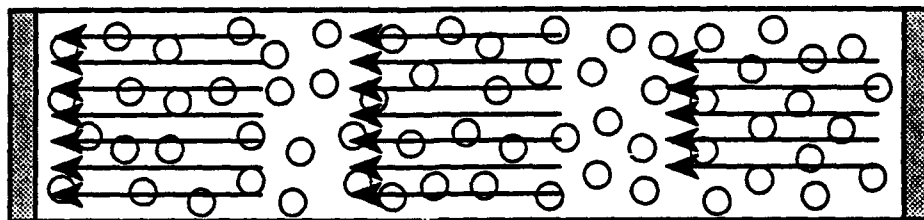
Figure 4.3. Resonance between the two mirrors, stimulating emission of more photons.
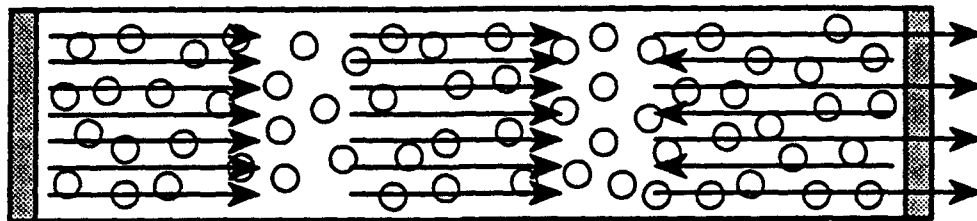
Figure 4.4. Sufficient number of photons to exit the partially reflective mirror.
The photons not emitted continue the process by stimulating more photons.

2.4. Laser Processing

Lasers are useful for materials processing because of the variety of processing techniques available and the ability to process many different types of materials. The processes offered by lasers include: cutting, drilling, welding, cladding, and surface treatment [46]. The materials that can be processed include: metals, ceramics, plastics, and composites.

Laser beam welding involves the use of a focused laser beam to cause localized melting in the material. Two different type of welds can be formed depending on the intensity of the laser beam. The first type of weld, known as a conduction weld, occurs when the incident laser energy is conducted away from the surface of the material. In this condition the penetration depth for metals is limited to about 1 mm [44]. The second type of weld, known as a keyhole weld, is achieved by lasers capable of generating high power densities, usually those greater than 1000 W. The high energy density vaporizes the material, generating plasma and creating a cavity in the material. Once formed, the plasma keyhole absorbs almost all the incident laser energy. The temperatures within the keyhole are extremely high, approaching 20,000 K [46]. The depth of the keyhole is a function of power; for a constant beam diameter the depth generally increases with increasing laser power [47]. During the laser beam welding process, a shielding gas is usually supplied to protect the weld, to prevent the absorption of gases, prevent unwanted chemical reactions, and to aid the welding process [48]. As the laser beam is moved across the material, the molten metal flows behind the beam and solidifies, forming the weld as shown in Figure 5. Laser beam welding offers several advantages over conventional welding processes, including; non-contact welding, low overall heat input, narrow fusion and heat affected zones, faster cooling rates, and faster welding rates [46-48]. Disadvantages of laser beam welding include; high equipment cost, and limited thickness in comparison to electron beam

welding [47]. Additionally, the high temperatures in the keyhole can result in the loss of volatile alloying additions [24].

Much like laser beam welding, laser cutting is also a useful process because of the fast rate, limited part distortion, minimal heat affected zone, and narrow kerf in comparison to most cutting methods [46]. As mentioned previously, the high equipment cost is a disadvantage of laser cutting. Laser cutting of materials is similar to laser beam welding in the keyhole mode. The focused laser beam causes localized melting of the material and assist gas, usually applied coaxial to the beam, expels the molten material prior to solidification, as shown in Figure 6. The primary role of the assist gas in laser cutting is to remove the molten material, but it may also enhance cutting by promoting oxidation reactions or prevent reactions by providing a gas shield [49]. Oxidation reactions tend to increase the heat in the material, causing more melting and a decrease the material viscosity, leading to faster properties of the material.

The amount of laser energy absorbed by the material is one factor that determines the effectiveness of laser processing [47]. The laser is a light source, so the amount of energy transferred to the workpiece depends on the amount of light absorbed by the workpiece. In general, improved absorptivity leads to greater processing efficiency, which allows for deeper penetration and faster processing speeds. The amount of energy absorbed by a material, measured by emissivity, is dependent on the optical properties of the material that vary as a function of the wavelength of the light and temperature. Emissivity is a function of wavelength; therefore the amount of energy absorbed will be dependent on the output wavelength of the laser. For example, the emissivity of aluminum at the operating wavelength of a CO_2 laser (10.6 μm) is 1.9 percent, and 8 percent for the operating wavelength of a Nd:YAG laser (1.06 μm) [50]. In general, metals absorb small amounts of energy, because they are very reflective. Aluminum in particular, has a very high reflectivity, as shown by the low emissivity for the wavelengths of the CO_2 and

Nd:YAG lasers. Ceramic materials usually have higher absorptivities than do metals [49].

The improved absorptivity of ceramics is an important consideration for laser processing of

DRA composites. Several researchers [28, 51] have observed an increase in the amount of

laser energy absorbed by DRA composites that has be attributed to the higher absorption of

laser energy by the ceramic reinforcement. Several other factors can affect the amount of

laser energy absorbed. Alloying additions have been shown to affect the amount of laser

energy absorbed by aluminum alloys for both the CO_2 and Nd:YAG lasers [52]. Surface

conditions can also be a factor for energy absorption, since more energy is reflected from a

highly polished surface than from a rougher one [53].
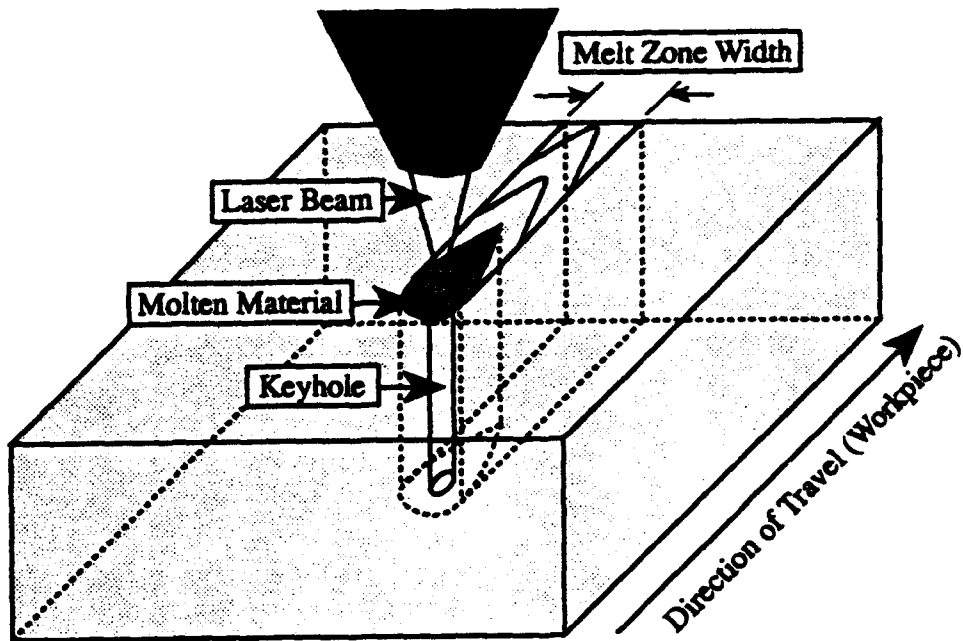
Figure 5. Schematic diagram for laser beam welding of a material.
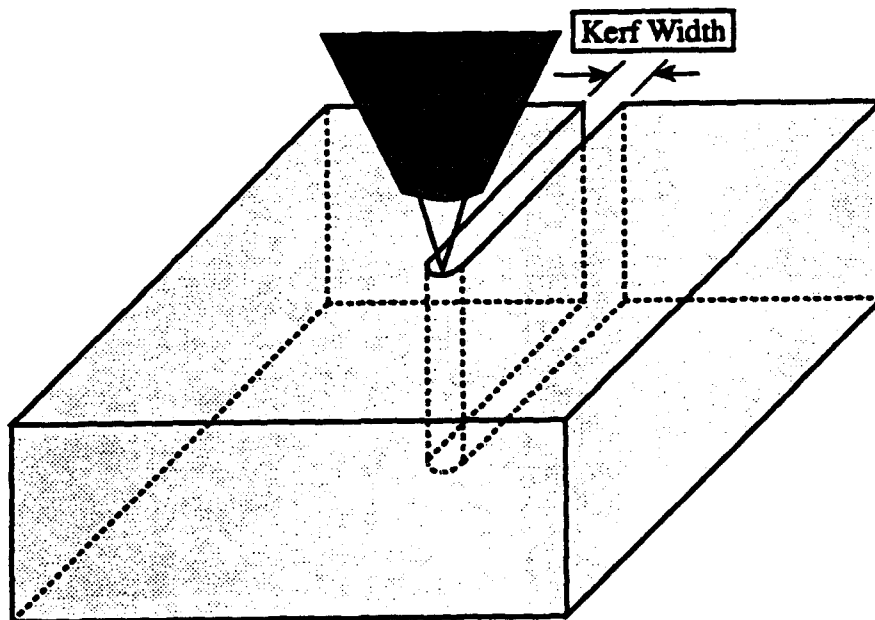
Figure 6. Schematic diagram for laser cutting of a material.

Chapter 3

EXPERIMENTAL WORK

3.1. Materials

Several different DRA composites were used in the investigation. The composites used varied in matrix alloy, composition and morphology of the reinforcement, method of fabrication, secondary processing, and heat treatment as shown in Table 2.

Table 2. Materials Used in the Experimentation and Relevant Material Data.

Material	Form	Heat Treatment	Fabrication Technique
6061/Al$_2$O$_3$/20p	Extrusion	As Extruded	Ingot Processing
6061/SiC/20w	Extrusion	As Extruded	Powder Metallurgy
X2080/SiC/15p	1.6 mm sheet	T6 Temper	Powder Metallurgy
A356/SiC/20w	Sheet	As Cast	Tape Cast Preform: HiPIC
A356/SiC/20p	Plate	As Cast	Ingot Metallurgy
6061	Sheet	T6 Temper	Ingot Metallurgy

The A356/SiC/20w composite was made in-house at the Applied Research Laboratory. Silicon carbide whisker preforms were fabricated by tape casting and were subsequently infiltrated using high pressure infiltration casting (HiPIC). The developed preform fabrication process starts by mixing measured amounts of silicon carbide whiskers, an organic binder, and solvent to form a homogenous slurry. A thin layer of the slurry is applied to a plastic carrier by means of a tape casting machine. The slurry dries on the carrier forming a green tape. The green tape is then cut and stacked in a die, as shown in Figure 7.
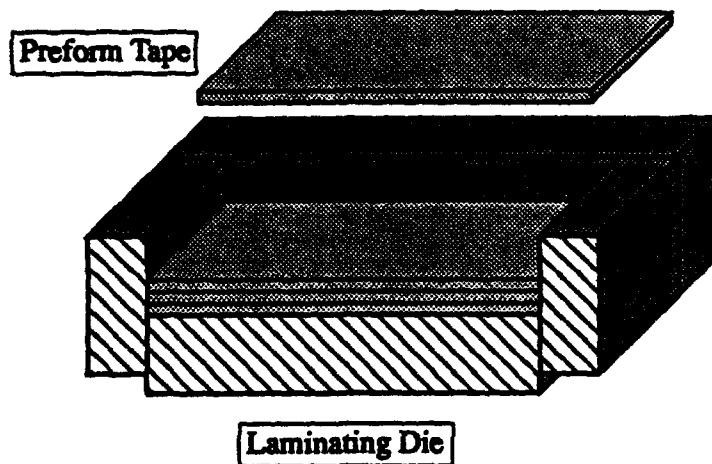
Figure 7. Schematic drawing of the laminating die for fabrication of silicon carbide whisker preforms by tape casting.

Heat and pressure are applied to the tape layers to consolidate the tapes into a green preform. The organic binder is then removed from the green preform by a heating cycle, completing the preform fabrication process.

High pressure infiltration casting is used to infiltrate the silicon carbide whisker preform, forming the composite. The preform is placed into a metal die. Molten aluminum is then poured over the preform. Pressure is applied immediately to infiltrate the preform and rapidly solidify the aluminum, forming the composite.

3.2. Equipment

A Coherent General EFA S51, 1.5 kW, enhanced fast axial flow CO_2 laser was used during the investigation. The laser has continuous wave (CW) and pulsed capability in the TEM_{00} mode with a circular polarized beam. A focal arrangement utilizing a 63.5 mm focal length lens produced a spot size of 120 μm at an output wavelength of 10.6 μm. Shielding and assist gases were provided coaxial to the beam, and a computer controlled micro-positioning system was employed to manipulate the test specimens during processing. The experimental arrangement used for the laser cutting and laser beam welding investigation is shown schematically in Figure 8.

3.3. Processes

Laser cuts were made on the composites and aluminum alloy 6061 to determine the cutting rates for the material. Thin sections ($\approx$ 1-4 mm) were cut from the parent extrusion using an abrasive cut-off wheel. Prior to laser cutting all the samples were sanded with 320 grit silicon carbide paper and were subsequently cleaned with acetone to provide uniform surface roughness for testing. Aluminum alloy 6061 was laser cut to provide a

comparison of the cutting rate of aluminum to the rate of the composites. Air, nitrogen, and oxygen were used as assist gases during cutting. The A356/SiC/20p composite was not used in the laser cutting experimentation.

Samples for laser beam welding were prepared in the same manner as the laser cutting samples. For the additions of filler metals to the 6061/SiC/20w composite, the edges of the composite were also sanded using 320 grit silicon carbide paper and cleaned with acetone. The filler metal was cut to fit the sample, was sanded, cleaned with acetone, and placed between the edges of the composite on the welding fixture, as shown in Figure 9. Clamps were then attached, as shown by the arrows in the figure, to prevent the composite plates from moving during welding and to keep the plates and filler metal in intimate contact. Helium was supplied at a flow rate of 25 cubic feet per hour (CFH) to protect the materials during welding.

The cuts and welds were mounted and polished to 1 μm grit using standard techniques to obtain samples for characterization. Optical and scanning electron microscopes were used to characterize the microstructure. An electron microprobe was used for elemental analysis and x-ray mapping. Microhardness of the cuts and welds was determined using a Vicker's indentor.
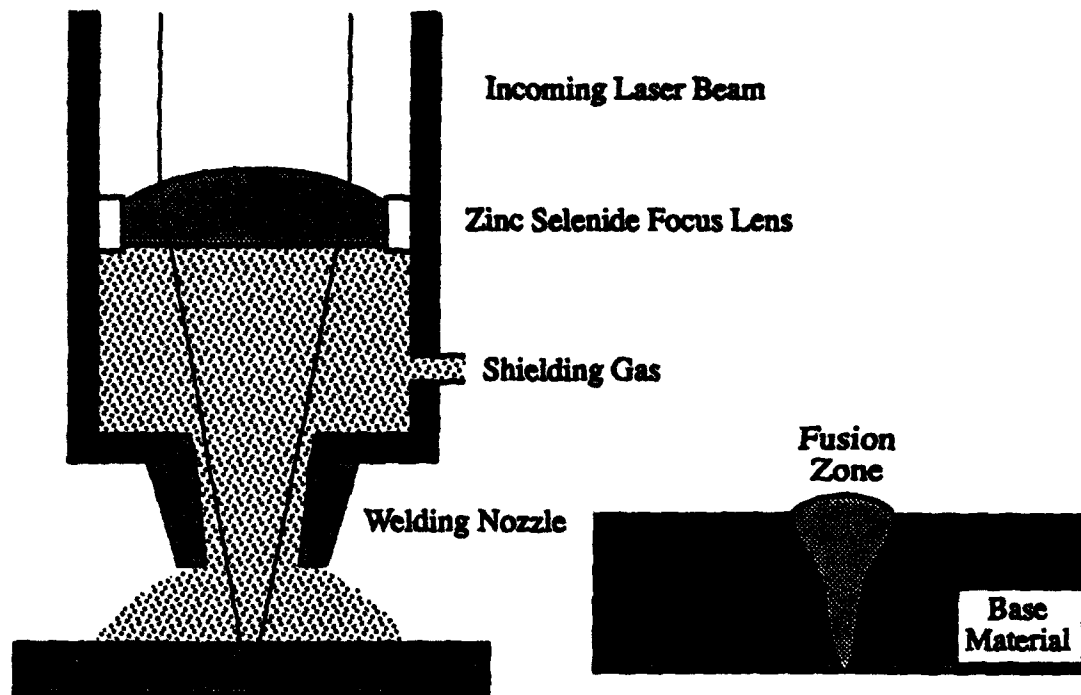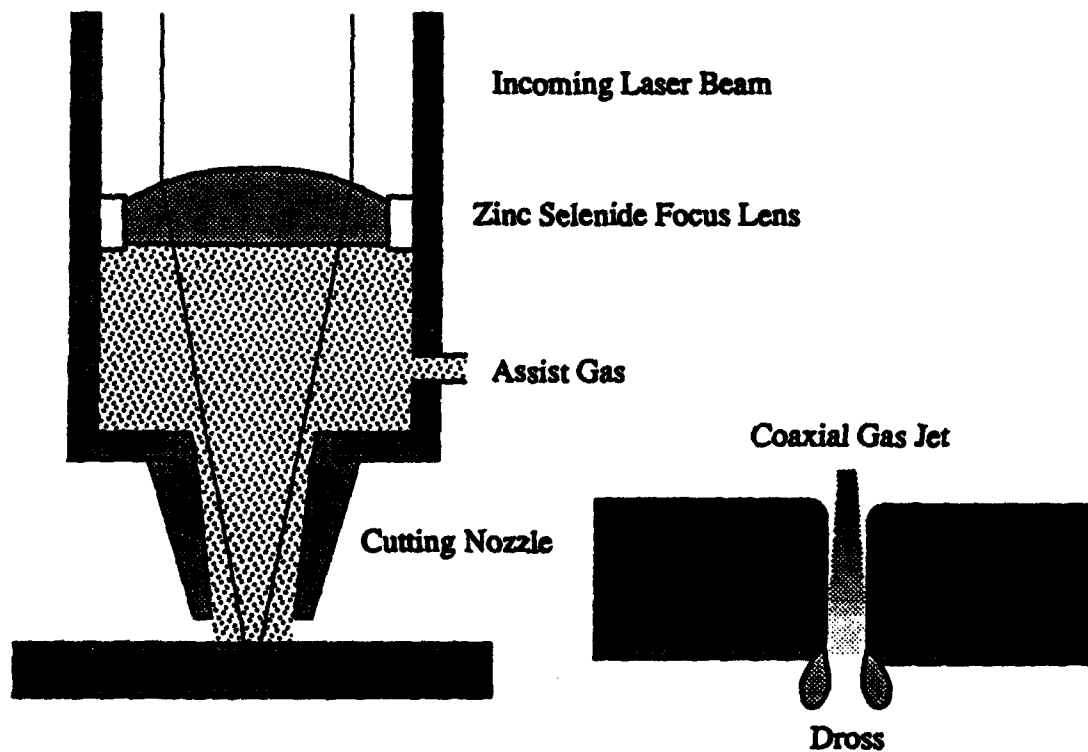
Figure 8. Experimental configuration for the laser cutting and laser beam welding experiments used in this investigation.
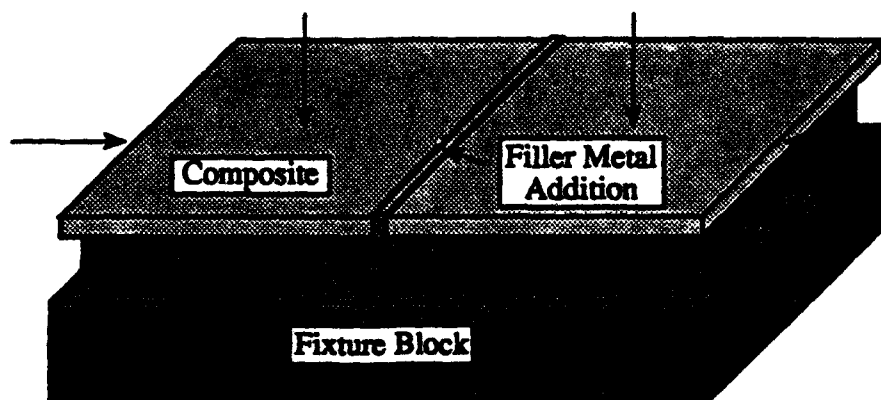
Figure 9. Welding fixture used for the addition of filler metals.

Chapter 4

RESULTS AND DISCUSSION

4.1. Laser Cutting

Laser cutting experimentation involved developing parameters for the composites and characterization the laser cuts made using the developed parameters. Characterization of the laser cuts included examination of the microstructure and microhardness testing to determine the effects on the composites due to laser cutting. The maximum laser cutting for the composites were determined for a specified set of parameters (1500 W, 63.5 mm focal length lens, 47 ℓ/min air). A comparison of these maximum cutting rates (based on the specified parameters) was made to a calculated emissivities for the composites.

4.1.1. Dross Formation

The most observable effect of laser cutting was the dross attached to the DRA composites reinforced with silicon carbide whiskers, 6061/SiC/20w and A356/SiC/20w. Although some dross generally remains attached to the exit of laser cut materials, a significant amount of dross remained attached to the whisker reinforced materials, as shown in Figure 10. The average height of the dross attached to the bottom of a 2mm sample of 6061/SiC/20w composite processed with a variety of process parameters was 1.25 mm. Different assist gases (air, O_2, N_2), gas flow rates, power levels, and travel speeds were used in an attempt to minimize the dross adhered to the bottom of the cuts; however, the changes did little to modify the attached dross. The dross attached to the cut exits of the 6061/SiC/20w and A356/SiC/20w composites was very difficult to remove, unlike that of the 6061Al$_2$O$_3$/20p and X2080/SiC/15p composites.
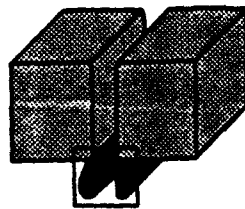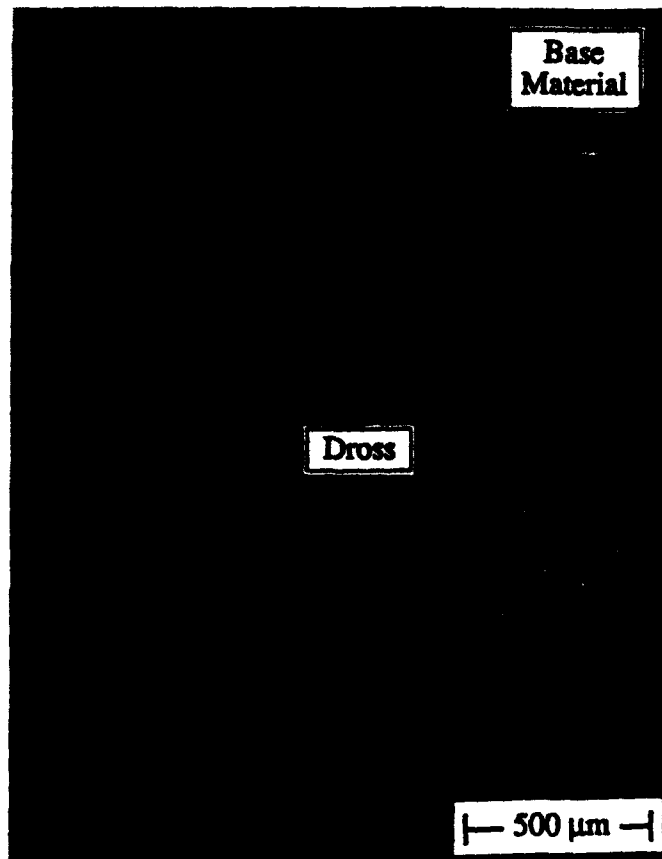
Figure 10. Dross attached to the cut exit of a laser cut made
on the 6061/SiC/20w composite.

Microstructural analysis of the dross formed on the silicon carbide whisker reinforced composites revealed platelets within the matrix that have been identified as aluminum carbide by previous researchers [24-30], as shown Figure 11. It is believed that the molten aluminum reacts with the silicon carbide whiskers, forming a viscous mixture of aluminum, aluminum carbide, and silicon. The assist gas moves the mixture toward the bottom of the cut, but is unable to expel it completely, due to its high viscosity, resulting in the buildup of the dross at the cut exit. Quantitative microscopy of a laser cut made on the 6061/SiC/20w composite determined that 78 percent of the volume of material removed from the cut remained attached to the exit of the cut as dross.

The amount of dross attached to the bottom of the cut was found to be a function of the thickness of the composite. Figure 12 shows the amount of dross attached to the bottom of the laser cuts made on the $6061/Al_2O_3/20p$ composite as a function of thickness, for thicknesses from 2 to 4 mm. As can be seen in the SEM micrographs, the amount of dross attached to the cut exit of the $6061/Al_2O_3/20p$ composite increases with thickness. An increase in the amount of attached dross with increasing thickness was also observed in the 6061/SiC/20w composite, although the amount of attached dross was much greater.

The laser cutting rate also affected the amount of dross attached to the cut exit of the $6061/Al_2O_3/20p$ composite. Shown in Figure 13 are SEM micrographs of the cut exits of a 3 mm thick section of the $6061/Al_2O_3/20p$ composite cut at several different travel speeds. The micrographs indicate that faster cutting rates result in less dross attached to the cut exit.
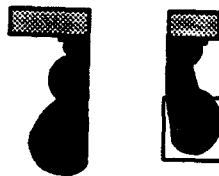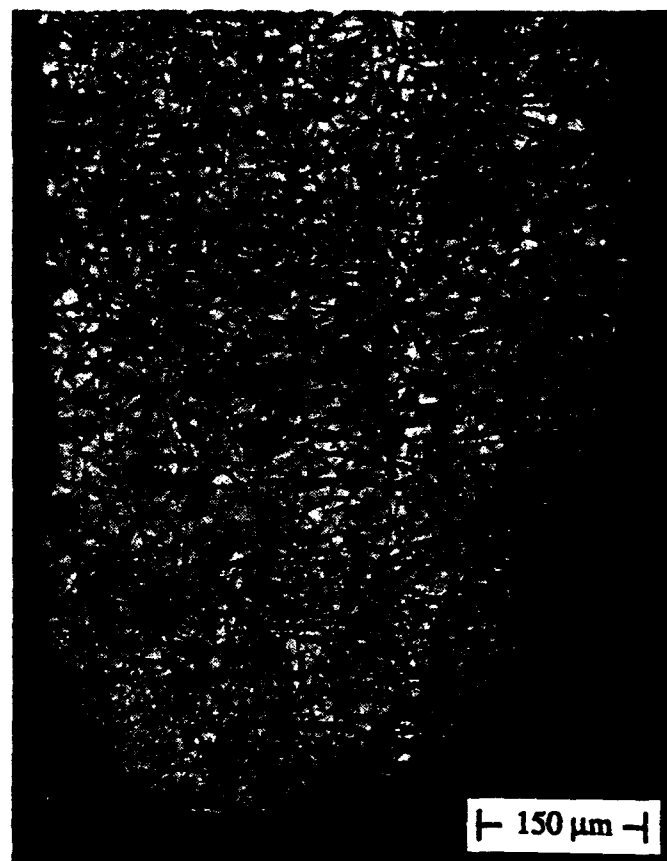
Figure 11. Microstructure of the dross attached to the bottom of a laser cut made on the 6061/SiC/20w composite showing aluminum carbide platelets in an aluminum matrix.
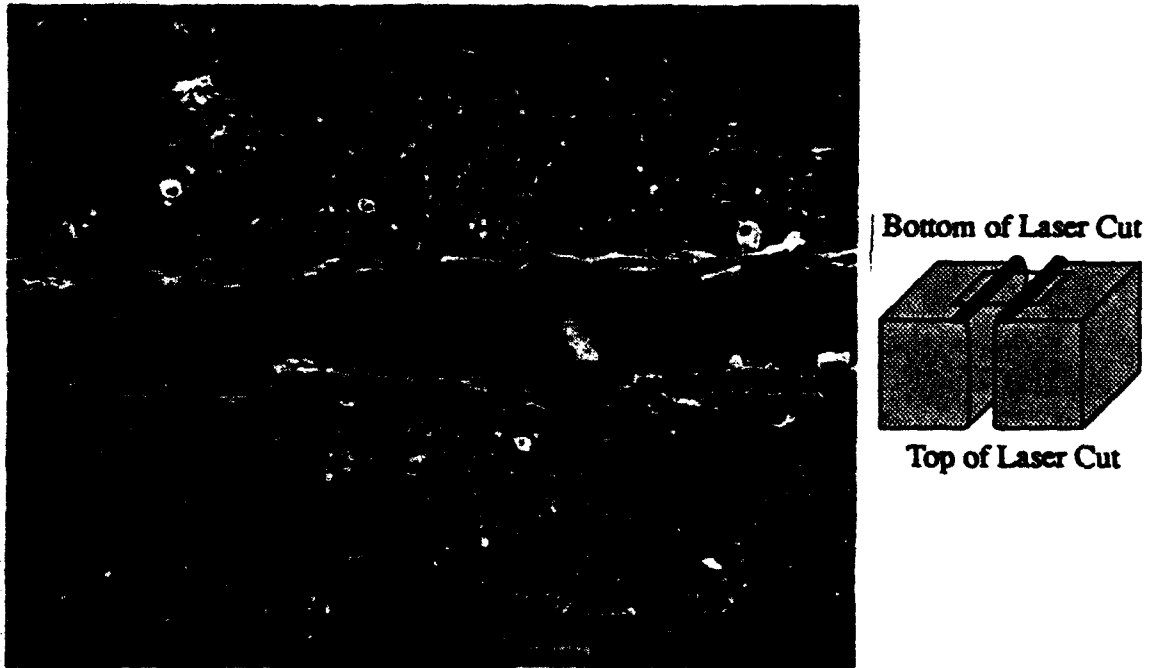
Figure 12.1. SEM micrograph of the cut exit of a 2 mm thick section of the 6061/Al$_2$O$_3$/20p composite cut at 15 cm/s.
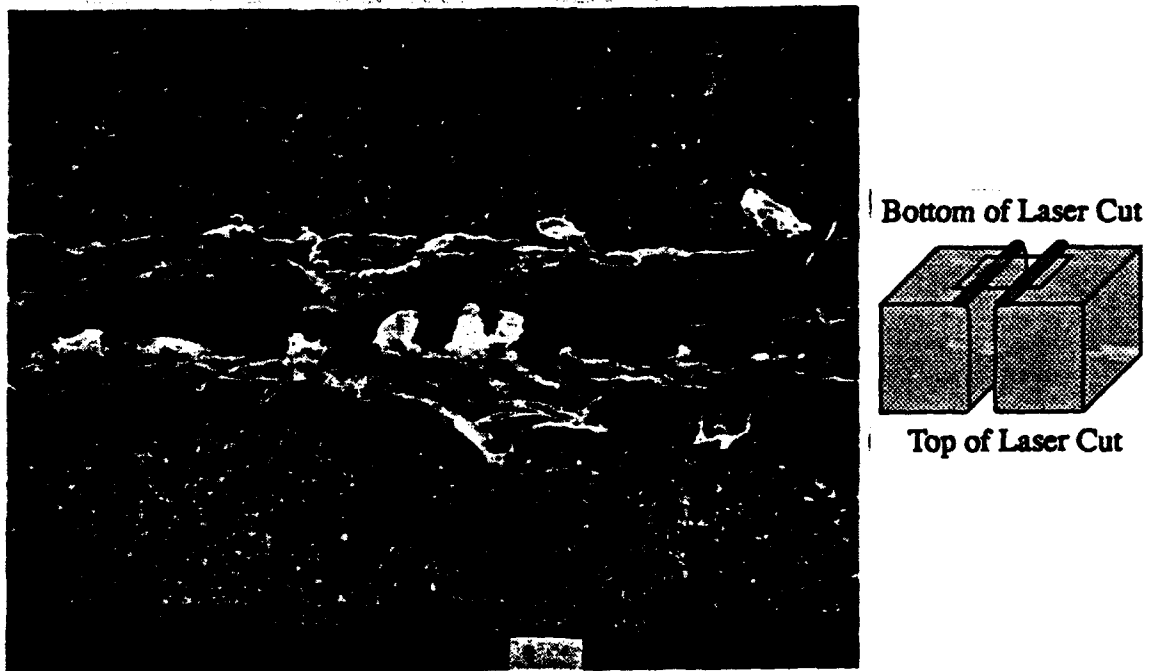
Figure 12.2. SEM micrograph of the cut exit of a 3 mm thick section of the 6061/Al$_2$O$_3$/20p composite cut at 6 cm/s.

Bottom of Laser Cut

Top of Laser Cut
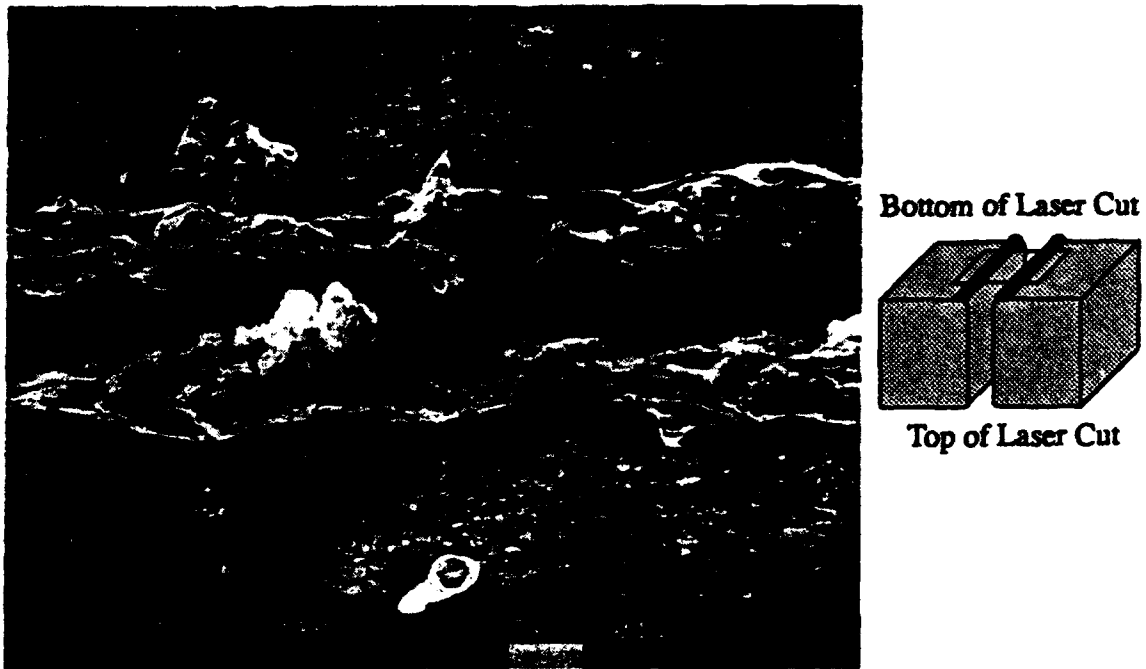
Figure 12.3. SEM micrograph of the cut exit of a 4 mm thick section of the 6061/Al$_2$O$_3$/20p composite cut at 4 cm/s.
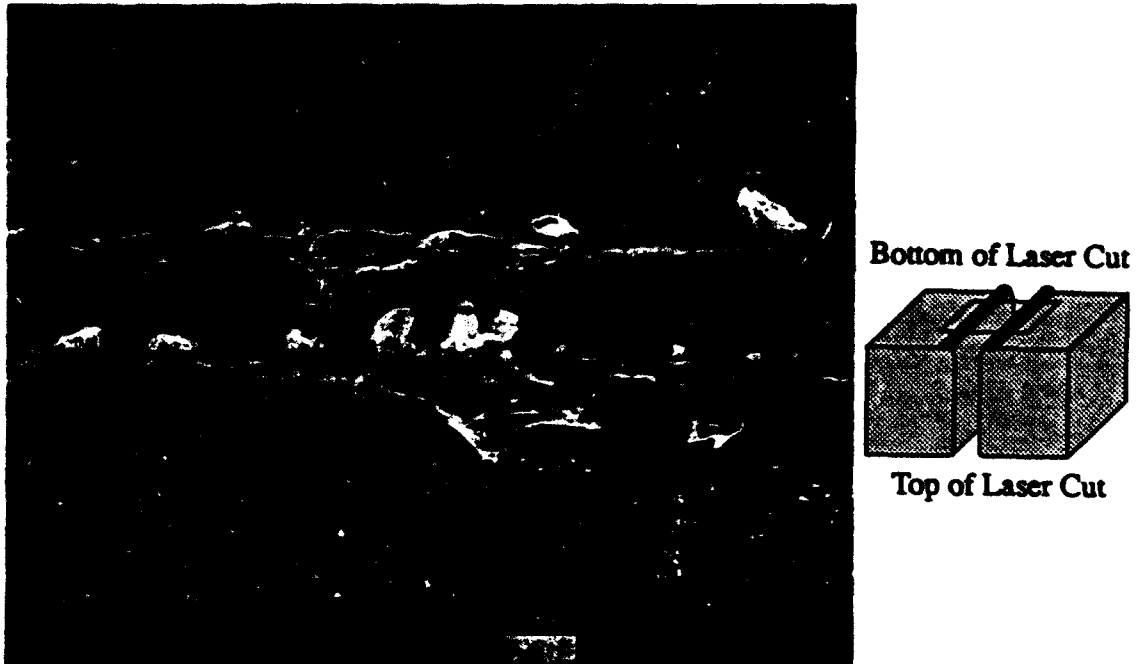
Figure 13.1. SEM micrograph of the cut exit of a 3mm thick section of the 6061/Al$_2$O$_3$/20p composite cut at 6 cm/s.
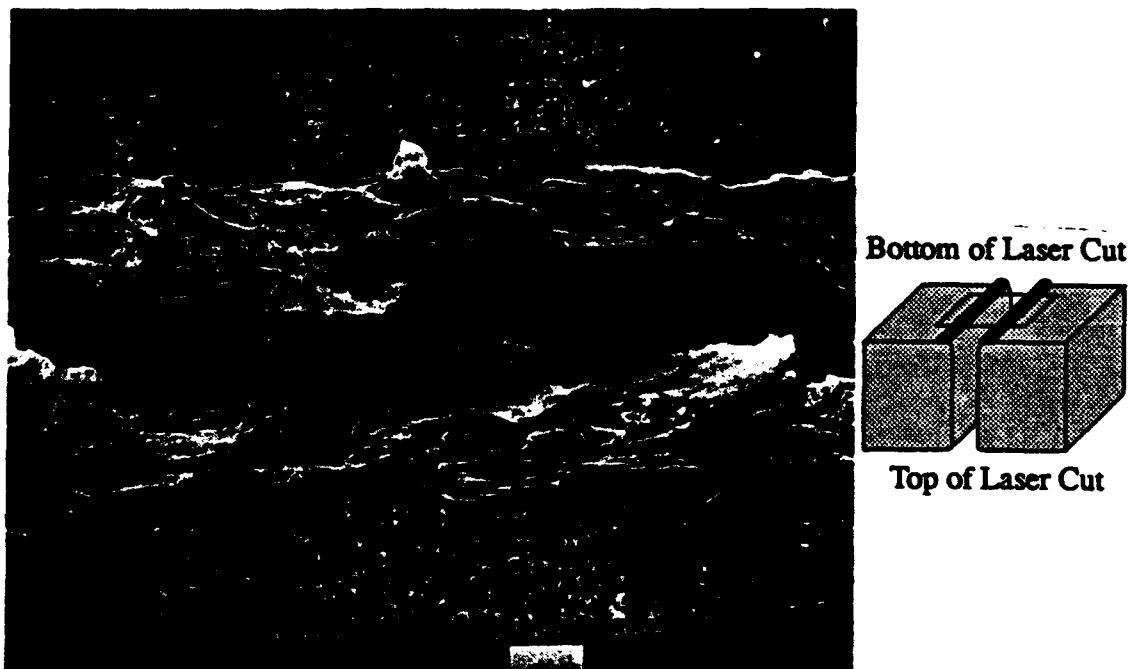
Figure 13.2. SEM micrograph of the cut exit of a 3mm thick section of the 6061/Al$_2$O$_3$/20p composite cut at 4 cm/s.
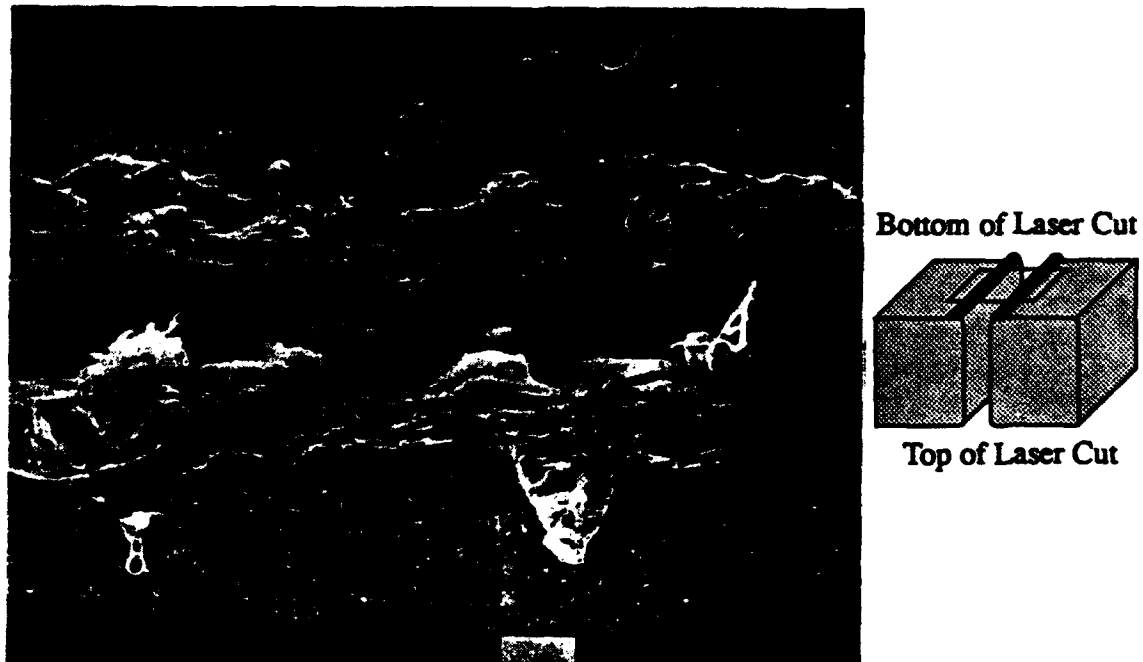
Figure 13.3. SEM micrograph of the cut exit of a 3 mm thick section of the
6061/Al$_2$O$_3$/20p composite cut at 2 cm/s.

4.1.2. Microstructure

An analysis of the microstructure of the laser cut composites show the effects of laser processing on the various materials. Shown in Figure 14 are photomicrographs of the cross sections of laser cuts made on the 6061/Al$_2$O$_3$/20p-F (14.1), X2080/SiC/15p-T6 (14.2), 6061/SiC/20w (14.3), and A356/SiC/20w-F (14.4) composites, which were cut using air as an assist gas. Laser cutting appears to have the most noticeable effects on the silicon carbide whisker reinforced composites, (14.3) and (14.4), as evidenced by a reaction layer on the cut surface. It is believed that a thin layer consisting of a mixture of aluminum, aluminum carbide and silicon remains attached to the surface of the cut as the assist gas expels the molten material, as can be seen in Figure 15. Porosity, attributed to P/M fabrication, is also evident in the heat affected zone of the 6061/SiC/20w composite laser cut shown in Figure 15. The large amount of porosity evident in the heat affected zone of the A356/SiC/20w-F composite (14.4), is believed due to hydrogen present in the as fabricated material. It is believed that the rapid solidification of the HiPIC fabrication process may trap hydrogen in the composite. As previously mentioned, aluminum has a high solubility for hydrogen. Any hydrogen present in the aluminum would not have sufficient time to diffuse out of the composite and the high pressure used during HiPIC (100 MPa) may have prevented nucleation of pores. The entrapped hydrogen appears to have been released from the composite during heating, since porosity of this magnitude was not observed in the as cast material. This behavior is similar to the that observed in laser processed DRA composites produced by P/M techniques. In addition, the porosity observed in the laser cut A356/SiC/20w composite follows the layers of the silicon carbide whisker preform that was infiltrated to form the composite. The particulate reinforced materials, (14.1) and (14.2), responded very well to the laser cutting operation, with no reaction layer visible during microstructural analysis.

Cut Surface

├─100 µm─┤
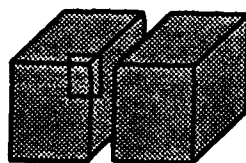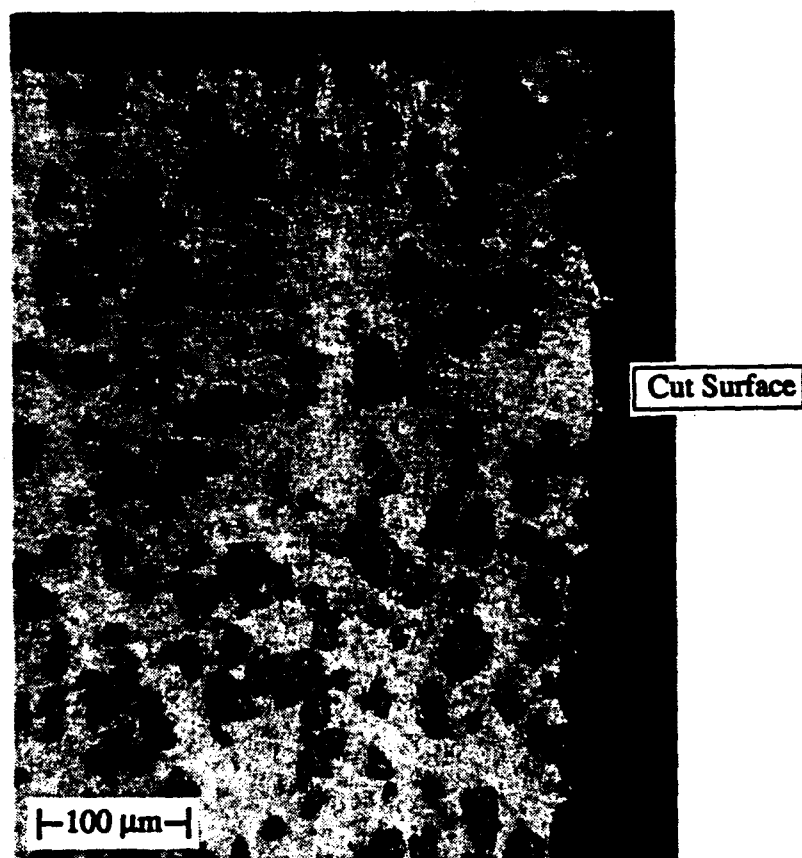
Figure 14.1. Photomicrograph of the cross section of a laser cut made on the
6061/Al$_2$O$_3$/20p composite.

Cut Surface

├─100 μm─┤
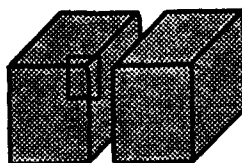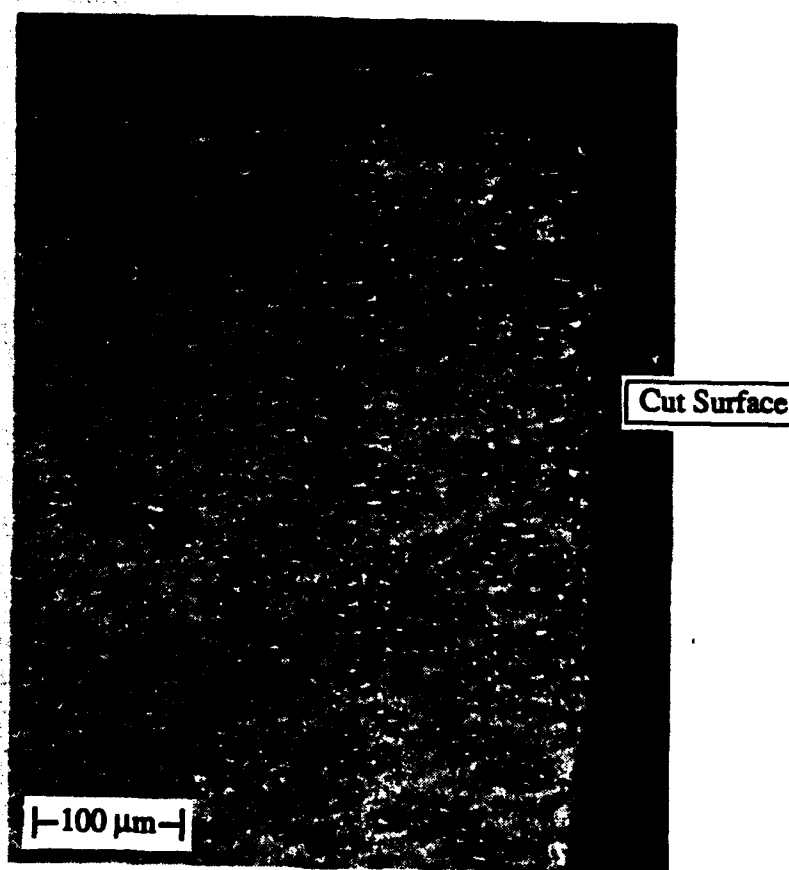
Figure 14.2. Photomicrograph of the cross section of a laser cut made on the
X2080/SiC/15p composite.

Cut Surface

⊢100 μm⊣
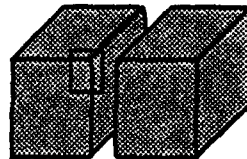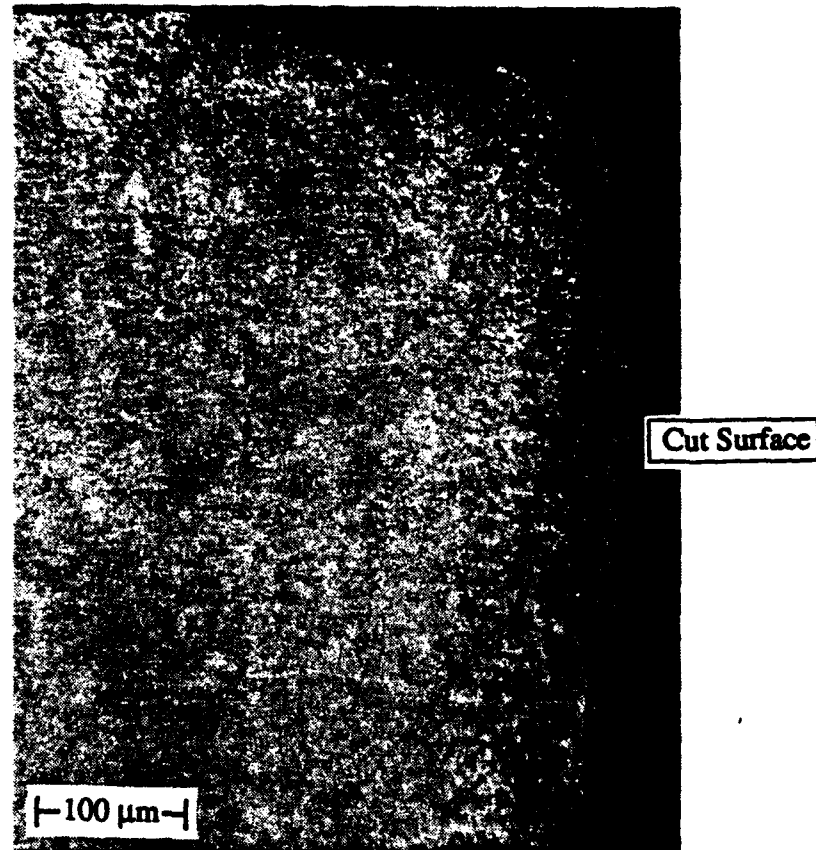
Figure 14.3. Photomicrograph of the cross section of a laser cut made on the
6061/SiC/20w composite.
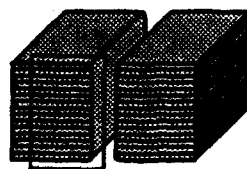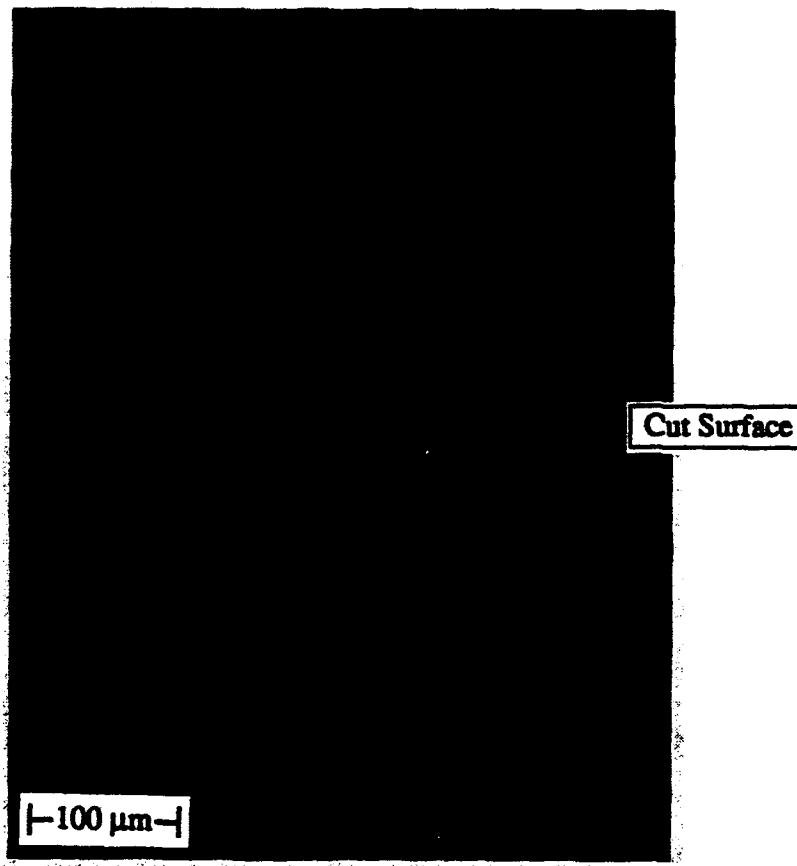
Figure 14.4. Photomicrograph of the cross section of a laser cut made on the A356/SiC/20w composite.
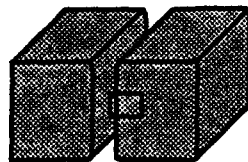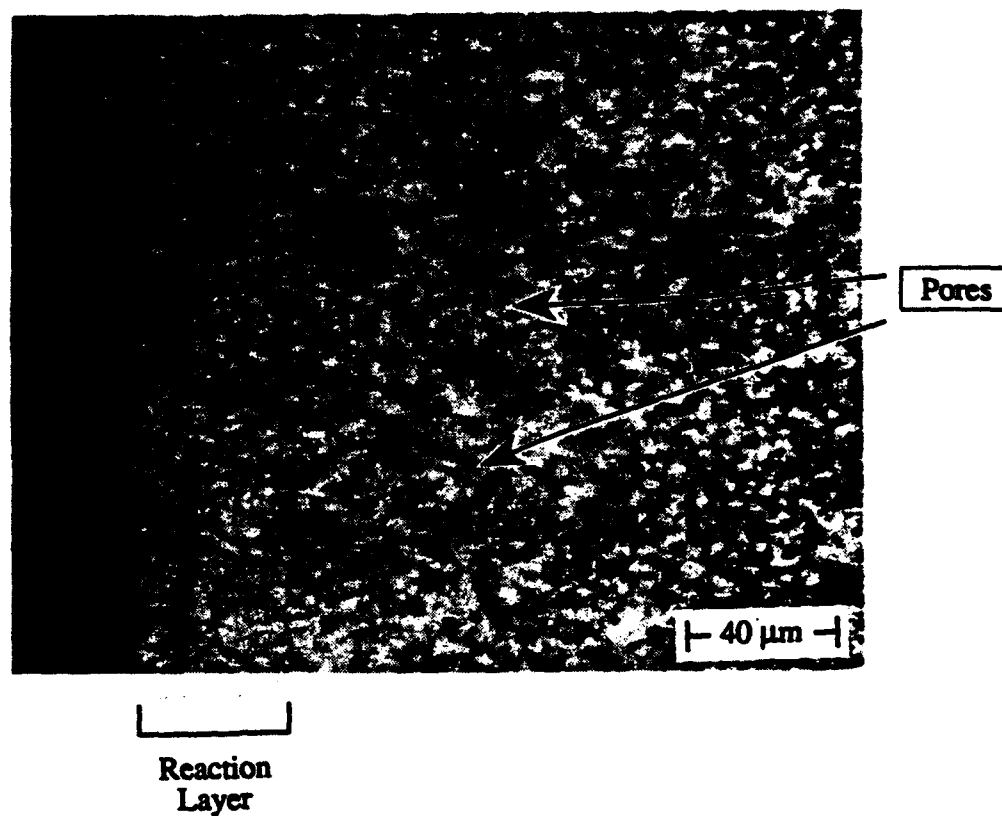
Figure 15. Reaction layer on the surface of the laser cut of the 6061/SiC/20w composite.

It is evident from a comparison of the microstructures of the silicon carbide reinforced materials, (14.2), (14.3) and (14.4), that the reinforcement morphology may affect the formation of aluminum carbide on the cut surface; since no aluminum carbide was evident at the cut surface of the composite reinforced with silicon carbide particulates. The lack of aluminum carbide on the cut surface of the X2080/SiC/15p-T6 is believed due to the morphology of the reinforcement. The particulates ($\approx$ 16 μm) [6] are much larger than the whiskers ($\approx$ 1 μm in diameter, 10-100 μm in length) [54]. The particulates have a smaller surface area per unit volume than the whiskers, and therefore less silicon carbide is in contact with the molten aluminum. It is believed that the molten aluminum and silicon carbide particulates are expelled by the assist gas before the formation of aluminum carbide can affect the viscosity of the molten material. It should be noted that the presence of 0.2 weight percentage of zirconium in the X2080 alloy [55] may have inhibited the formation of aluminum carbide to some extent, due to thermodynamic considerations. Reynolds and Yang [43] have shown that low levels of zirconium (3 wt%) can prevent the formation of aluminum carbide during low pressure plasma joining of 1100-30wt% SiCp composites.

4.1.3. Cutting Rate

The cutting rates for the composites were found to be higher than that of unreinforced aluminum, except for the SiCw reinforced composites. The 6061/Al_2O_3/20p composite had the best response to laser cutting, with very fast cutting rates attained. The range of maximum cutting speed as a function of thickness for the 6061/Al_2O_3/20p composite is shown in Figure 16, along with the maximum cutting rate for aluminum alloy 6061, based on the following parameters (1500 W, 63.5 mm focal length lens, 47 ℓ/min air). The difficulties involved in cutting samples and limited material prevented determination of the maximum cutting rate to a high degree of accuracy, and only a range

could be generated. The upper bound in the figure is lowest speed were the composite was not cut for the given thickness; the lower bound in the figure is the highest speed were the composite was cut. The maximum cutting speed is somewhere between the upper and lower bound. The maximum cutting rate data for 6061 Al is accurate to + 0.25 cm/s. Air was used as the assist gas during cutting of the 6061/Al_2O_3/20p composite due to its availability; however, the use of oxygen showed an increase of about six percent in the cutting rate at a thickness of 2 mm.

The improvements in the cutting rate of the 6061/Al_2O_3/20p and X2080/SiC/15p composites over unreinforced aluminum are believed due to the improved absorptivity of the composite. The reinforcement materials commonly used in DRA composites, silicon carbide and aluminum oxide , absorb much more energy at 10.6 μm wavelength than does aluminum, as shown by the increased emissivity (Figure 17) [50, 56]. Using this emissivity data for the bulk materials, effective emissivities for the composites were calculated using the rule of mixtures. These calculated emissivities, shown in Table 3, are approximations for comparison to experimental results. The calculations are based solely on emissivity values of bulk materials and the rule of mixtures. The absorptivity of the reinforcement in the composite may be different that of the bulk material and would therefore affect the effective emissivity calculated for the material. In addition, the emissivity for pure aluminum was used for the calculations, and it has been shown that alloying additions can affect the amount of energy absorbed by aluminum alloys [52].

Table 3. Calculated Emissivity Values at 10.6 μm for Several Composite Materials.

Material	Percent Emissivity
Al/Al_2O_3/20	14.92
Al/SiC/20	5.11
Al/SiC/15	4.31
Aluminum [50]	1.90
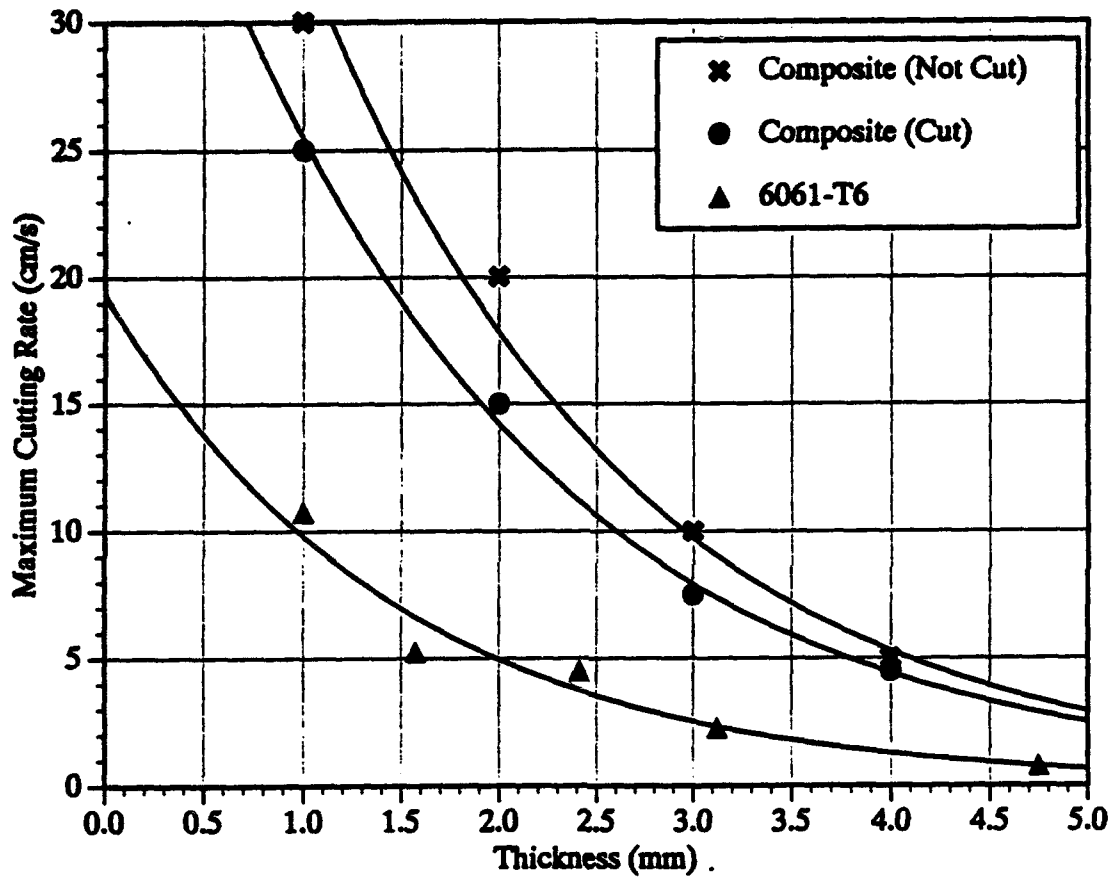
Figure 16. Range of the maximum cutting rate of the $6061/Al_2O_3/20p$ composite and aluminum alloy 6061 as a function of thickness. (Maximum laser cutting rate based on 1500 W, 63.5 mm focal length lens, and 47 ℓ/min air)
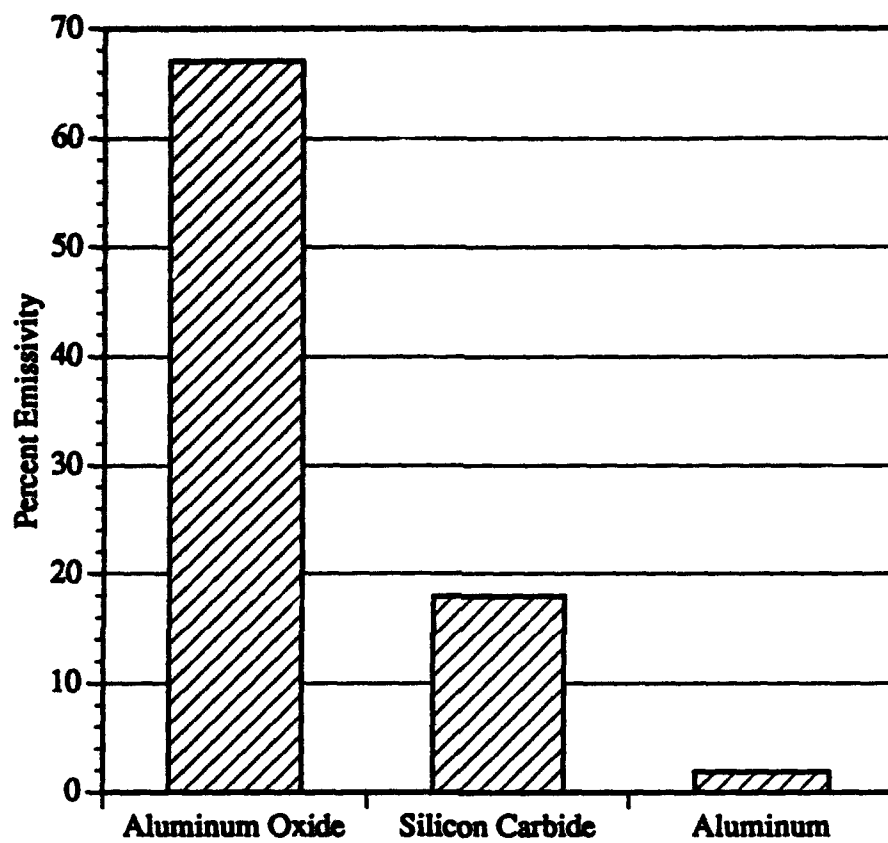
Figure 17. Bulk emissivity of the composite constituents at a wavelength of 10.6 µm.

Comparison of the effective emissivities to the maximum cutting rate of several composites at 1.6 mm thickness (Figure 18) shows that there is some correlation between the two. Although emissivity cannot be used to directly predict the cutting rate of a material, a correlation between the emissivity of the material and the laser cutting rate does exist. The low cutting rate of the 6061/SiC/20w composite in comparison to 6061 Al is believed to be due to the formation of aluminum carbide. Slower cutting rates appear to be necessary to overcome the effects of the increased viscosity of the molten composite material caused by the formation of aluminum carbide. The increased viscosity appears to have overcome the effect of improved emissivity in the 6061/SiC/20w composite.

4.1.4. Microhardness

Microhardness testing was performed on the cross sections of a 2 mm thick laser cut 6061/Al$_2$O$_3$/20p composite to determine the effects on the material due to laser cutting. Testing of laser cuts made at various cutting speeds, which correspond to different heat inputs (slower travel speeds = greater heat input), are shown in Figure 19. The data shows that the loss of hardness extends approximately 0.4 mm from the cut surface. In addition, the loss of hardness observed in the composite is independent of the cutting speed. Microstructural observations indicated the existence of a coarse precipitate near the cut surface and a fine precipitate away from the cut surface. The analysis suggests that coarsening of the Mg$_2$Si precipitates is responsible for the decrease in hardness [57]. A micrograph of the composite matrix at the cut edge shows the Mg$_2$Si precipitates as a black phase in Figure 20. In contrast, at a distance of 0.4 mm from the cut surface, where the hardness returns to that of the base material, the Mg$_2$Si precipitates are too small to be resolved, Figure 21. This suggests growth of the Mg$_2$Si precipitates in the matrix from the unresolvable size in the base material shown in Figure 21, to the size shown in Figure 20 at the edge of the cut surface.
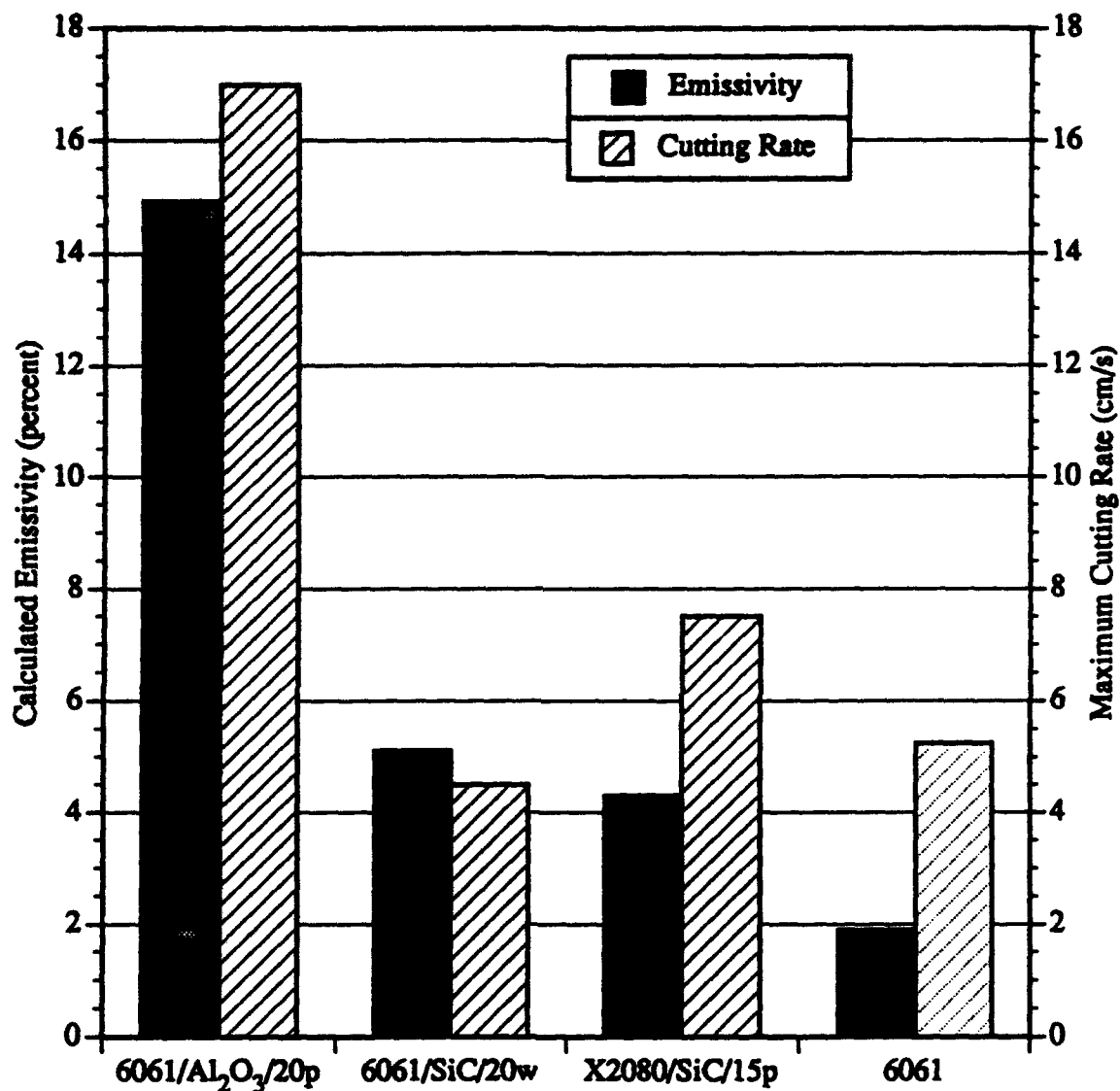
Figure 18. Comparison of the effective emissivity to the maximum laser cutting
rate of the composites at a thickness of 1.6 mm. (Maximum laser cutting rates
based on 1500 W, 63.5 mm focal length lens, and 47 ℓ/min air)
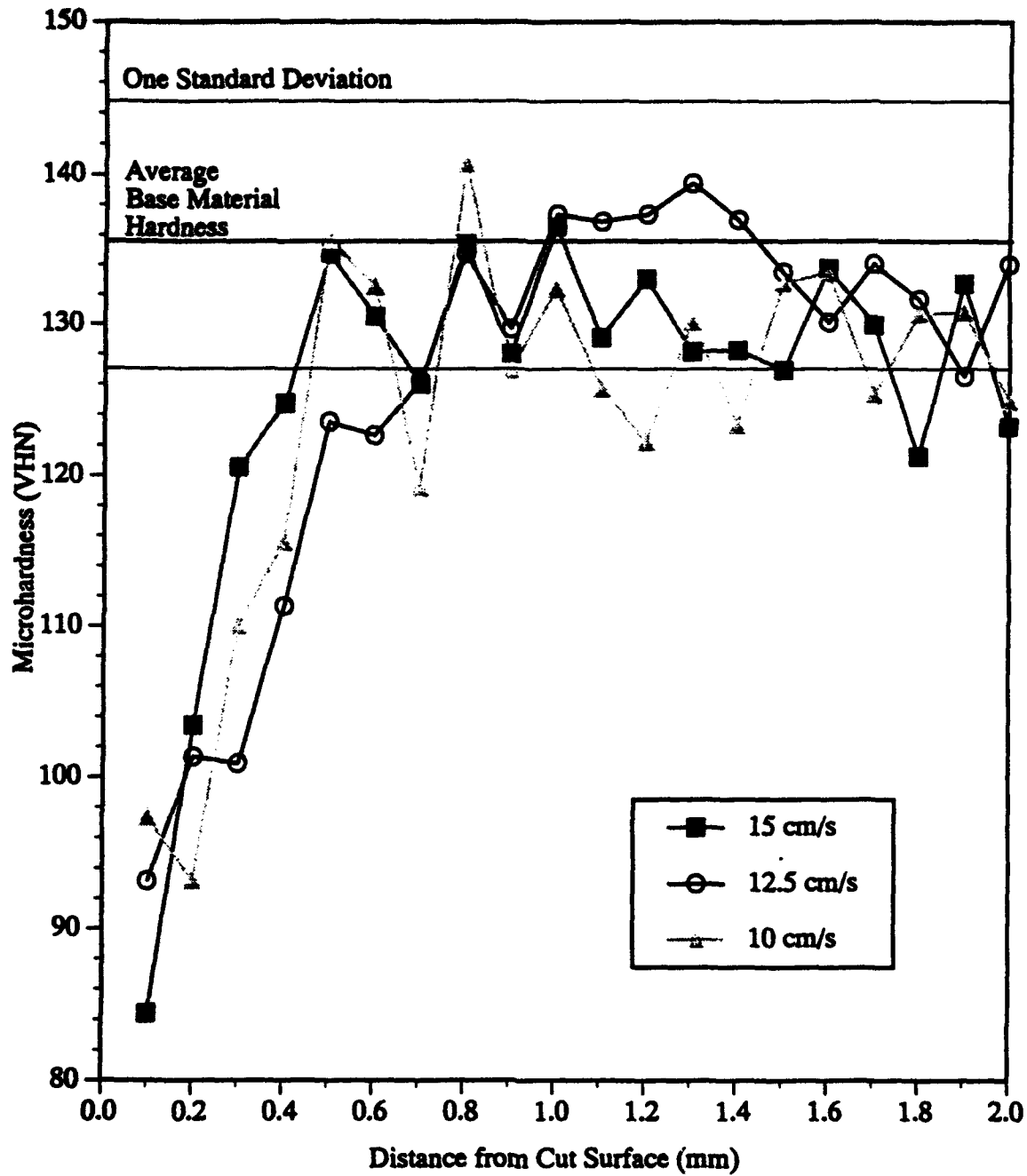
Figure 19. Plot of the average microhardness of the cut cross section of laser cuts made on 2 mm thick sections of the 6061/Al$_2$O$_3$/20p composite cut at several speeds.
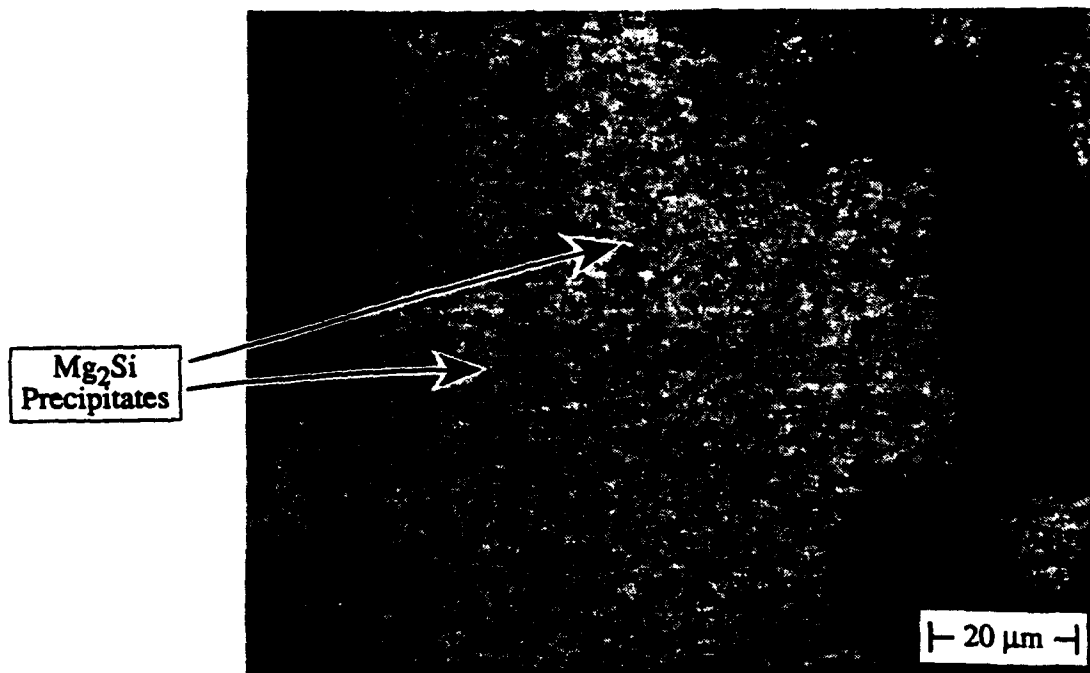
Figure 20. Microstructure at the cut surface of a laser cut made on the 6061/Al$_2$O$_3$/20p composite cut at 15 cm/s, showing Mg2Si precipitates in the matrix.
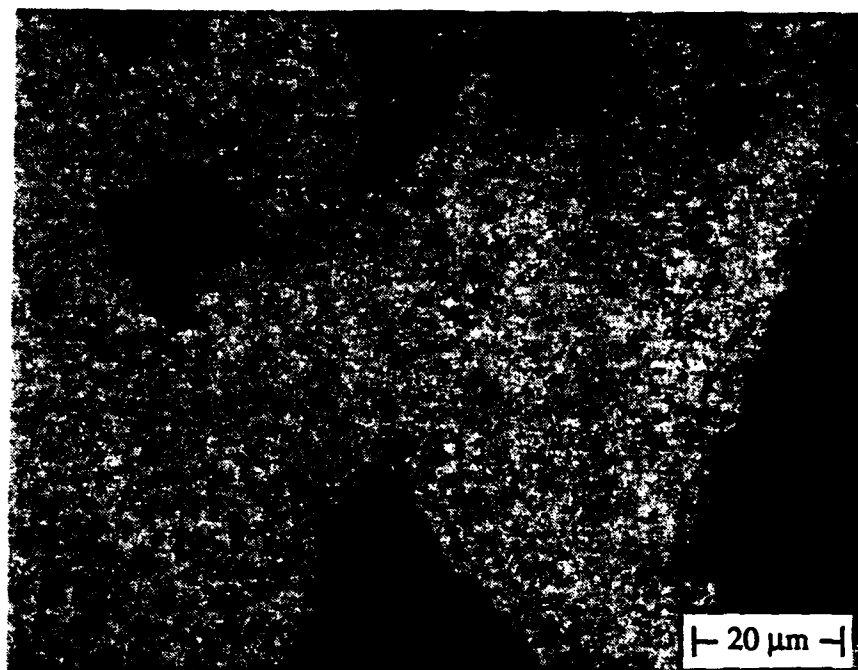
Figure 21. Microstructure at a distance of 0.4 mm from the cut surface of a laser cut made on the 6061/Al$_2$O$_3$/20p composite cut at 15 cm/s. The Mg2Si precipitates are too small to be resolved.

Microhardness testing was also performed on a 1 mm thick 6061/SiC/20w composite laser cut. In this case, the heat affected zone due to cutting is very small, less than 0.1 mm, as shown in Figure 22. A significant increase in the hardness found to be due to the reaction layer on the cut surface. The reaction layer had a hardness of 283 VHN. The smaller heat affected zone of the 6061/SiC/20w composite in comparison to the larger heat affected zone of the $6061/Al_2O_3/20p$ composite may be a function of the thermal properties of the materials. The thermal properties of the composites in comparison to the matrix material show that increasing the silicon carbide level increases thermal conductivity, while increasing the aluminum oxide content decreases the thermal conductivity [58]. As a result, the heat imparted by the laser would be conducted away more quickly in the 6061/SiC/20w composite resulting in a small heat affected zone. In contrast, the low thermal conductivity of the $6061/Al_2O_3/20p$ composite would result in a larger heat affected zone since heat is transported more slowly.

4.2. Laser Beam Welding

Laser beam welds were made on the DRA composites to determine the depth of penetration into the material for comparison to the effective emissivity. Autogenous laser beam and gas tungsten arc (GTA) welds were made on the 6061/SiC/20w and the A356/SiC/20p composites to determine the effects on the materials and to characterize the microstructure. The focus of the laser beam welding experimentation dealt with eliminating the formation of aluminum carbide by filler metal additions. Appropriate filler metals and the respective carbides were analyzed for thermodynamic stability and for physical and chemical compatibility in the weld. A computer program used to determine the chemical equilibrium of a system was employed to predict the amount of filler metal necessary to prevent the formation of aluminum carbide in a Al/SiC/20 composite. Shims of filler metal were placed between two thin plates of 6061/SiC/20w and were laser beam welded. The welds were characterized using electron probe microanalysis and optical microscopy.
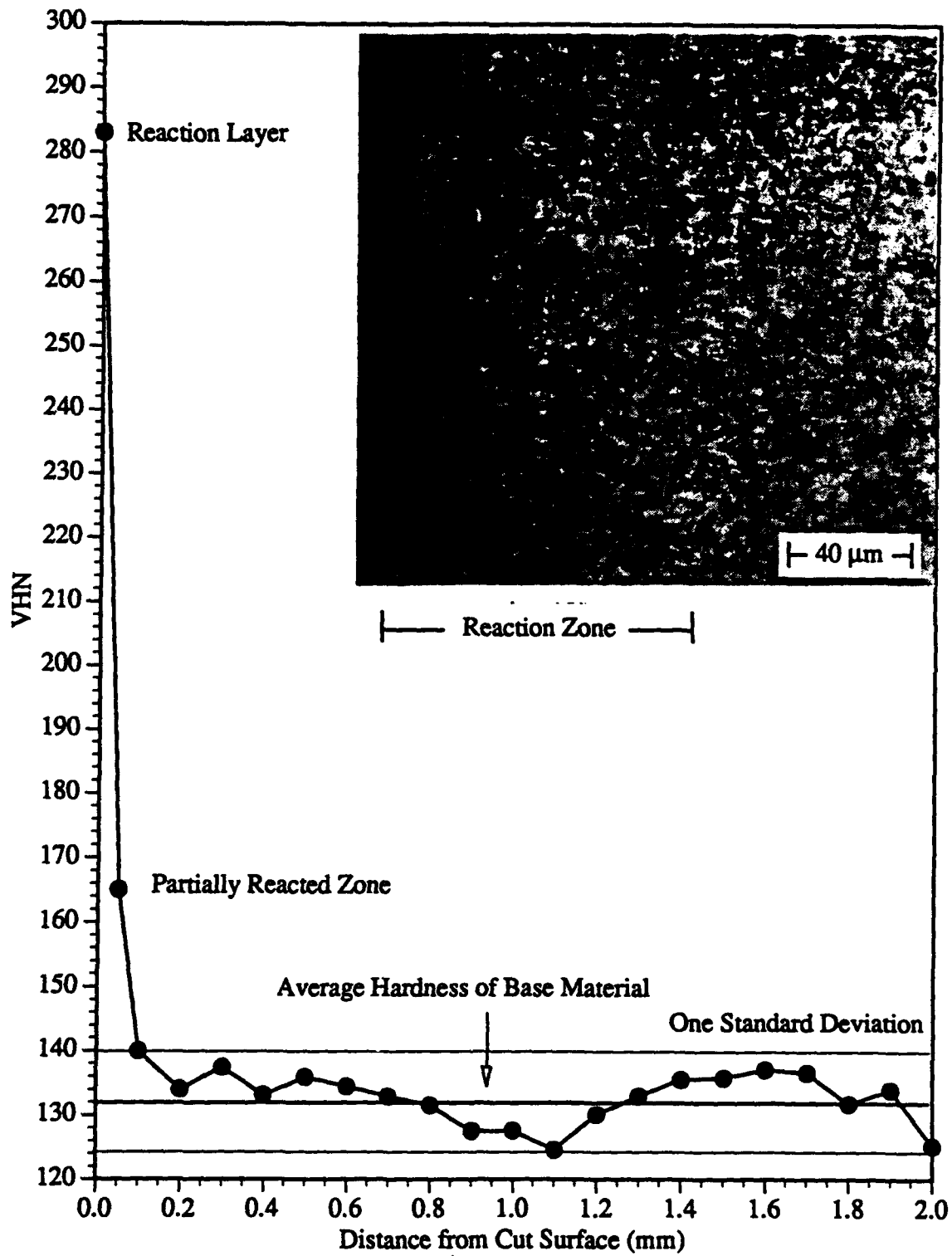
Figure 22. Plot of the microhardness of a cross section of a laser cut on a 1 mm thick section of the 6061/SiC/20w composite. (1500 W, 7 cm/s, 100 CFH air)

4.2.1. Autogenous Laser Welds

Autogenous laser beam welds were made on the $6061/Al_2O_3/20p$ and $6061/SiC/20w$ composites and aluminum alloy 6061 to compare the depth of penetration of the weld to the effective emissivity of the materials. The comparison (Figure 23) shows that the effective emissivities agree reasonably well with the weld penetration depths. For aluminum alloy 6061, the energy density was not sufficient to initiate a keyhole, due to the high reflectivity of the aluminum. The resultant conduction mode is shallow in comparison to keyhole mode welds on the composite materials.

4.2.2. Microstructure

Autogenous laser beam and gas tungsten arc (GTA) welds were made on the $6061/SiC/20w$ and the $A356/SiC/20p$ composites to determine the effects on the materials and to characterize the microstructure. Gas tungsten arc (GTA) welding was used for comparison to laser beam welding (LBW) since it is a well established and commonly used fusion joining technique. GTA welds are generally wide and shallow, with large heat affected zones, and the weld pool temperatures are relatively low. In contrast, laser beam welds are usually very narrow and deep, have a small heat affect zone, and relatively high weld pool temperatures.

The microstructure of welds made on $6061/SiC/20w$ and $A356/SiC/20p$ composites show the differences between laser beam and gas tungsten arc welding. Figure 24 exhibits the microstructural features common to laser beam welds made on silicon carbide reinforced composites; aluminum carbide platelets and a large weld crown. The large pores observed in the fusion zone are believed to be related to hydrogen present in the composite. The low fluidity of the molten material combined with the fast cooling rates may prevent the gases from escaping from the fusion zone.
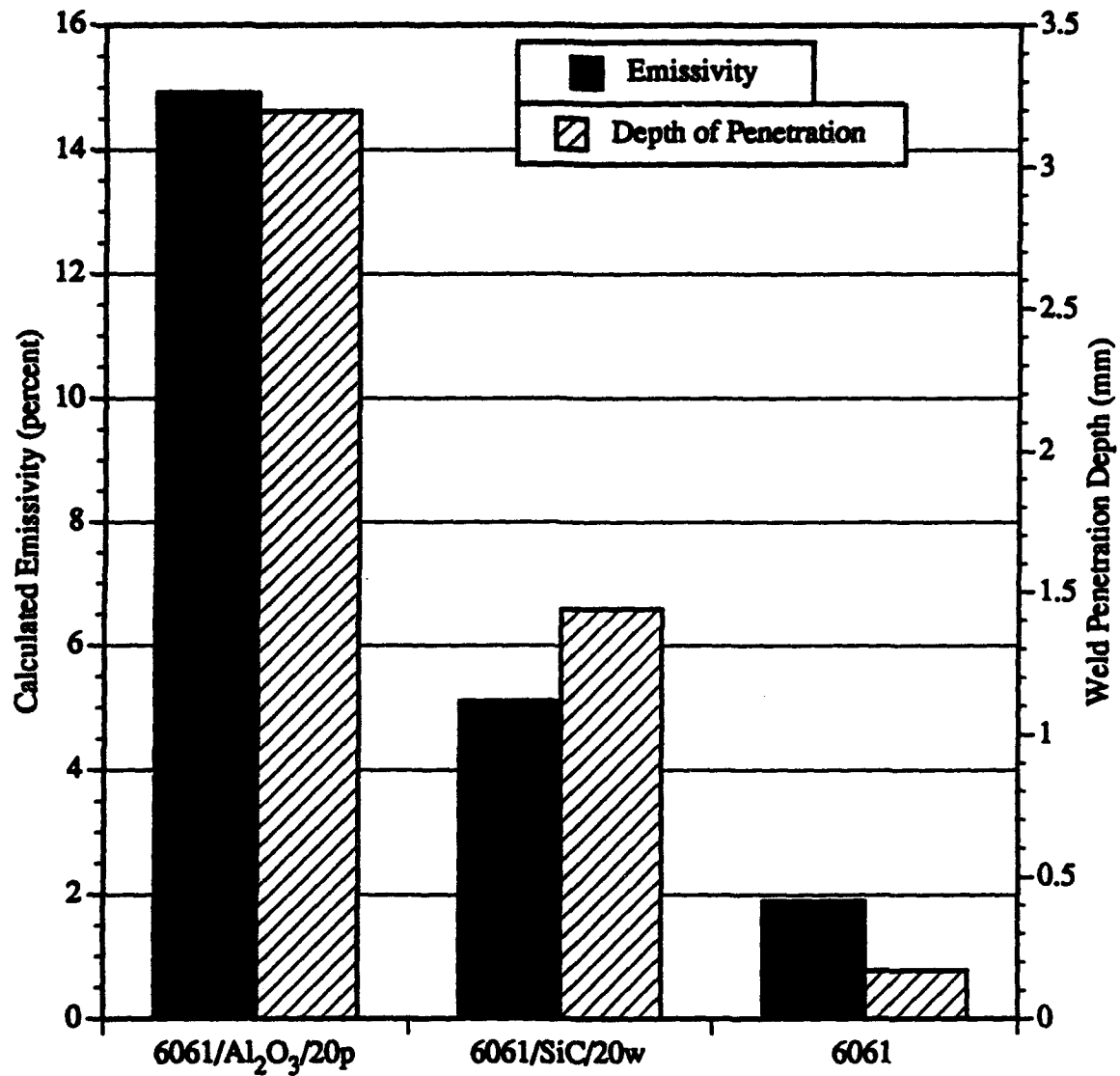
Figure 23. Comparison of the effective emissivity to the weld penetration depth of two composites and aluminum alloy 6061.
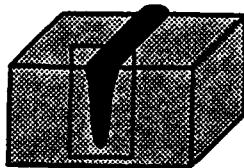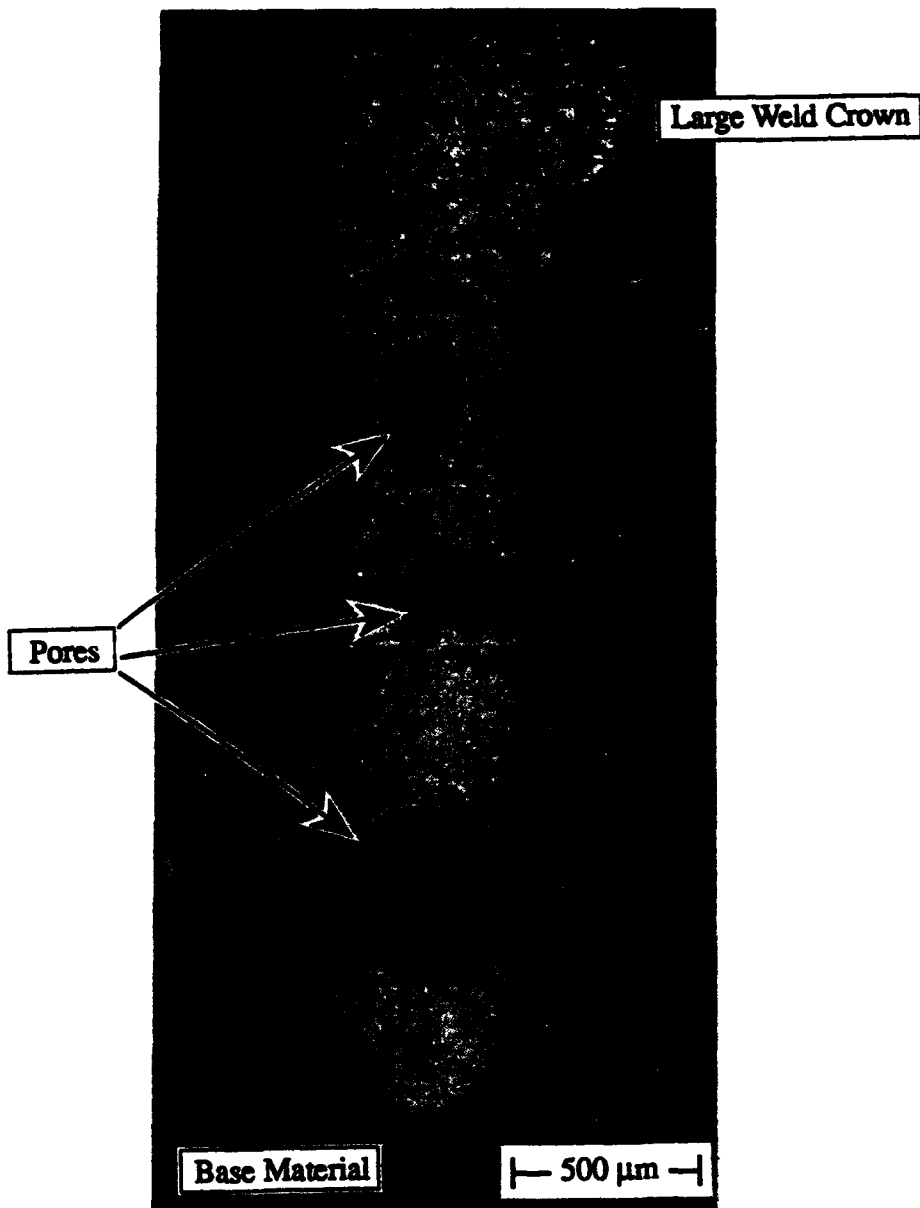
Figure 24. Laser beam weld made on the 6061/SiC/20w composite showing aluminum carbide platelets, pores in the fusion zone, and a large weld crown. (1500 W, helium shielding gas)

Although arc welding provides a lower weld pool temperature than a laser weld, the formation of aluminum carbide platelets is evident in the arc weld of this material, Figure 25. A comparison of weld morphology reveals that the GTA weld is much wider and shallower than the laser beam weld, as expected. The microstructure of the GTA weld is similar to that of the laser beam weld, containing aluminum carbide platelets and having a large weld crown. The aluminum carbide platelets in the arc weld are larger than those in the laser beam weld. The increase in platelet size is probably due to the slower cooling rate of the GTA weld, allowing more growth prior to solidification. A macrograph of the GTA weld reveals a significant amount of porosity in the heat affected zone of the weld which is attributed to P/M fabrication, Figure 26.

Initial observations for a laser beam weld on the A356/SiC/20p composite shows a narrow weld which penetrates deep in the material, Figure 27. A comparison of the unetched microstructure (Figure 28) to the etched microstructure (Figure 29) revealed that the weld was much larger than previously believed. Analysis of the etched microstructure reveals four distinct regions of the weld. Region 1, (Figure 30), shows a large solidified structure that is characteristic of slow cooling. Region 2, reveals a fine solidified structure that is characteristic of relatively fast cooling, Figure 31. The microstructure of Region 3 contains both silicon carbide particles and aluminum carbide platelets, as shown in Figure 32. The microstructure of region 4, exhibits aluminum carbide plates, silicon particles, and aluminum, Figure 33. No silicon carbide particles remain in this region.
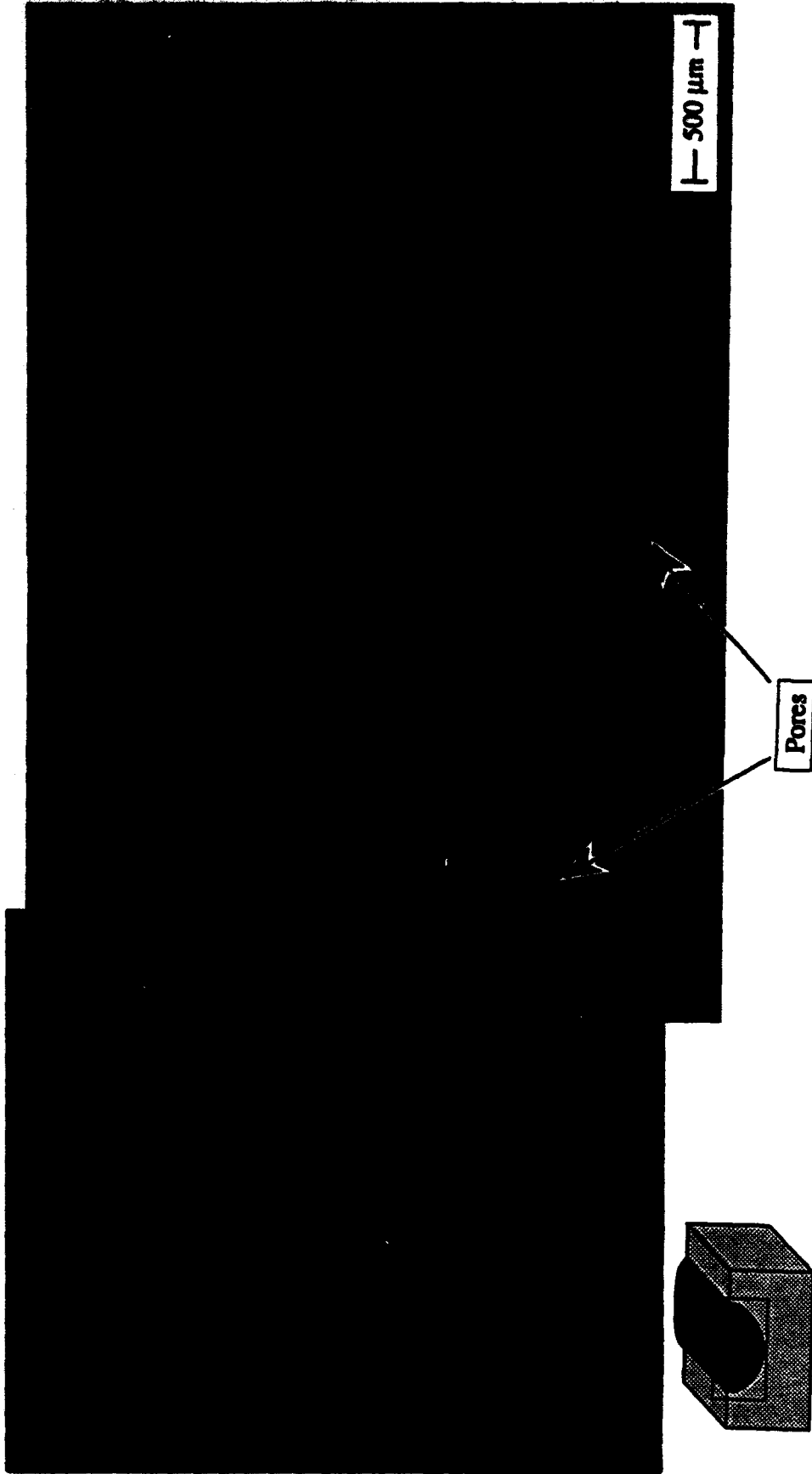
Figure 25. GTA weld made on the 6061/SiC/20w composite, showing aluminum carbide platelets, pores in the fusion and heat affected zones, and a large weld crown.
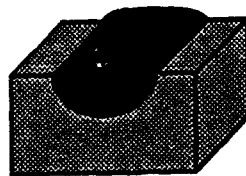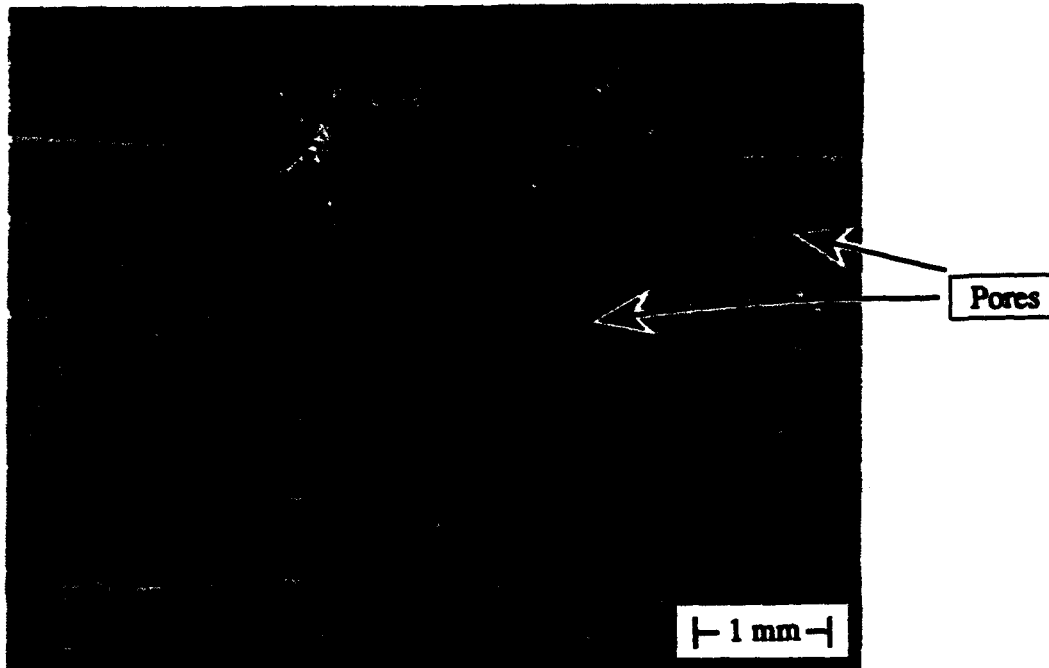
Figure 26. Macrograph of a GTA weld made on the 6061/SiC/20w composite showing porosity in the heat affected zone.
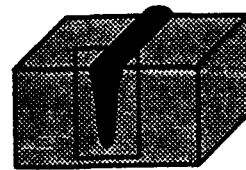
Figure 27. Laser beam weld made on the A356/SiC/20p composite showing aluminum carbide platelets and a large weld crown (1500W, helium shielding gas).
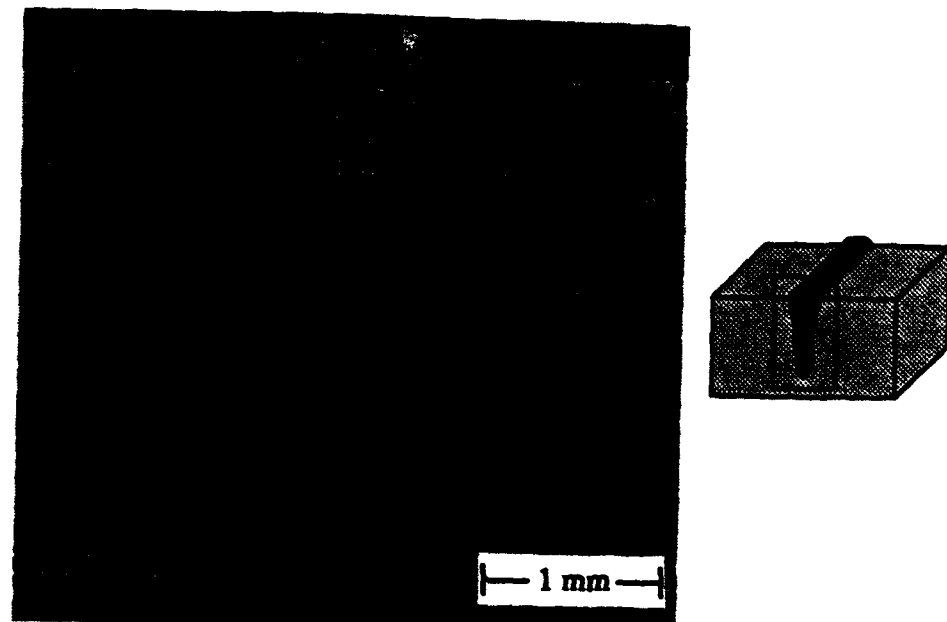
Figure 28. Laser beam weld made on the A356/SiC/20p composite.
(Unetched)
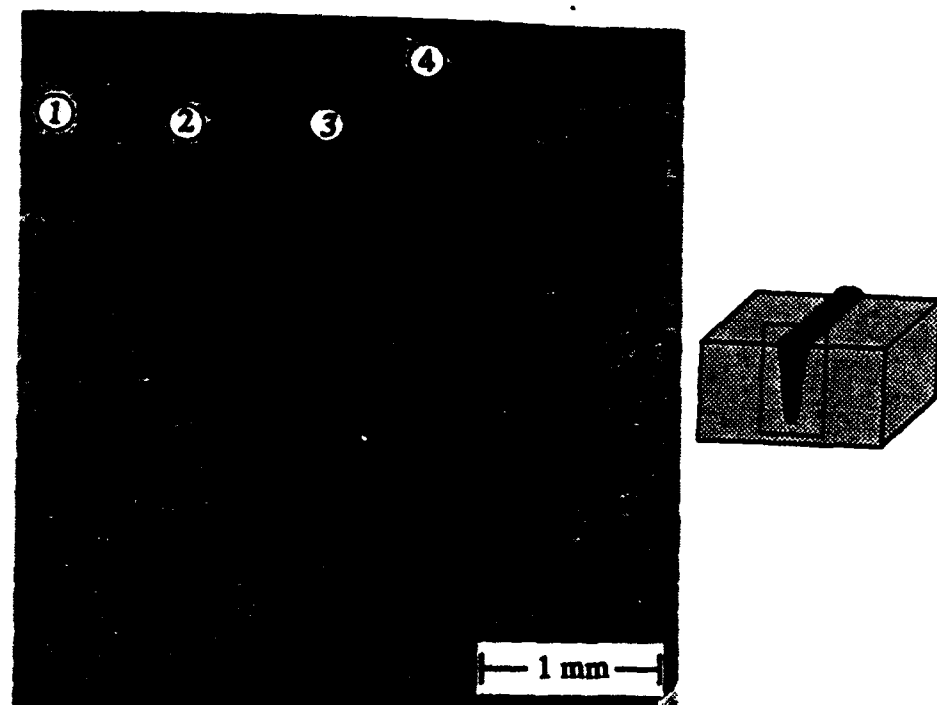
Figure 29. Laser beam weld made on the A356/SiC/20p composite.
(Keller's Etch)
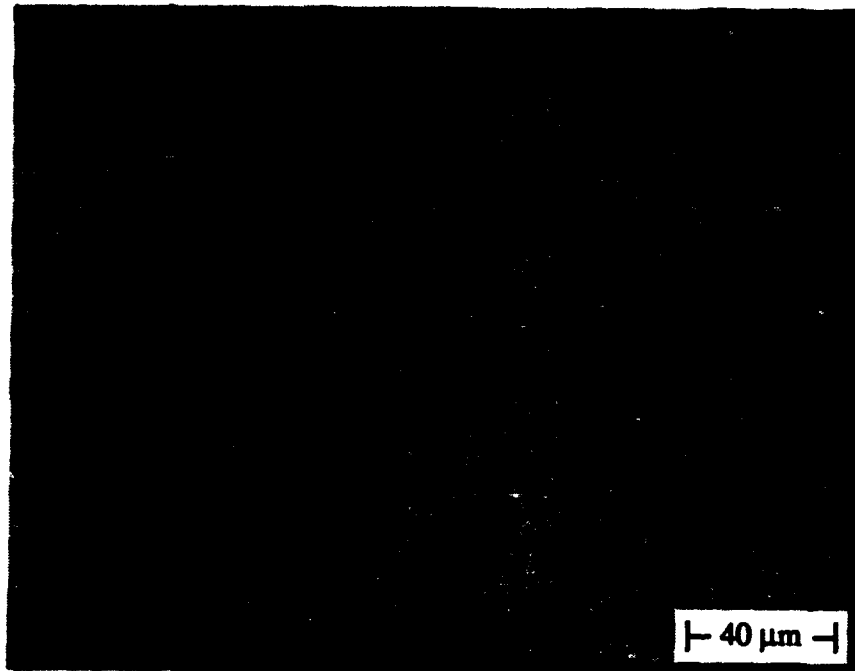
Figure 30. Region 1 of the laser beam weld made on the A356/SiC/20p composite showing the large solidified structure of the as-cast material.
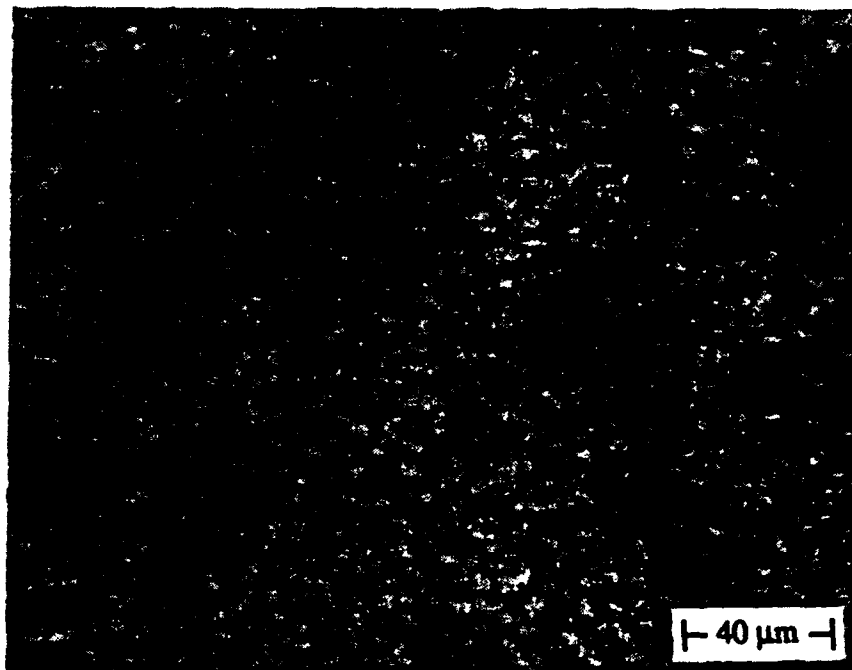
Figure 31. Region 2 of the laser beam weld made on the A356/SiC/20p composite showing the fine solidified structure of the fusion zone.
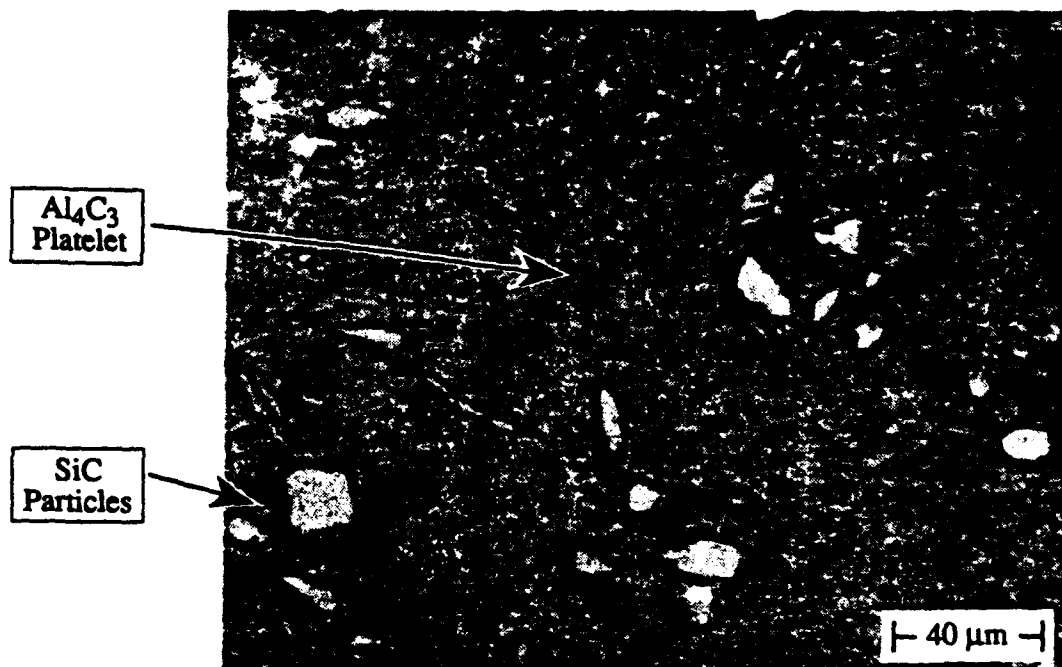
Figure 32. Region 3 of the laser beam weld made on the A356/SiC/20p composite. Both silicon carbide and aluminum carbide are present in this region.
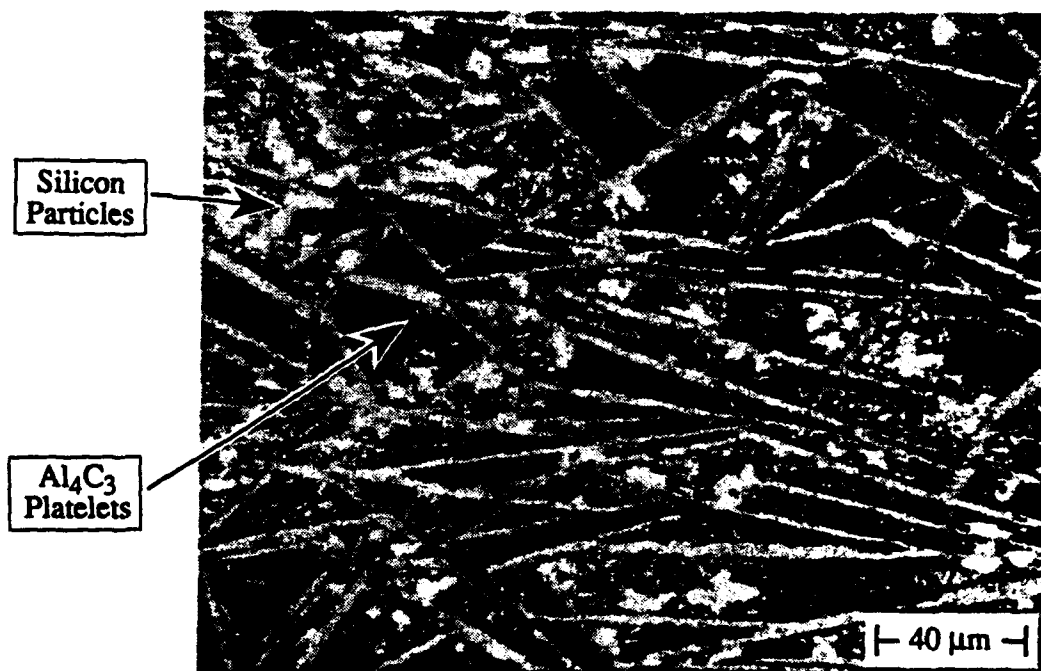
Figure 33. Region 4 of the laser beam weld made on the A356/SiC/20p composite. All the SiC has reacted to form Al_4C_3. Silicon particles are also evident in this region.

The GTA weld on the A356/SiC/20p composite exhibits a wide shallow weld that is characteristic of the process, Figure 34. The low weld pool temperature provided by the arc welding process in combination with the silicon content of the matrix was successful in preventing the formation of aluminum carbide on this composite. No aluminum carbide was observed in the fusion zone. The microstructure of the fusion zone has a small solidified structure that is similar to that observed in Region 2 of the laser beam weld on this material, shown in Figure 35.

Porosity was often observed in the heat affected zones and fusion zones of both arc and laser beam welds, as well as in the heat affected zones of laser cuts. As mentioned previously, the porosity evident in the 6061/SiC/20w can be attributed to P/M fabrication, while the porosity in the A356/SiC/20p composite may be due the HiPIC fabrication. The porosity evident in the heat affected zones of welds made on the 6061/SiC/20w composite was often oriented. The microstructure of the as-received 6061/SiC/20w composite provided insight in to the orientation of the porosity, since the composite is very different in the three directions, as shown in Figure 36. The variation in microstructure is most likely due to extrusion of the composite. Composites reinforced with whiskers or short fibers are often extruded to align the fibers to some extent. Although extrusion can improve the mechanical properties, it tends to lower the fiber aspect ratio and leads to the banding of the matrix in the material [3]. As is evident from the microstructure shown in Figure 36, the banded matrix regions can be quite large. These matrix rich areas are believed to be the source of porosity in the heat affected zone of the welded composite, since the porosity appears to form at these matrix rich areas, as evidenced by the micrograph of the arc weld made on this material, Figure 37. This observation is in agreement with the experiments done by Ahearn [16], where it was found that hydrogen in the aluminum alloy was responsible for the porosity observed in the welds and heat affected zones.
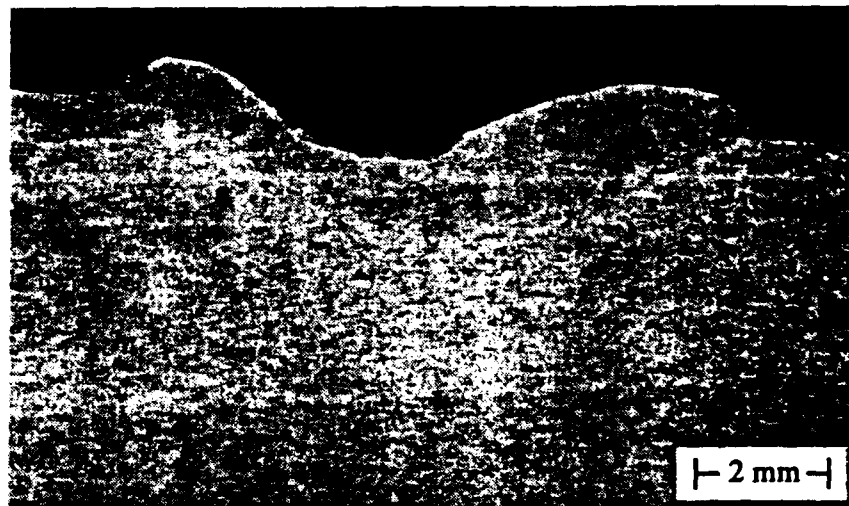
Figure 34. Macrograph of a GTA weld made on the A356/SiC/20p composite.
(Keller's Etch)
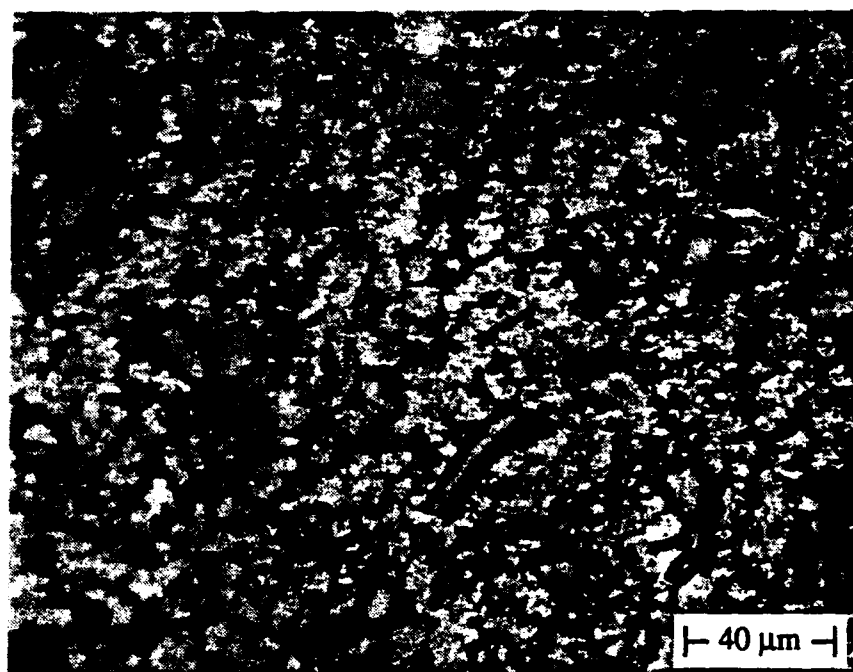
Figure 35. Microstructure of the fusion zone of a GTA weld made on the A356/SiC/20p
composite. (Keller's Etch)
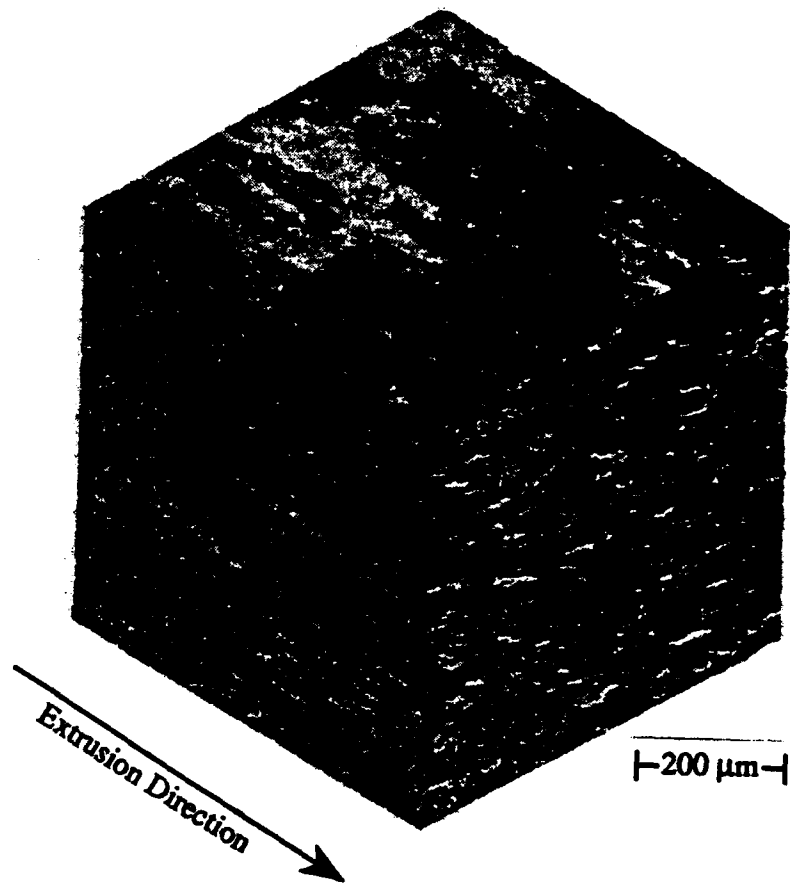
Figure 36. Microstructure of the as-received 6061/SiC/20w composite.
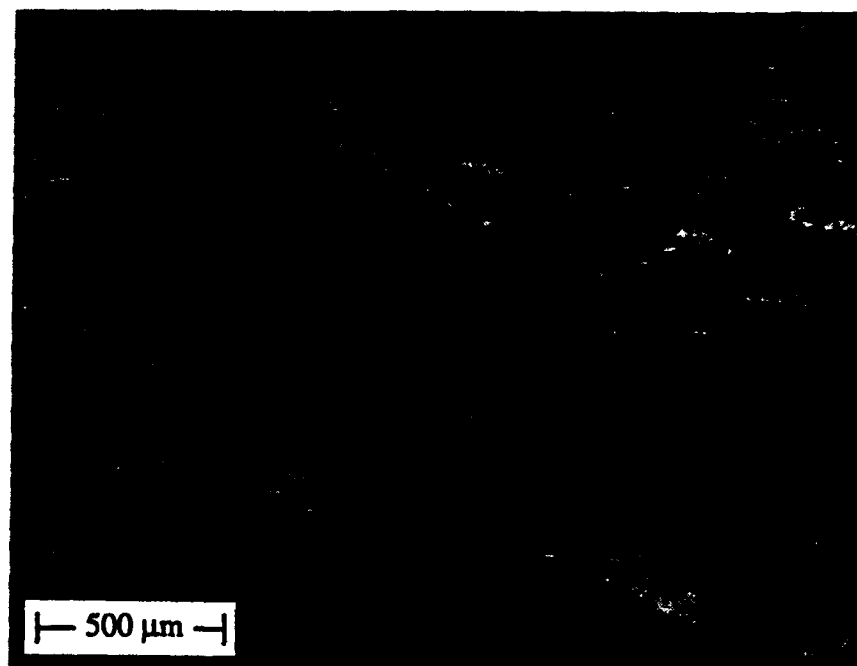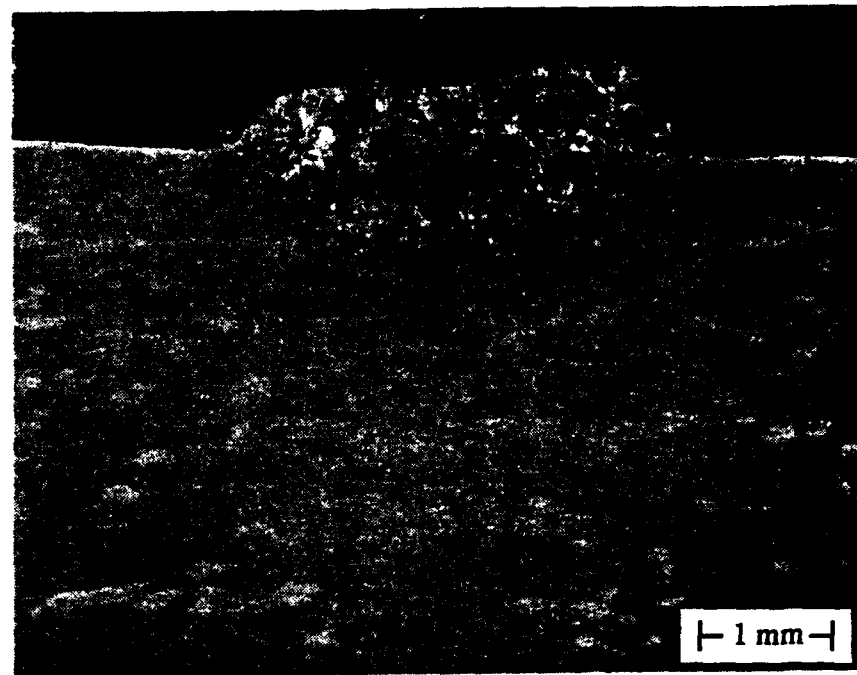
Figure 37. Pores formed in the heat affected zone of a GTA weld made on the 6061/SiC/20w composite. The pores appear to form in the banded regions containing high concentrations of matrix.

A micrograph of an autogenous laser beam weld made on the A356/SiC/20w composite exhibits substantial amounts of porosity in the fusion and heat affected zones in addition to the formation of aluminum carbide, Figure 38. The porosity, also observed in laser cuts on this material, is attributed to hydrogen in the as-fabricated composite, that forms pores in the material upon heating. This is believed to be similar to the behavior observed in P/M fabricated DRA composites. The porosity in the laser beam welds on the A356/SiC/20w composite was oriented along the layers of the silicon carbide whisker preform that was infiltrated to form the material.

4.2.3. Filler Metals

Although the use of certain metals has been shown to prevent the formation of aluminum carbide in other situations, it was necessary to determine if use of these metals would be applicable for laser beam welding and if the metals could prevent the formation of aluminum carbide. Based on free energy data, the mechanical, physical, and chemical properties of metals whose carbides are more thermodynamically stable than aluminum carbide were investigated. A chemical equilibrium analysis of amount of filler metal necessary to prevent the formation of aluminum carbide was generated, using the SOLGASMIX computer program. Welds were made on the 6061/SiC/20w composite using titanium and zirconium additions for comparison to the thermodynamic analysis and for microstructural characterization.

62
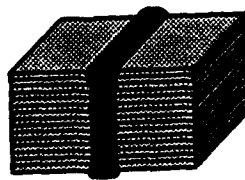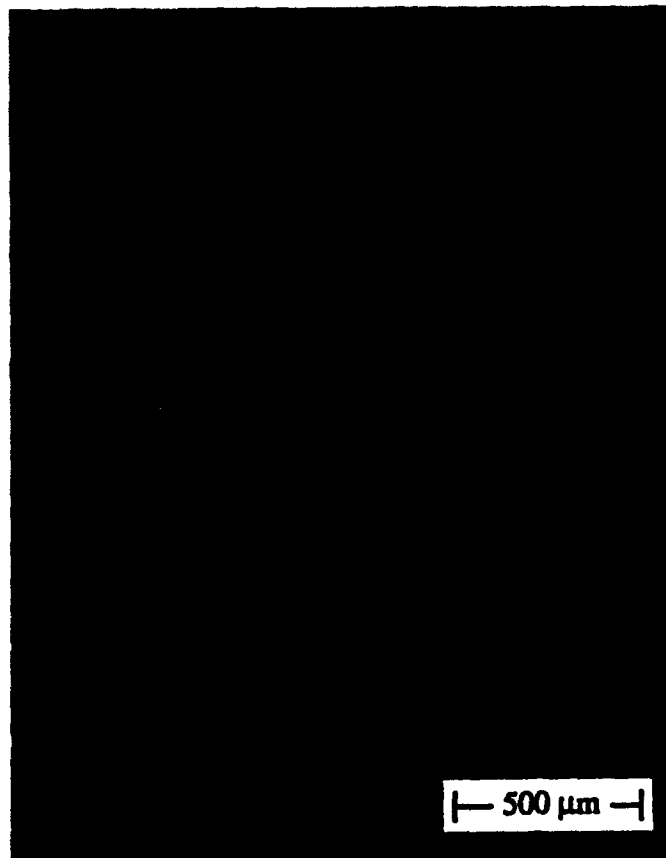
Figure 38. Formation of porosity in the fusion and heat affected zone of a laser weld made on the A356/SiC/20w composite.

4.2.3.1. Analysis of Carbide Formation

Free energy of formation data indicates that several metallic carbides are more likely
to form in preference to aluminum carbide [59]. Titanium and zirconium show the most
promise in eliminating the formation of aluminum carbide based on free energy change, as
shown in Figure 39. Titanium carbide and zirconium carbide are chemically stable
compounds that are not subject to dissolution in water [32]. The properties of titanium and
zirconium carbide are similar to those of silicon carbide; as shown in Table 4. Calculations
show that the formation of titanium and zirconium carbide from silicon carbide result in
volume expansion of five and three percent respectively, much less than the twenty-five
percent expansion due to the formation of aluminum carbide. Although the properties of
titanium and zirconium carbides are similar to that of silicon carbide, experimentation and
analysis was necessary to verify the formation of these compounds and to characterize the
microstructure of the fusion zone.

Table 4. Properties of Metallic Carbides [60].

Material	Elastic Modulus (GPa)	Microhardness (HV: kg/mm^2)	Thermal Expansion (10^{-6}/ K)
SiC (CVD)	420	3000	5.5
TiC	447	3200	7.2
ZrC	406	2600	6.3
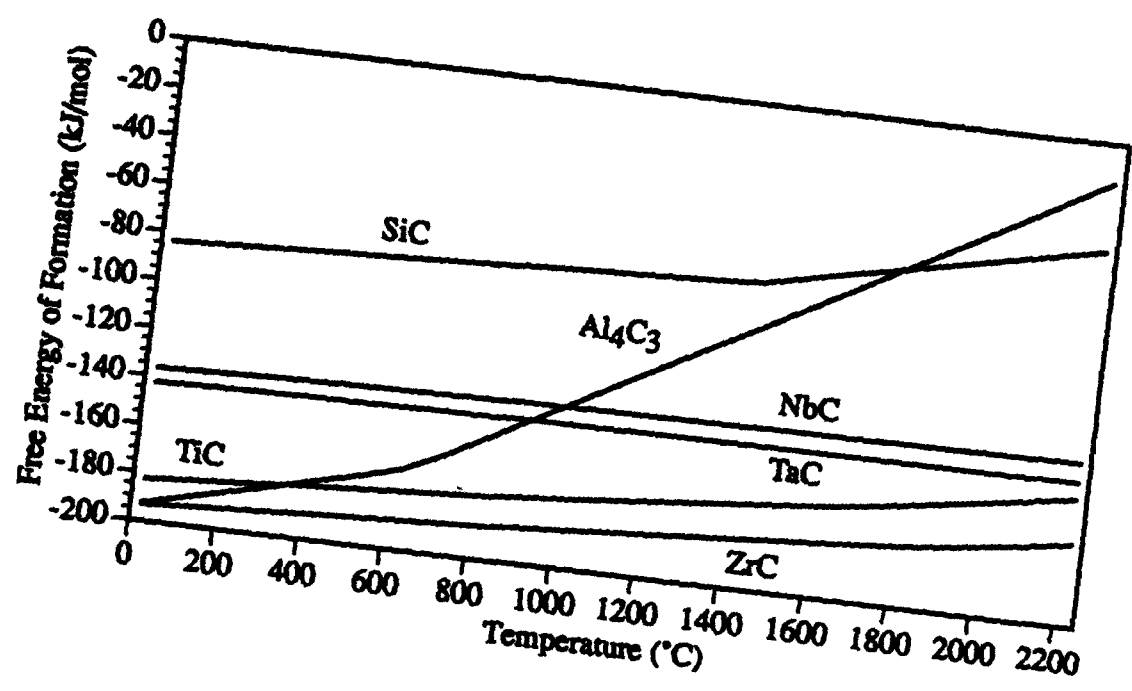
Figure 39. Free energy of formation for several metallic carbides.

4.2.3.2.   Chemical Equilibrium Analysis

Analysis of chemical equilibrium for the addition of filler metal to the fusion zone of the Al/SiC composite begins with the chemical reactions believed to occur in the system. The reaction between aluminum and silicon carbide to form aluminum carbide has been observed and documented [24-30].

$$4Al_{(\ell)} + 3SiC_{(s)} \rightarrow Al_4C_{3(s)} + 3Si_{(s)} \qquad (3)$$
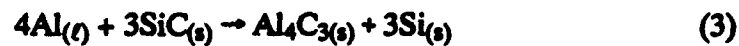
Titanium reacts with the silicon carbide by the following reaction.

$$Ti_{(\ell)} + SiC_{(s)} \rightarrow TiC_{(s)} + Si_{(s)} \qquad (4)$$

Combining reactions 3 and 4 leads to the following reaction.

$$Al_4C_{3(s)} + 3Ti_{(\ell)} \rightarrow 3TiC_{(s)} + 4Al_{(\ell)} \qquad (5)$$
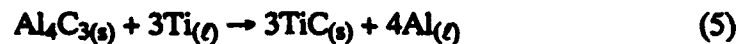
The free energy of reaction 5 will determine if aluminum carbide or titanium carbide is favored thermodynamically. If the free energy is negative, titanium carbide is favored; if positive, aluminum carbide is favored. The total free energy of reaction can be determine by the free energy of the reaction in the standard state and the equilibrium constant for the reaction.

$$\Delta G_{Rxn} = \Delta G^0_{Rxn} + RT \ln(K) \qquad (6)$$

The equilibrium constant, K, for reaction 5 is as follows.

$$K = \frac{a_{Al}^4 \, a_{TiC}^3}{a_{Ti}^3 \, a_{Al_4C_3}} \qquad (7)$$

Assuming that the aluminum and titanium carbides are pure and remain in their standard state in the system; the activities of these compounds can be considered to be unity [61]. Using these assumptions the equilibrium constant can thereby be reduced to the following.

$$K = \frac{a_{Al}^4}{a_{Ti}^3} \tag{8}$$

To determine the equilibrium for reaction 5, the activities of titanium and aluminum in solution must be specified, based on the amounts of each present in the system. The activity of titanium in solution with aluminum has been determined experimentally for the binary system of Ti-Al for a composition range of 0.6 to 1.0 mole fraction of titanium [62]. The researchers developed an equation for the activity of titanium as a function of composition and temperature using experimental data. The developed equation shown in Figure 40 reveals the deviations from the ideal solution behavior (Raoult's Law) due to the attraction between the aluminum and titanium atoms.

One major problem in the determination of the chemical equilibrium of a system is the failure to include all possible compounds that can form in the system. For equation 5, no titanium intermetallics are considered, yet those and other compounds have been observed in the Al-Ti-C system [38], and have the potential to form in the current system. Therefore, it was necessary to develop a more detailed analysis that included all possible compounds to obtain the most accurate results. A modified version of a thermodynamic analysis program, SOLGASMIX, was used to determine the amounts of filler metal additions necessary to prevent the formation of aluminum carbide. SOLGASMIX determines the chemical equilibrium of a system through the minimization of free energy [63]. The program has been modified to include an interface with the JANAF Thermochemical Data Tables [59] to provide a large data base of compounds for solving chemical equilibrium problems [63]. One subroutine of the SOLGASMIX program checks
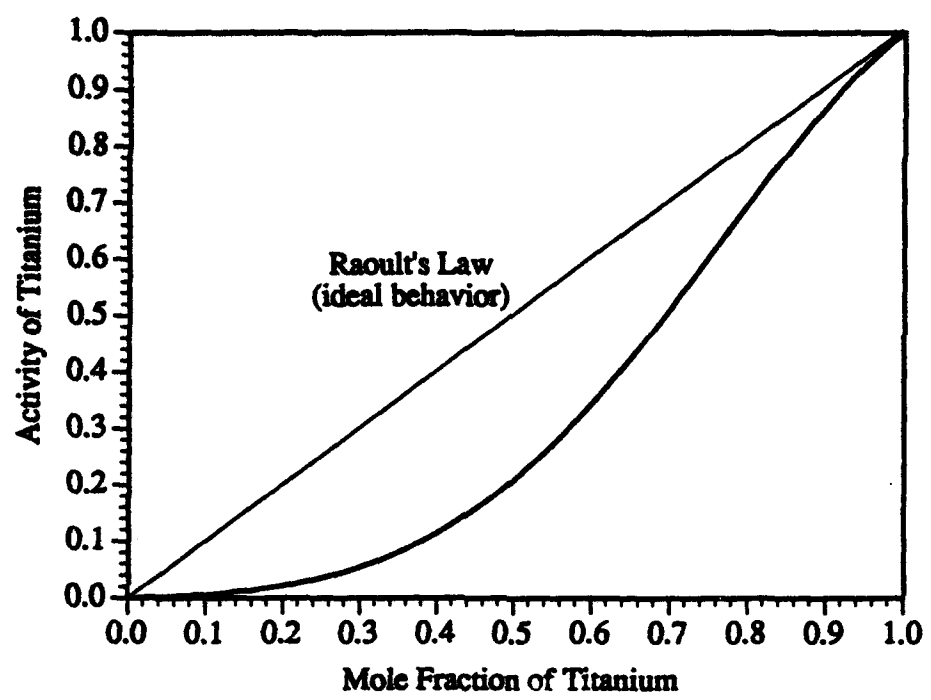
Figure 40. Titanium activity as a function of mole fraction for the Al-Ti system at 1750 K [62]. The deviation from Raoult's Law (ideal behavior) is due to the attraction between the aluminum and titanium atoms.

the data base and lists all possible compounds formed from the constituent elements for the system. The output for the Al-C-Si-Ti system revealed that several compounds known to form were not present in the data base. It was necessary to obtain free energy of formation data for these compounds to provide the most accurate analysis of the system. The possible compounds known to form in the Al-C-Si-Ti system from various sources [64-72], along with the availability of data for the compounds are shown in Table 5. Unfortunately, not all the necessary data for the analysis was available and therefore could not be included in the computer analysis. In addition, there was some variation in the reported free energy data for several of the titanium aluminide compounds [39, 69, 72]. A single source of free energy data for the compounds in the Ti-Al system [69] was chosen for the SOLGASMIX data base. The need for activity data for titanium and aluminum in solution has been mentioned previously; however the activities of the other components in the system were also required. The most accurate analysis would be provided by the activity data for the components of the quaternary system; however none was available. Available activity data was limited to the binary systems of Ti-Al (titanium in solution with aluminum) [62] and Al-Si [65]. The activity data for titanium in solution in aluminum was provided in the form of an equation; however the activity data for the Al-Si system was fitted to the quasi-chemical solution model to obtain equations for the activity as a function of composition. The lack of any data for the activity of zirconium in aluminum prevented a SOLGASMIX analysis of zirconium additions to the silicon carbide reinforced aluminum composite. The predictions for the titanium additions are believed to be similar to those for the zirconium additions, since the free energies of formation for the two carbides are similar.

Table 5. Compounds in the Al-C-Si-Ti system and the Availability of Free Energy Data.

Possible Compounds	Initial Database	Modified Database
Elements		
Al	✓	✓
C	✓	✓
Si	✓	✓
Ti	✓	✓
Al-C Phase Diagram [62]		
Al₄C₃	✓	✓
Al-Si Phase Diagram [63]		
none	-	-
C-Si Phase Diagram [64]		
SiC	✓	✓
C-Ti Phase Diagram [65]		
Ti₂C		X
TiC	✓	✓
Si-Ti Phase Diagram [66]		
Ti₃Si		✓
Ti₅Si₃		✓
Ti₅Si₄		✓
Ti₆Si₅		X
TiSi		✓
TiSi₂		✓
Ti-Al Phase Diagram [67]		
Ti₃Al		✓
TiAl		✓
Ti₂Al₅		✓
TiAl₂		✓
TiAl₃		✓
Al-Si-C Phase Diagram [68]		
Al₈SiC₇		X
Al₄SiC₄		X
Al₄Si₆C₅		X
Al-C-Ti Phase Diagram [69]		
Ti₂AlC		X
Ti₃AlC		X

Once all the available data was added to the data base, an example was run to provide verification to further analysis. The example involved the A356/SiC/20p composite. Experiments determined that aluminum carbide began to form at approximately 1060 K [35]. The result of the thermodynamic analysis can be seen in Figure 41. The aluminum begins to react with the silicon carbide, forming aluminum carbide and silicon at a temperature of 1092 K. As the temperature increases, the reaction proceeds, until all the silicon carbide has reacted at approximately 1800 K. The SOLGASMIX analysis prediction of aluminum carbide formation at 1092 K is somewhat higher, but agrees reasonably well with the temperature of approximately 1060 K, observed previously [35].

The thermodynamic analysis of the A356/SiC/20p composite can clarify the microstructure observed in the laser beam weld made on this material, shown in Figure 42. The etched microstructure reveals several different regions in the weld, corresponding to different temperatures. The temperatures in the weld pool are highest in the center (nearest the laser beam) and decrease as the distance from the weld center increases. The microstructure of the center of the weld, containing only aluminum carbide, silicon, and aluminum suggests weld pool temperatures in excess of 1800 K, based on the thermodynamic analysis. At temperatures between 1800 to 1100 K, both aluminum carbide and silicon carbide coexist. From 1100 to 828 K, molten aluminum and silicon carbide are stable. The temperatures of 828 (the alloy liquidus) and 1800 K (total conversion of SiC to Al_4C_3) are clearly defined, however the 1100 K isotherm cannot be determined accurately from the microstructure.
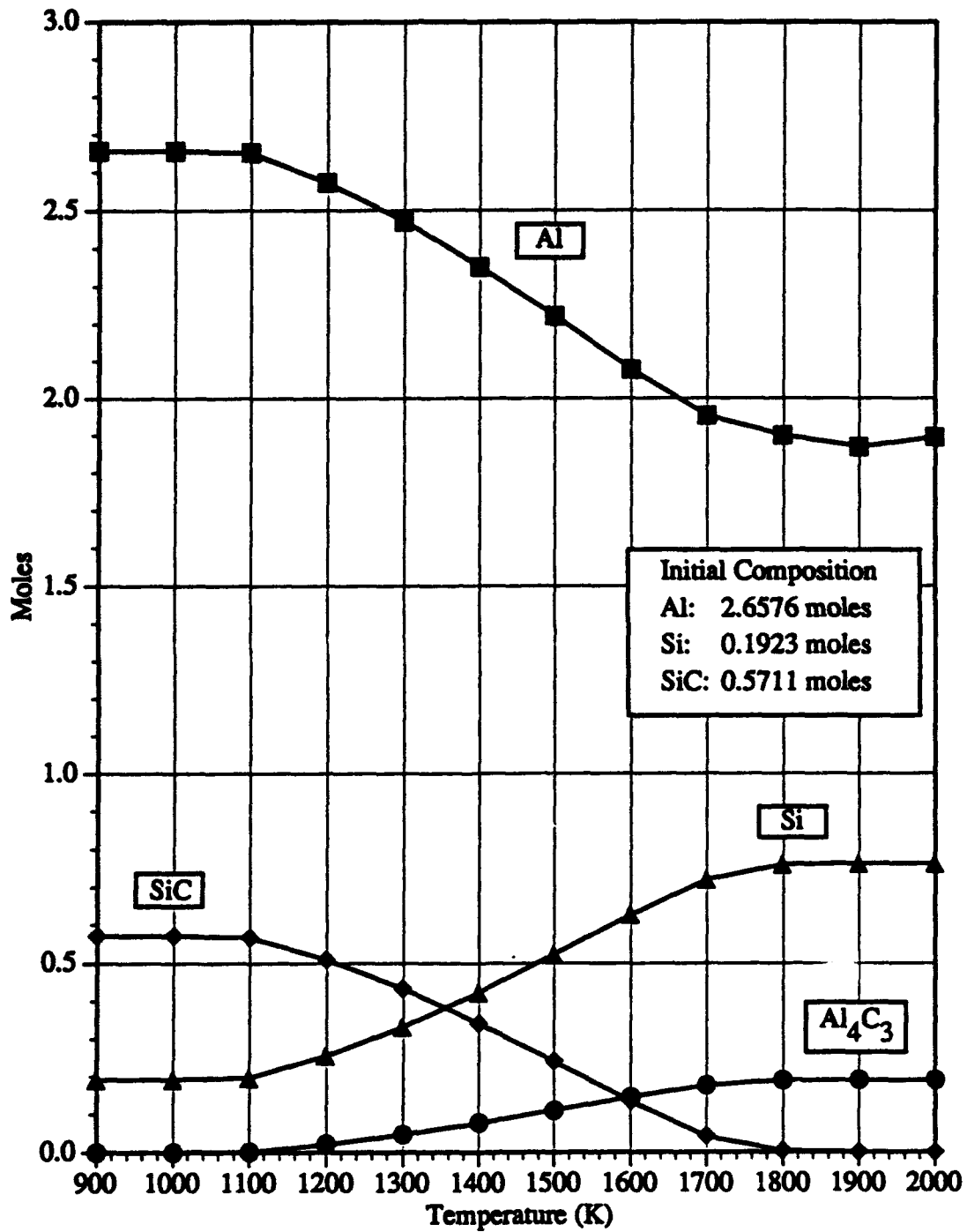
Figure 41. Thermodynamic analysis predictions of the compounds present as a function of temperature for a Al-7Si/SiC/20 composite.
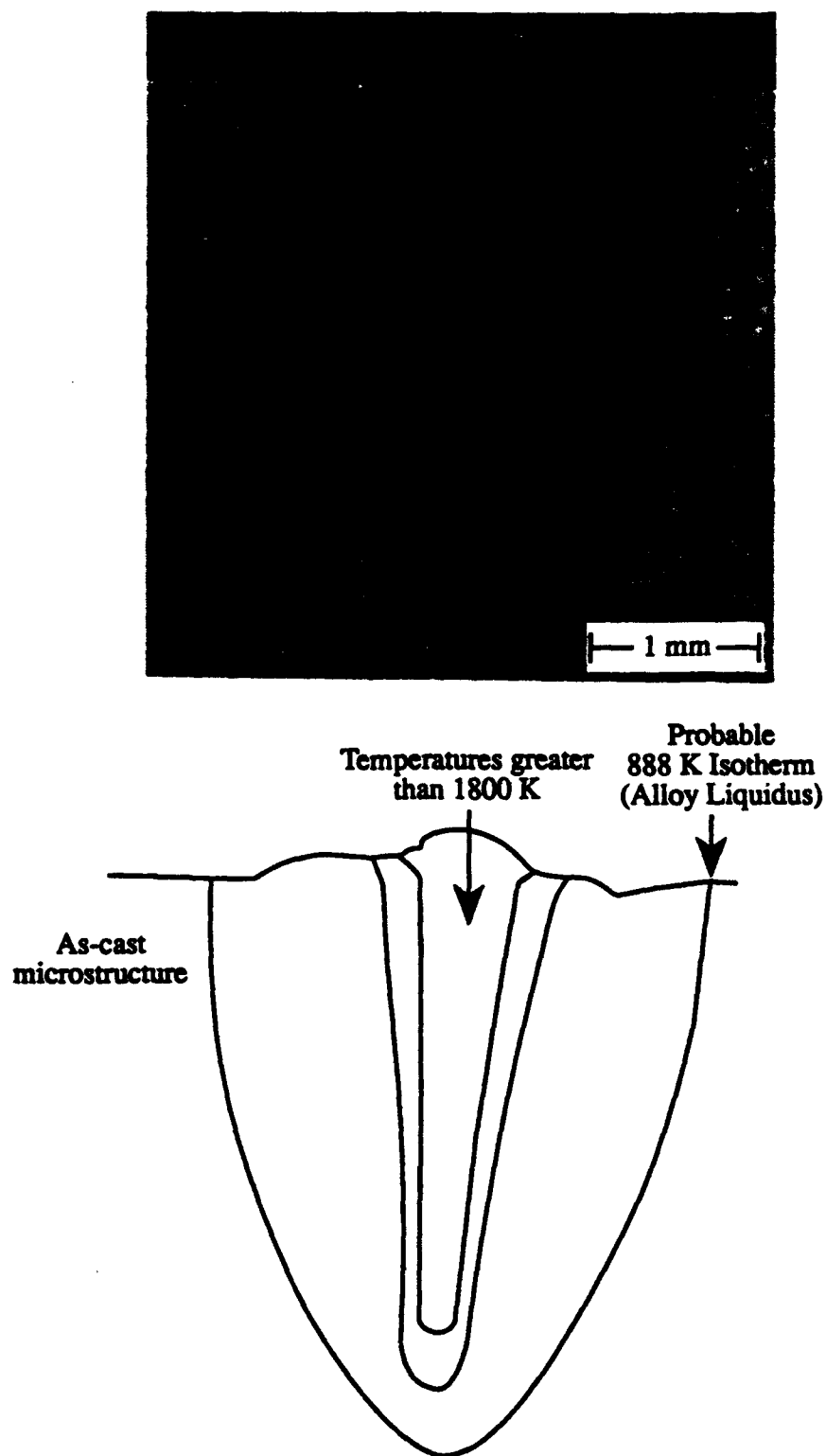
Figure 42. Comparison of the microstructure of the laser beam weld made on the A356/SiC/20p composite to the computer predictions from the SOLGASMIX analysis of the composite.

One very important factor not addressed by the SOLGASMIX thermodynamic analysis is the reaction kinetics. According to the thermodynamic analysis, aluminum carbide formed at higher temperatures should revert to silicon carbide upon cooling; however, this is not observed experimentally. The aluminum carbide formed at higher temperatures remained in the weld upon solidification. From this observation it can be concluded the kinetics for the aluminum carbide to revert to silicon carbide are slow relative to the cooling rate of the weld.

SOLGASMIX analyses for the addition of titanium to a Al/SiC/20 model composite were run to determine the optimal level of addition to the fusion zone to prevent the formation of aluminum carbide. The analyses determined that a 22 wt% (15 vol%) addition of titanium to the fusion zone is necessary to prevent aluminum carbide formation. The compounds formed as a function of temperature are shown in Figure 43, along with the initial composition. Aluminum is not included in the Figure to provide better resolution for the other compounds. The titanium reacts with the silicon carbide, resulting in the formation of titanium carbide and silicon. The amounts of titanium carbide and silicon (right hand scale) are equal throughout the entire temperature range. The silicon carbide and titanium remaining at 960 K, (left hand scale) continue to react until 1200 K, where all the silicon carbide has reacted. No titanium intermetallics or aluminum carbide are predicted for this level of titanium addition.

For titanium levels below 22 wt%, the formation of aluminum carbide is predicted to occur. An analysis for a 10wt% (6.5 vol%) addition of titanium to the fusion zone, Figure 44, shows the compounds formed in the system as a function of temperature. Initially, the titanium in the system reacts with the silicon carbide to form titanium carbide and silicon. The remaining silicon carbide begins to react with the molten aluminum at 1100 K to form aluminum carbide. The reaction continues as the temperature increases until 1500 K, where all the silicon carbide has reacted to form aluminum carbide.
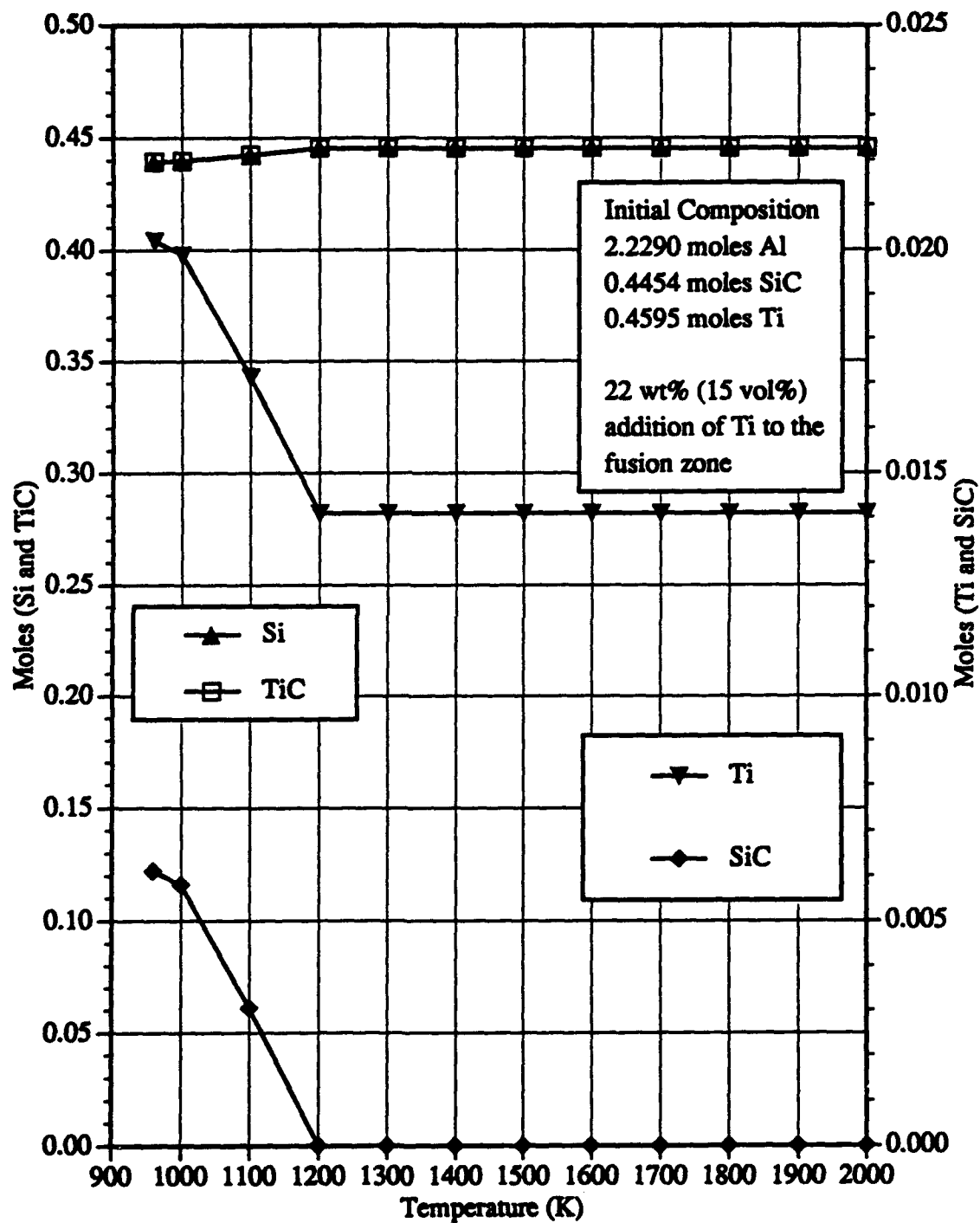
Figure 43. Thermodynamic analysis predictions of the compounds present as a function of temperature for a 22 wt% addition of titanium to a Al/SiC/20 composite.
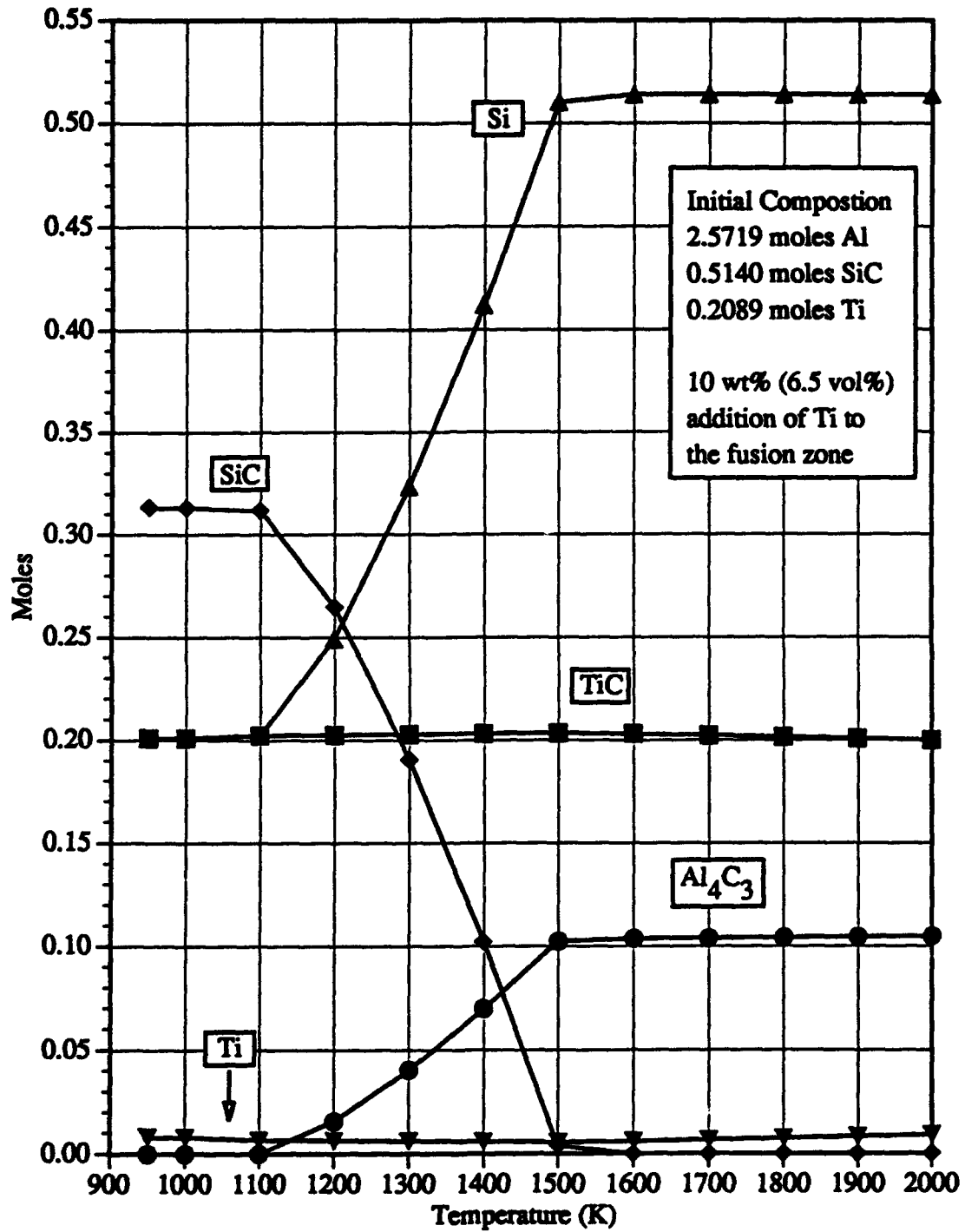
Figure 44. Thermodynamic analysis predictions of the compounds present as a function of temperature for a 10 wt% addition of titanium to a Al/SiC/20 composite.

The analysis for a 30 wt% (21vol%) addition of titanium to the fusion zone, Figure 45, shows the compounds formed in the system as a function of temperature. The titanium in the system reacts with the silicon carbide to form titanium carbide and silicon. The silicon produced reacts with the excess titanium to form TiSi. As the temperature increases the amount of TiSi decreases until it reaches zero at 1300 K.

4.2.3.3. Microstructure

Thin shims of titanium and zirconium were placed between two plates of the 6061/SiC/20w composite in the manner previously described and were laser welded. Different shim thicknesses were used to vary the level of filler metal addition to the fusion zone. These welds were characterized for the microstructure and for comparison to the thermodynamic analysis. Several different thicknesses of titanium shims, ranging from 64 to 582 μm, were used in the study. The zirconium shims used varied in thickness from 40 to 127 μm. In order to compare the experimental welds made with titanium to the thermodynamic analysis, the widths of the weld fusion zones were compared to the initial shim thickness. The comparison provides an indication of the volume fraction of the filler metal present in the weld. The volume fraction cannot be determined accurately by this technique, since volumetric changes may occur upon mixing and as a result of chemical reactions. For the purposes of comparison to the thermodynamic analysis, this approximation is necessary. Shown in Figure 46 are the widths of the fusion zone compared to the thickness of the titanium shim and the approximate volume fraction of titanium in the experimental welds. The fusion zone width, initial zirconium shim thickness, and approximate fraction of zirconium in the welds are shown in Figure 47 for comparison.
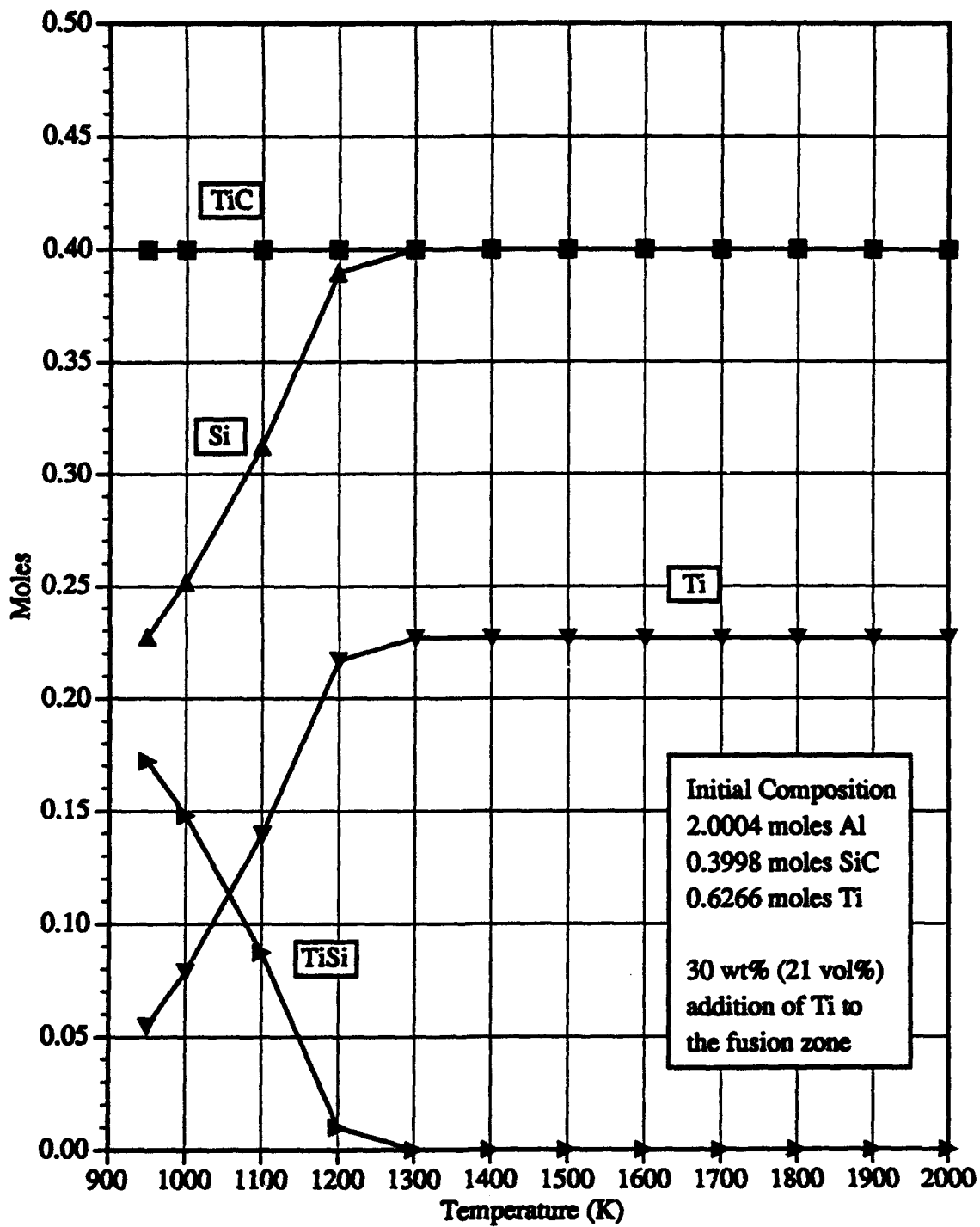
Figure 45. Thermodynamic analysis predictions of the compounds present as a function of temperature for a 30 wt% addition of titanium to a Al/SiC/20 composite.

Weld Specimen	Shim Thickness (μm)	Fusion Zone Width (μm)	Volume Fraction Titanium (percent)
Ti:A	582	1100	53
Ti:B	127	700	18
Ti:C	64	600	11
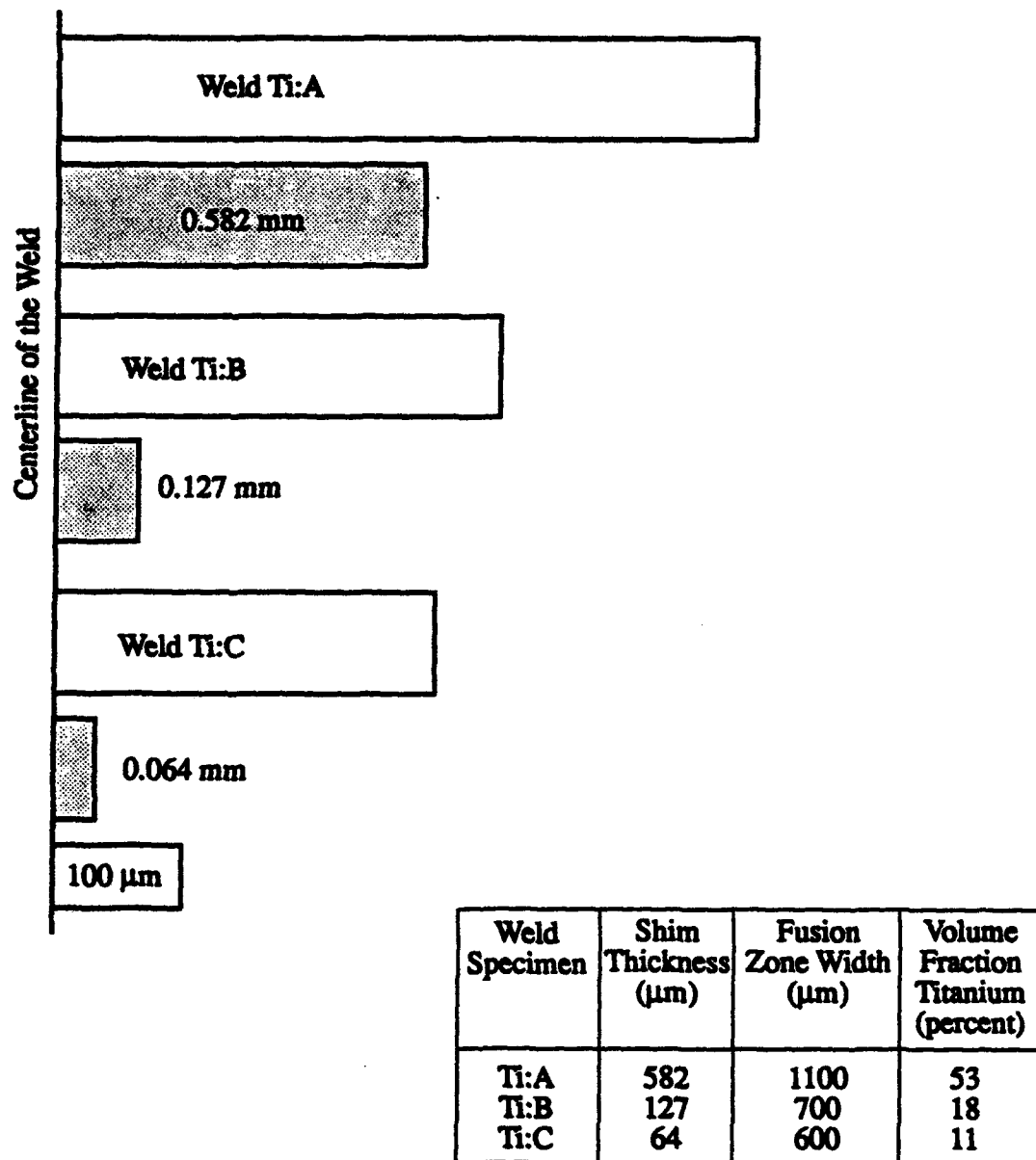
Figure 46. Widths of the fusion zone, initial shim thickness, and the volume fraction of titanium for welds made on the 6061/SiC/20w composite.
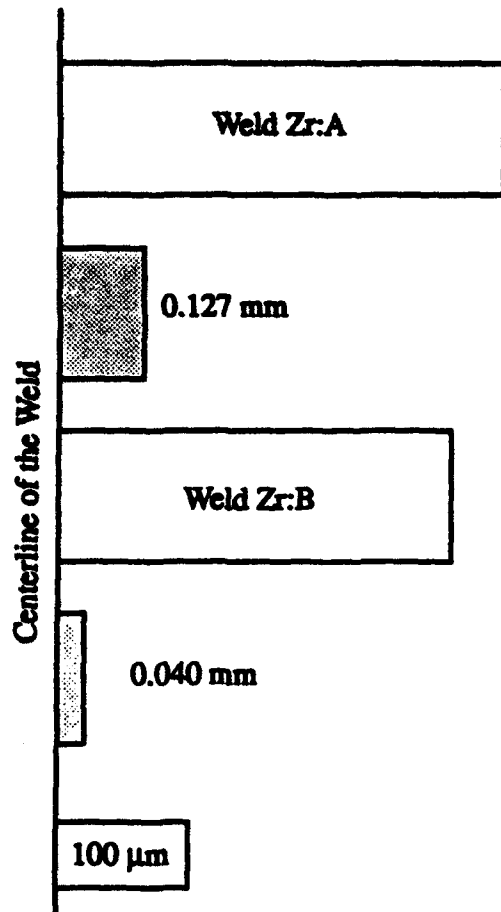
Weld Specimen	Shim Thickness (μm)	Fusion Zone Width (μm)	Volume Fraction Zirconium (percent)
Zr:A	127	675	18
Zr:B	40	600	11

Figure 47. Widths of the fusion zone, initial shim thickness, and the volume fraction of zirconium for welds made on the 6061/SiC/20w composite.

From the approximate volume fraction data for titanium shown in Figure 46 and the thermodynamic analysis, the composition of the fusion zones can be predicted. Weld Ti:A (582 μm Ti shim) contains a greater amount of titanium than necessary to prevent the formation of aluminum carbide. The formation of titanium carbide is predicted, as well as the possible formation of titanium silicide, no aluminum carbide is predicted. Weld Ti:B (127 μm Ti shim) has a level of titanium slightly higher than that predicted to prevent the formation of aluminum carbide. In this case the formation of titanium carbide and possibly some titanium silicide is predicted. For Weld Ti:C (64 μm Ti shim) the level of titanium is less than that necessary to prevent the formation of aluminum carbide; the formation of aluminum carbide as well as some titanium carbide should be present in the fusion zone.

The fusion zone of Weld Ti:A did not exhibit the formation of aluminum carbide platelets that have been observed in autogenous welds as expected by the thermodynamic anlaysis, as shown by the comparison of welds (Figure 48). Although aluminum carbide platelets did not appear in the microstructure of the fusion zone, several other structures were observed, including fine dendrites, nodular regions near the edge of the fusion zone, and long band-like structures, also located near the edge of the fusion zone. The dendrites observed in the microstructure, shown in Figure 49, were small (1-5 μm) and well dispersed throughout the fusion zone. An SEM image of the dendrites and corresponding X-ray maps of those dendrites (Figure 50) obtained by EPMA, suggest that these dendrites are titanium carbide, since only titanium and carbon, and not aluminum or silicon are present. The morphology of the titanium carbide dendrites is nearly identical to that observed in Ti-TiC composites, studied by Chen, Geng, and Chin [73]. Also evident in the X-ray maps is the high amount of titanium present in the matrix surrounding the dendrites. EPMA of the fusion zone, provided the elemental composition of the fusion zone, shown in Table 6.

├─200 μm─┤
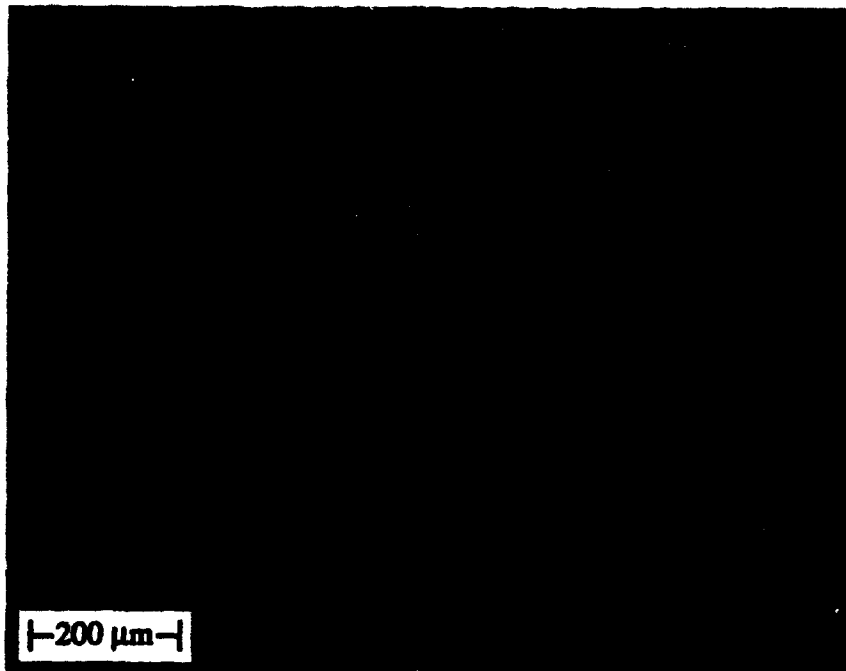
Figure 48.1. Optical micrograph of the fusion zone of an autogenous laser beam weld made on the 6061/SiC/20w composite, showing aluminum carbide platelets in the fusion zone.

├─200 μm─┤
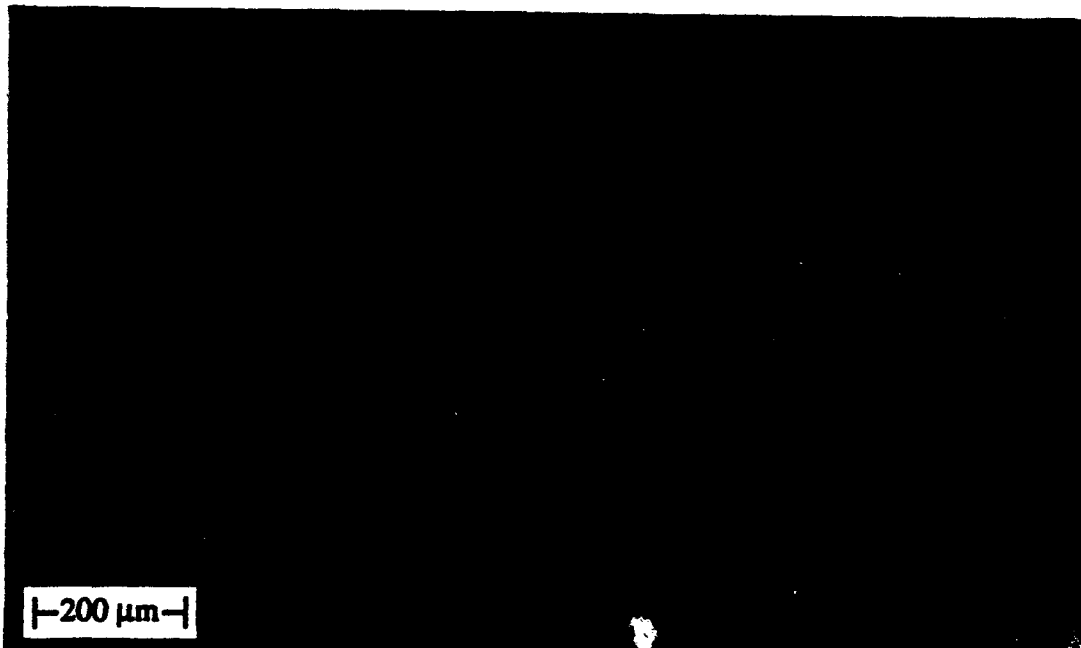
Figure 48.2. Optical micrograph of the fusion zone of a laser beam weld made on the 6061/SiC/20w composite (Weld Ti:A) showing that the formation of aluminum carbide platelets has been suppressed.

82
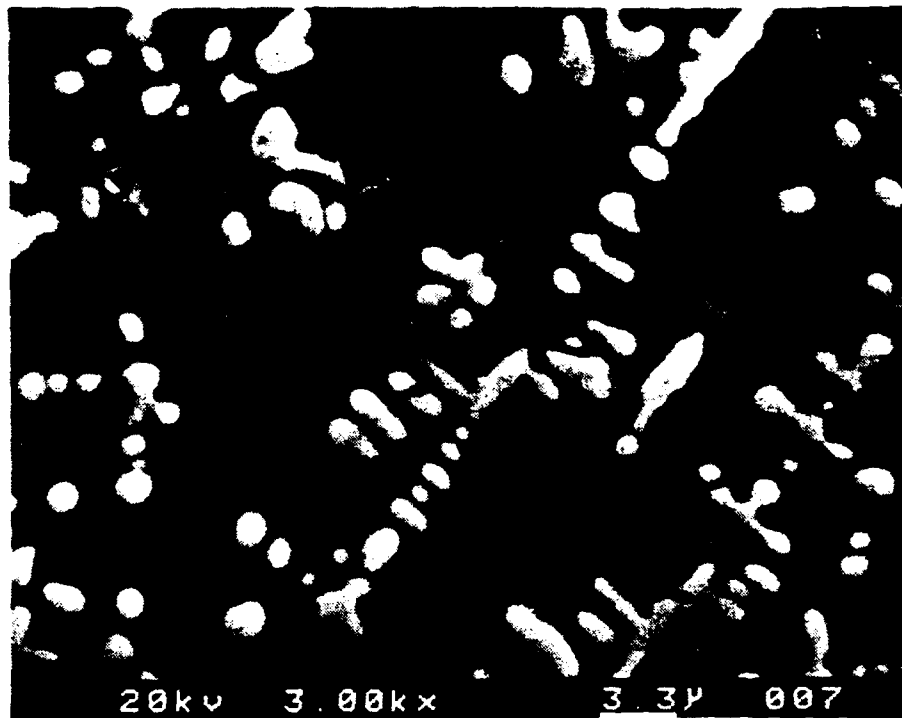
Figure 49. Dendrites present in the fusion zone of the 6061/SiC/20w composite welded with a 0.582 mm thick titanium filler addition.

Figure 50.1. SEM image of the dendrites in the fusion zone of the 6061/SiC/20w composite welded with a 0.582 mm thick titanium shim.
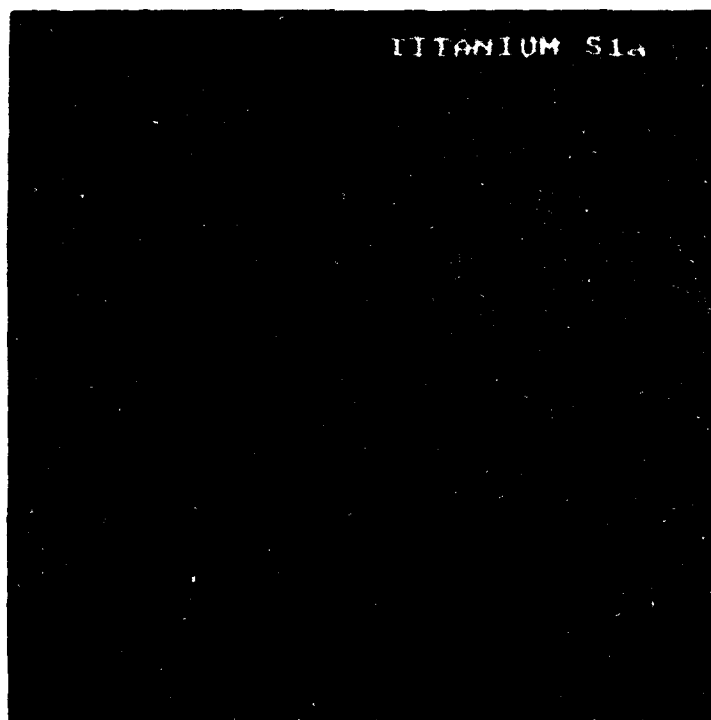
Figure 50.2. X-ray map of titanium.
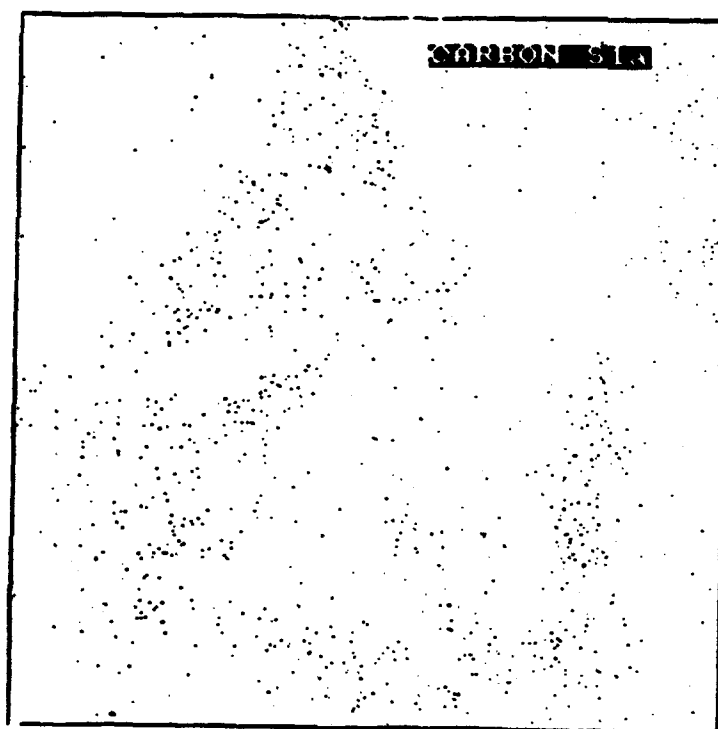
Figure 50.3. X-ray map of carbon.

84

Figure 50.4. X-ray map of aluminum.
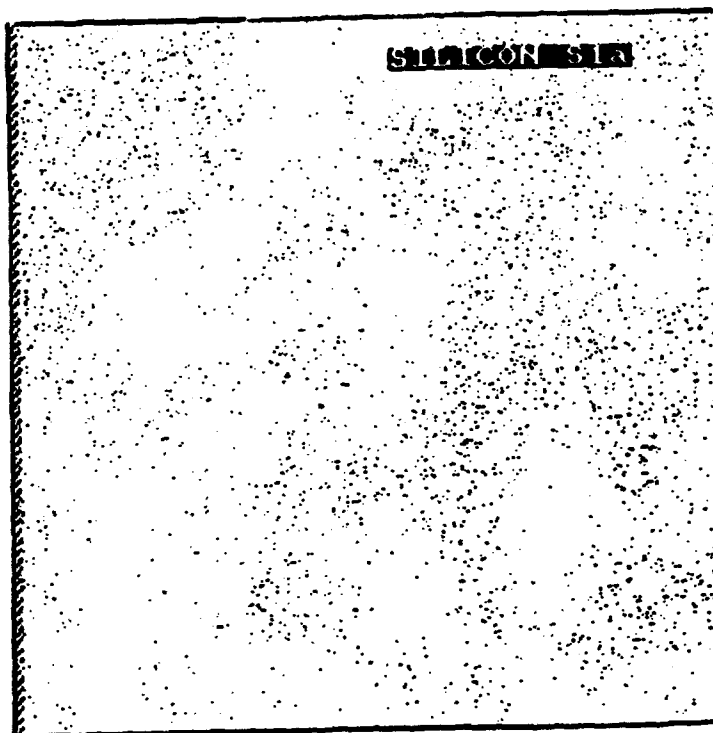
Figure 50.5. X-ray map of silicon.

Table 6. Elemental Composition of the Fusion Zone Matrix of Weld Ti:A.

Element	Amount Present (wt%)
Titanium	70.79
Aluminum	23.23
Silicon	2.29
Carbon	0.95

The data shown in Table 6 suggest that the matrix is primarily a titanium aluminide (mixture of TiAl and Ti_3Al) that contains small amounts of silicon and carbon. The titanium aluminide matrix suggests a brittle weld, due to the characteristic poor ductility of intermetallic compounds [74]. Nodules containing large platelike structures were evident near the edge of the fusion zone, as shown in Figure 51. EPMA of these platelike structures in the nodules suggest they are $TiAl_3$ ($TiAl_3$ stoichiometric composition: 62.8 wt% Al, 37.2 wt% Ti), while the surrounding matrix is an Al-Si alloy. Also near the edge of the fusion zone were band-like structures, (Figure 52). EPMA of these band structures suggest a complex compound containing appreciable amount of all four elements.

Weld Ti:B (127 μm Ti shim) also did not exhibit aluminum carbide platelets in the fusion zone, as evidenced in Figure 53. Neither the large nodular regions nor the bandlike structures found near the edge of the fusion zone of weld Ti:A were observed in this weld. Two regions of were observed in weld Ti:B. Shown in Figure 54 is a back scattered electron image of the first region, that contains four distinct areas. The elemental composition of the brighter matrix region appears to be $TiAl_3$ with some silicon present. The darker matrix area, containing a lower amount of titanium, is composed predominately of Al and $TiAl_3$ with some silicon and carbon present. The bright blocky region is nearly stoichiometric TiC, containing some aluminum and silicon. EPMA of the dendrites suggest that they are a combination of Ti_xAlC and TiC. The TiC is most predominate around the
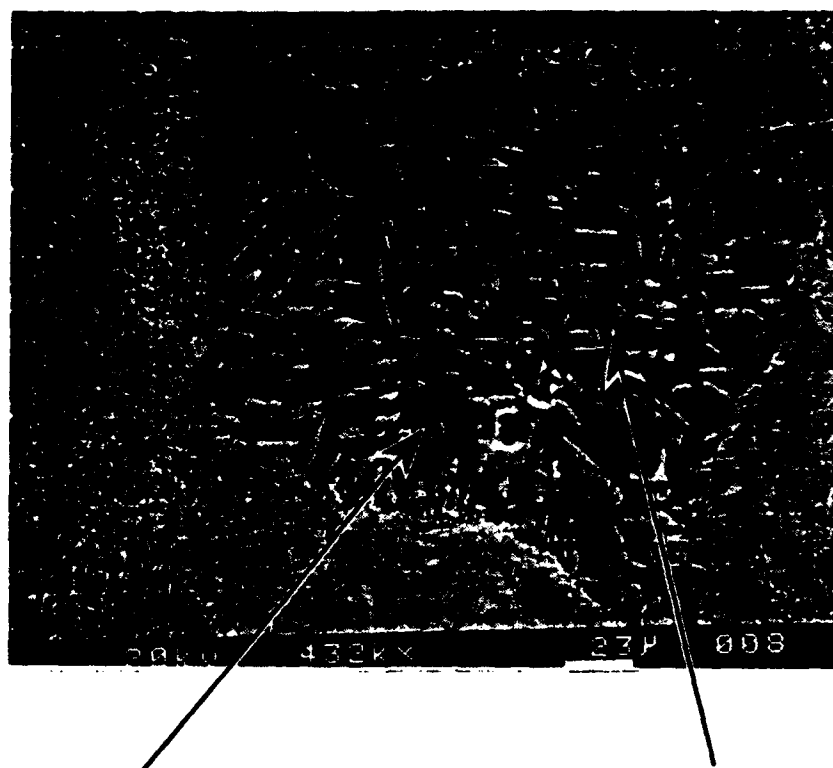
Matrix

Element	Amount Detected (wt%)
Aluminum	72.5
Silicon	16.5
Carbon	5.2
Titanium	0.2

Platelets

Element	Amount Detected (wt%)
Aluminum	52.4
Titanium	36.9
Silicon	6.7
Carbon	2.4

Figure 51. Intermetallic nodule formed at the edge of the fusion zone of the 6061/SiC/20w composite welded using a 0.582 mm thick titanium shim (Weld Ti:A).
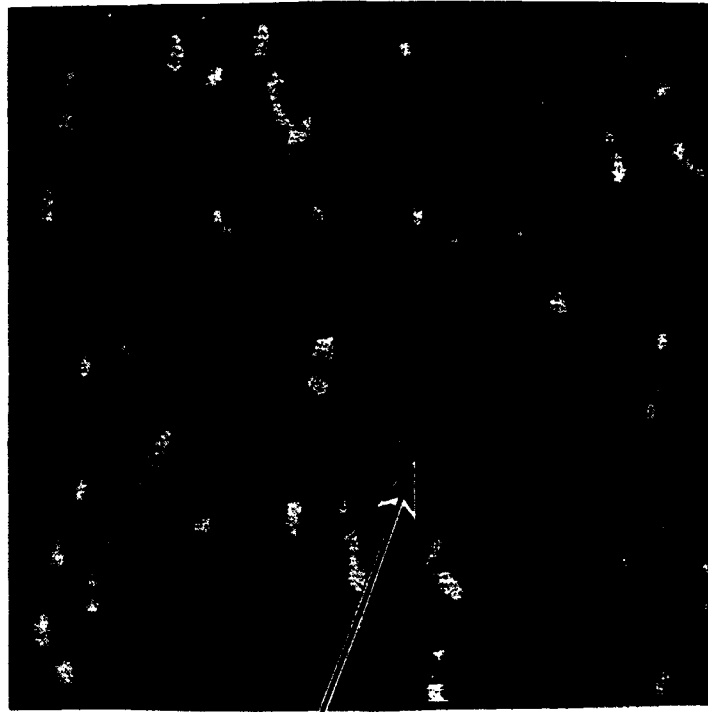
Banded Structure

Element	Amount Detected (wt%)
Titanium	63.3
Silicon	16.9
Aluminum	10.7
Carbon	9.0

Figure 52. Banded structure formed near the edge of the fusion zone of the 6061/SiC/20w composite welded using a 0.582 mm thick titanium shim (Weld Ti:A).
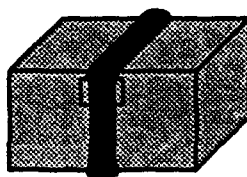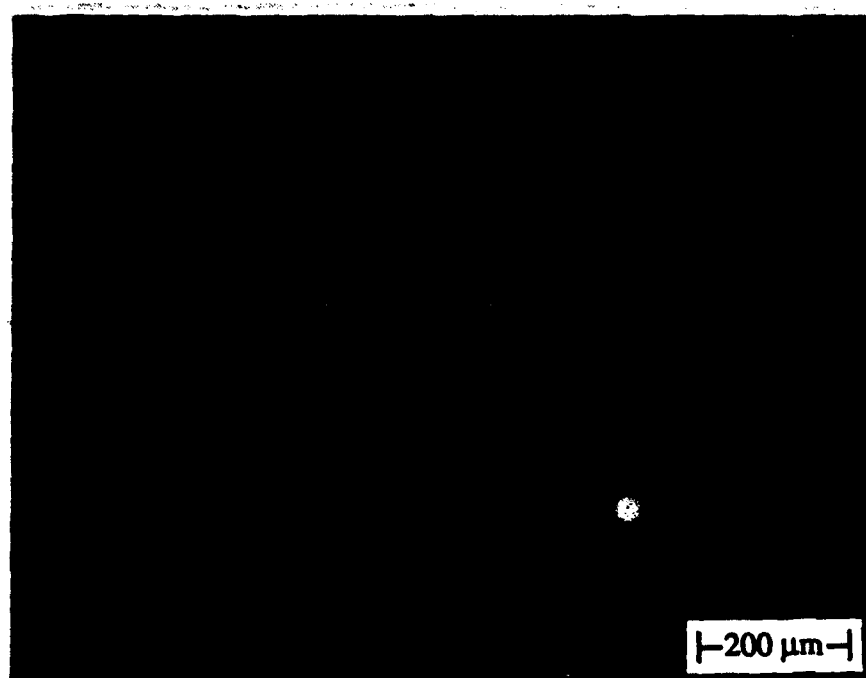
Figure 53. Optical micrograph of the fusion zone of the fusion zone of weld Ti:B (0.127 mm Ti shim: 6061/SiC/20w base material). No aluminum carbide platelets are evident.

Bright Blocky Phase

Element	Amount Detected (wt%)
Titanium	78.2
Carbon	17.9
Aluminum	2.6
Silicon	0.9

Dendrites

Element	Amount Detected (wt%)
Titanium	68.8
Carbon	18.4
Aluminum	10.2
Silicon	2.6
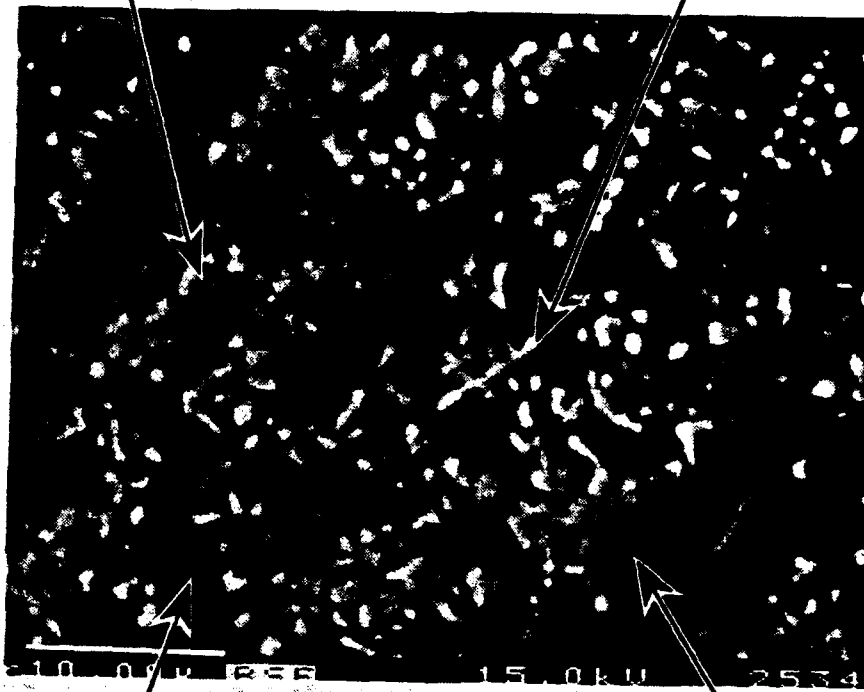
Dark Matrix Regions

Element	Amount Detected (wt%)
Aluminum	77.5
Titanium	15.1
Silicon	4.8
Carbon	2.2

Light Matrix Regions

Element	Amount Detected (wt%)
Aluminum	55.3
Titanium	37.8
Silicon	5.9
Carbon	1.1

Compound	Weight Percent		
	Al	C	Ti
TiC	-	20.0	80.0
TiAl$_2$	53.0	-	47.0
TiAl$_3$	62.8	-	37.2
Ti$_2$AlC	20.0	8.9	71.1
Ti$_3$AlC	14.8	6.6	78.6

Figure 54. Dendrites and blocky particles in a two phase matrix in the fusion zone of the 6061/SiC/20w composite welded using a 0.127 mm thick titanium shim (Weld Ti:B).

edge of the dendrites, which seems to indicate that TiC is forming from the Ti_xAlC

compounds. This agrees with the observations made by Jarfors, Fredricksson, and Froyen

[38]. The formation of titanium carbide at the surface of the dendrites may also explain the

composition of the darker matrix phase that is in contact with the dendrites and blocky

particles. If the Ti_xAlC compounds react to form TiC, the aluminum content of the

surrounding region should increase, as shown by the EPMA. The second region, shown

in Figure 55, contains dendrites within a matrix. The dendrites are composed of a

compound containing appreciable amounts of all four elements, while the matrix is nearly

stoichiometric $TiAl_2$ ($TiAl_2$ stoichiometric composition: 53.0 wt% Al, 47.0 wt% Ti).

The microstructure of Weld Ti:C (64 μm Ti shim) exhibits the formation of

aluminum carbide platelets in the fusion zone, as shown in Figure 56. A back scattered

electron (BSE) image of the fusion zone (Figure 57) shows the titanium is not uniformly

distributed throughout the fusion zone (brighter regions denote the presence of titanium).

Figure 58 is a BSE image of the region below the pore shown in Figure 57. Four regions

are evident, dark platelets, gray platelets, a gray blocky phase, and the matrix. The

morphology of the dark platelets corresponds to aluminum carbide platelets. EPMA shows

that these dark platelets are nearly stoichiometric aluminum carbide (Al_4C_3 stoichiometric

composition: 75.0 wt% Al, 25.0 wt% C). The gray platelets, having the same morphology

as the dark platelets, contain a significant amount of titanium. The gray blocky phase has a

composition very similar to that of the gray platelets. The matrix in this region is an

aluminum silicon alloy containing low levels of titanium and carbon. As the titanium

content increases (moving to the left in Figure 57) the dark platelets gradually disappear and

the gray platelets and blocky particles become more prevalent. At the left of the fusion zone

the microstructure consists primarily of the blocky particles. This indicates that as the

titanium levels increase aluminum carbide platelets become less stable and the blocky

particles become more stable.
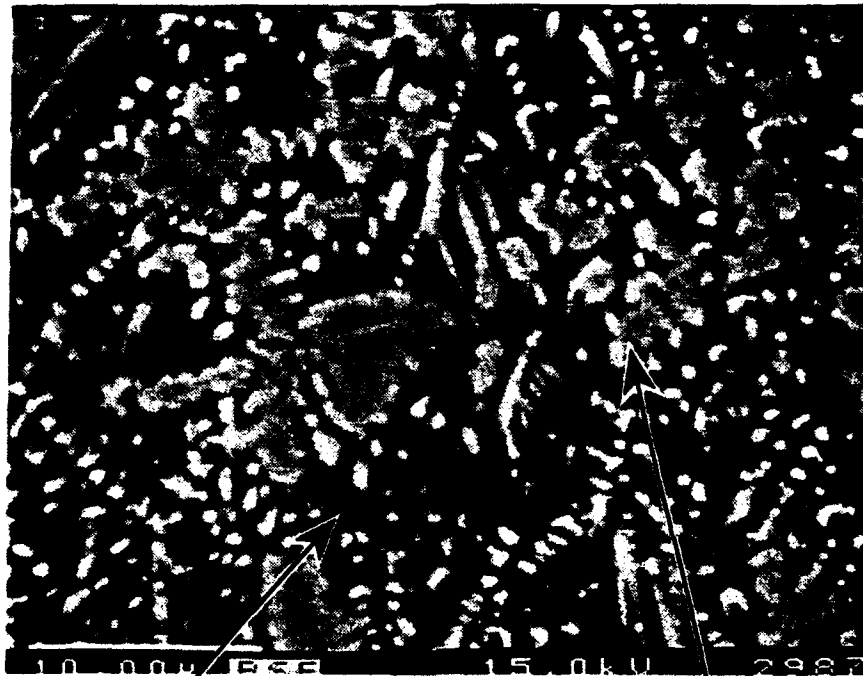
Matrix

Element	Amount Detected (wt%)
Titanium	51.1
Aluminum	46.2
Silicon	1.5
Carbon	1.2

Dendrites

Element	Amount Detected (wt%)
Titanium	73.2
Carbon	11.5
Aluminum	10.9
Silicon	4.4

Figure 55. Dendrites within the matrix in the fusion zone of the 6061/SiC/20w composite welded using a 0.127 mm thick titanium shim (Weld Ti:B).

├─200 μm─┤

├─ 80 μm ─┤
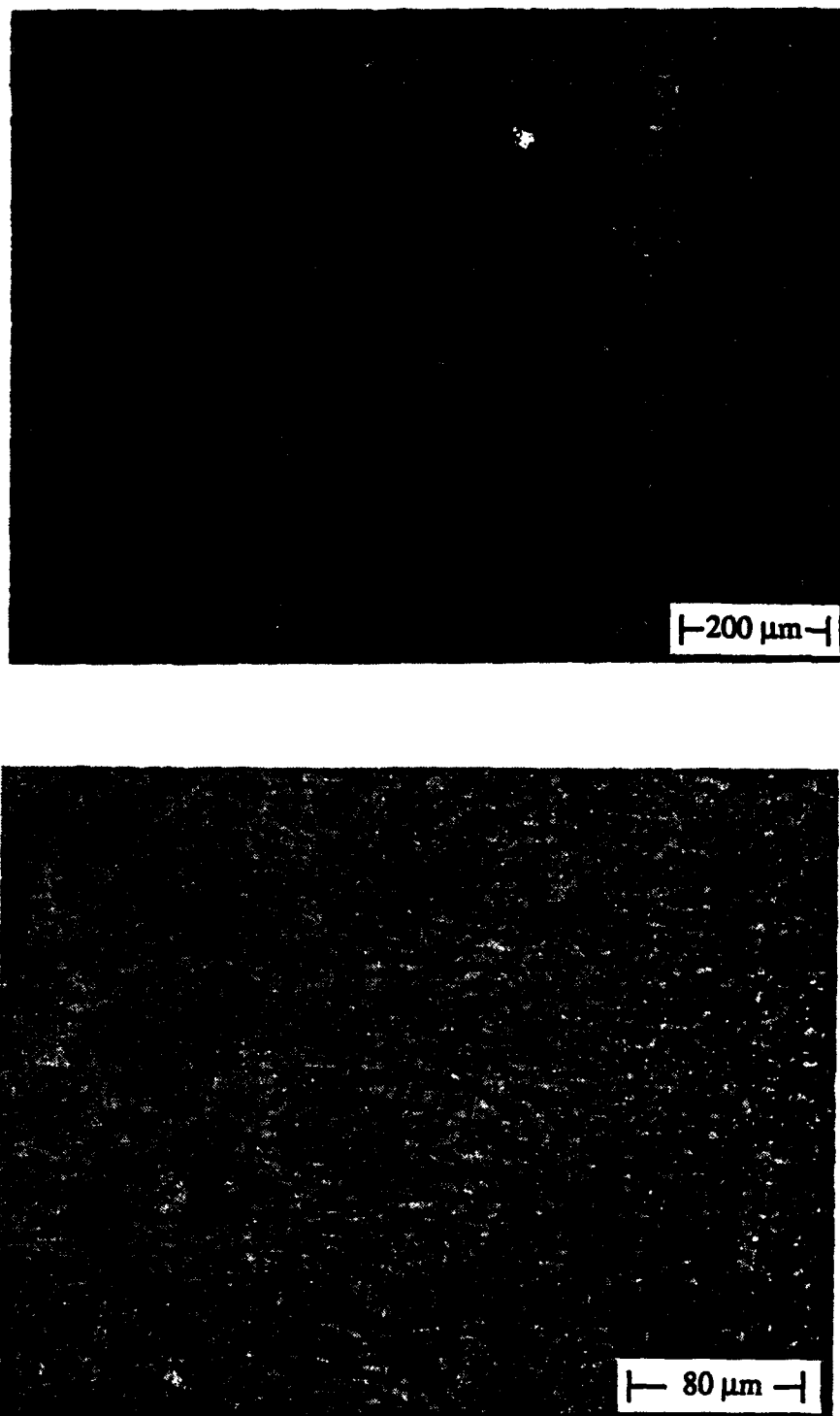
Figure 56. Optical micrograph of the fusion zone of the fusion zone of weld Ti:C (0.064 mm Ti shim: 6061/SiC/20w base material). Aluminum carbide platelets are evident near the edge of the fusion zone.
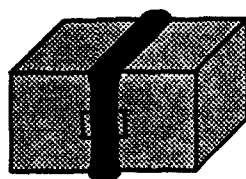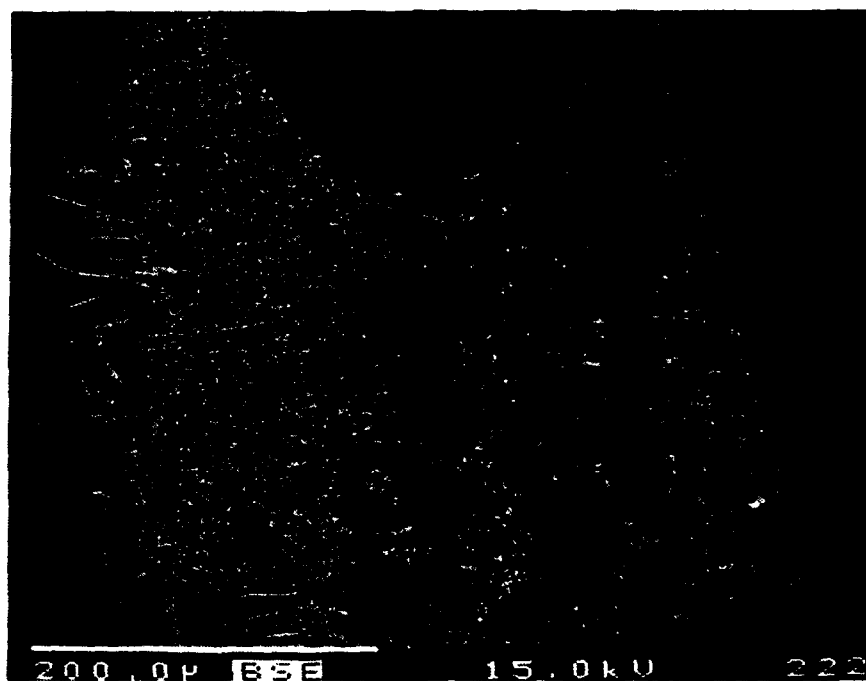
Figure 57. Back scattered electron image of the fusion zone of the 6061/SiC/20w composite welded using a 0.064 mm thick titanium shim (Weld Ti:C).

Matrix

Element	Amount Detected (wt%)
Aluminum	79.1
Silicon	16.8
Titanium	2.1
Carbon	0.1

Grey Blocky Phase

Element	Amount Detected (wt%)
Silicon	35.8
Titanium	31.4
Aluminum	29.8
Carbon	2.9
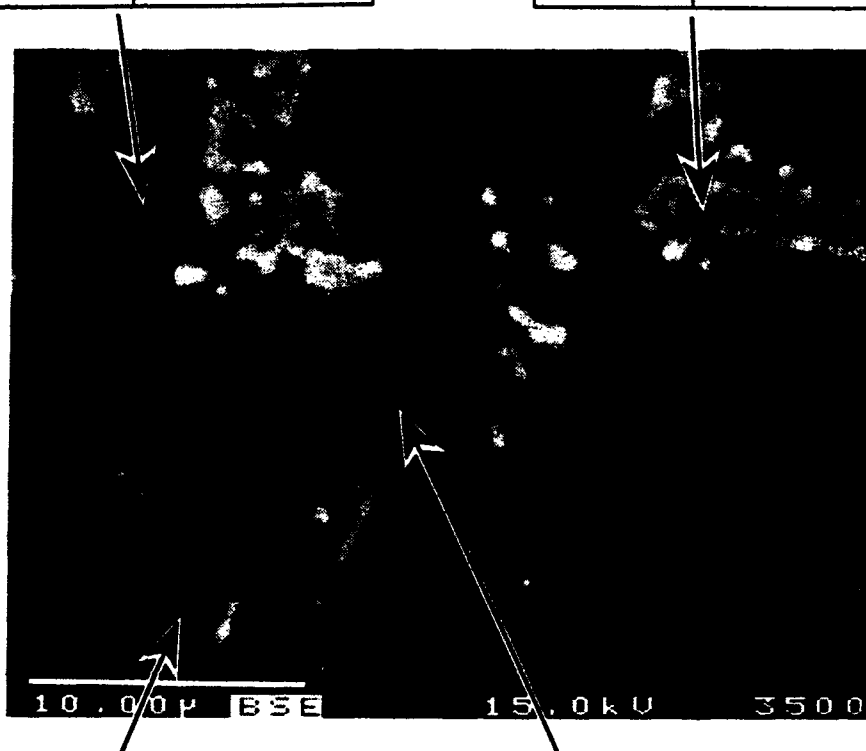
Gray Platelets

Element	Amount Detected (wt%)
Silicon	33.9
Aluminum	33.7
Titanium	29.2
Carbon	3.1

Dark Platelets

Element	Amount Detected (wt%)
Aluminum	66.6
Carbon	23.8
Silicon	9.1
Titanium	0.5

Figure 58. Back scattered electron image of structures present in the fusion zone of the 6061/SiC/20w composite welded using a 0.064 mm thick titanium shim (Weld Ti:C).

The welds made using zirconium filler additions showed results similar to those made using titanium filler additions. Weld Zr:A (18 vol% addition) resulted in a weld containing no discernible aluminum carbide platelets in the fusion zone, Figure 59. Weld Zr:B (11 vol% addition) contained aluminum carbide platelets near the edge of the fusion zone, Figure 60. From the microstructural observations it can be concluded that the optimal level of filler addition for zirconium necessary to prevent the formation of aluminum carbide lies between 18 and 11 vol%.
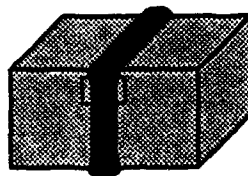
Figure 59. Optical micrograph of the fusion zone of weld Zr:A (0.127 mm Zr shim: 6061/SiC/20w base material). No aluminum carbide platelets are evident.
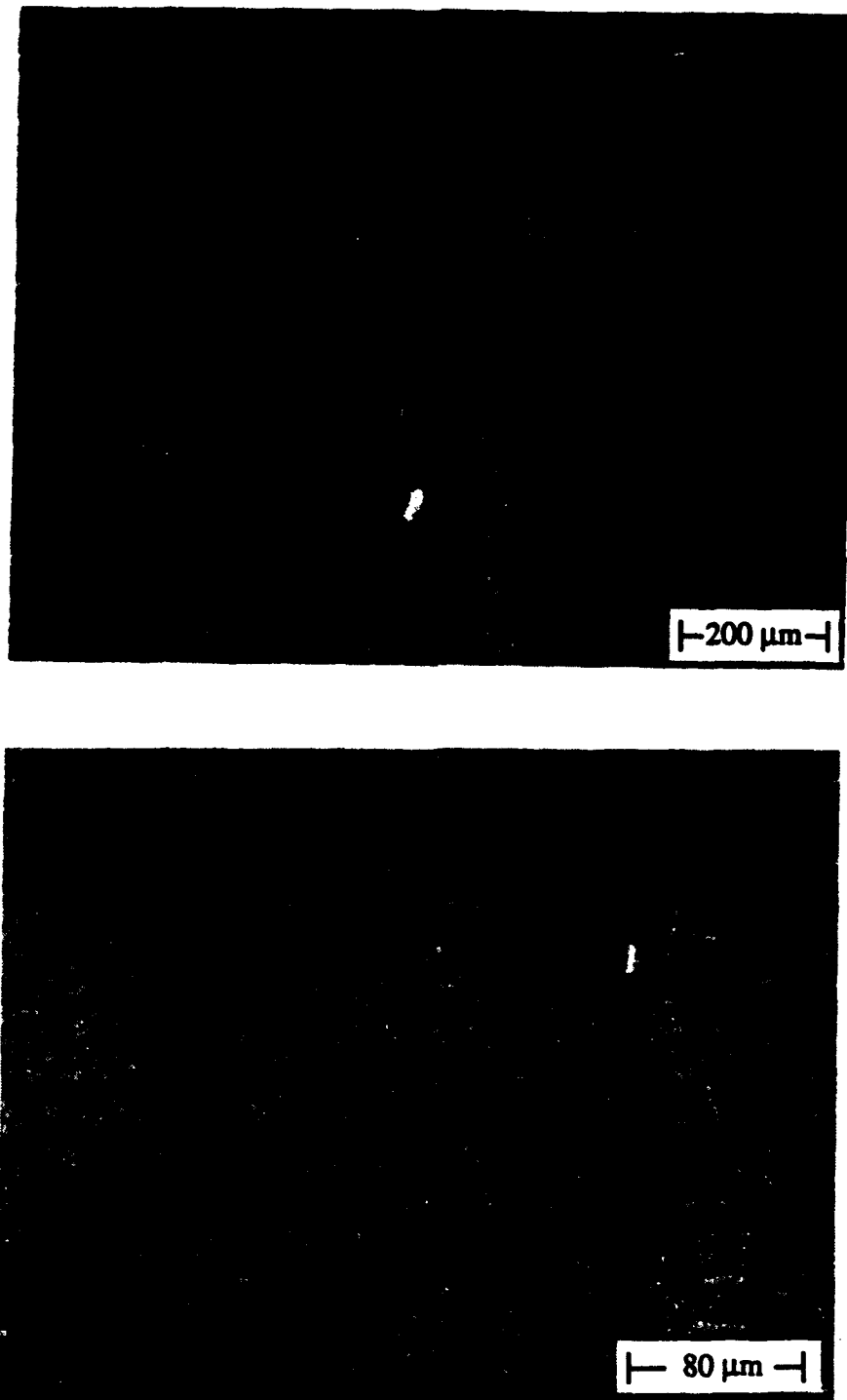
Figure 60. Optical micrograph of the fusion zone of the fusion zone of weld Zr:B (0.040 mm Zr shim: 6061/SiC/20w base material). Aluminum carbide platelets are evident in near the edge of the fusion zone.

Chapter 5

CONCLUSIONS

The results of the laser cutting experimentation suggest that lasers can be effective in cutting DRA composites. However, laser welding of these materials may pose difficulties due to the formation of undesirable phases in the fusion zone. Primarily, the formation of aluminum carbide from the silicon carbide reinforcement and molten aluminum may lead to extremely low ductility of the welded joint and accelerated corrosion in moist environments. It has been found that alloying additions to the fusion zone can suppress the formation of aluminum carbide. Higher processing speeds and greater penetration show that lasers offer a viable technique for processing these materials.

It was found that the DRA composites could be cut at rates faster than that of unreinforced aluminum. The improved cutting rates are attributed to the energy absorption of the reinforcement. The silicon carbide and aluminum oxide reinforcements absorb more laser energy than unreinforced aluminum. Calculations based on the rule of mixtures showed that a Al/SiC/20 composite absorbs 2.5 times more energy than unreinforced aluminum while an Al/Al$_2$O$_3$/20 composite absorbs more than 7.5 times the energy of unreinforced aluminum. A comparison of the effective emissivities and the experimental laser cutting rates show that there is a direct correlation between the two.

For the case of the 6061/SiC/20w composite, the increased cutting rates offered by the improved energy absorption were offset by the formation of aluminum carbide. The increased viscosity caused by the formation of aluminum carbide results in a large dross layer attached to the cut exit and a reaction layer on the cut surface, leading to a decreased cutting rate in comparison to unreinforced aluminum. The formation of aluminum carbide was not observed in the X2080/SiC/15p composite. It is believed that the silicon carbide

particles are expelled from the cut before the formation of aluminum carbide can affect the viscosity of the molten material. Therefore, laser cutting seems best suited for composites which do not have silicon carbide whisker reinforcement.

Microhardness testing for 2 mm thick sections of the 6061/Al$_2$O$_3$/20p composite determined that the loss of hardness was exhibited to a distance of 0.4 mm from the cut surface. Optical microscopy determined that this was probably due to coarsening of the Mg$_2$Si precipitates. Microhardness testing of a 1 mm thick section of the 6061/SiC/20w composite revealed that the formation of aluminum carbide leads to a substantial increase in the hardness adjacent to the cut surface. This increase in hardness extends less than 0.1 mm from the cut surface. The relative sizes of the heat affected zones are in agreement with the reported thermal conductivities of the composites. The addition of aluminum oxide decreases thermal conductivity, while the addition of silicon carbide increases thermal conductivity.

Welds made on the composites showed that the improved absorption of laser energy also resulted in a substantial increase in the weld penetration depth over unreinforced aluminum. Effective emissivities calculated by the rule of mixtures correlated well with the weld penetration depth.

Comparison of gas tungsten arc welding and laser beam welding of Al/SiC composites showed that laser welding results in much deeper penetration into the workpiece. The welds made on the 6061/SiC/20w composite exhibited aluminum carbide platelets, a large weld crown, and a substantial amount of porosity in the weld. The porosity observed in the welds is believed due to hydrogen entrapped in the material during P/M fabrication and evolves during welding. For the A356/SiC/20p composite, aluminum carbide was observed in the laser beam weld, but not in the GTA weld. The high silicon content of the matrix alloy combined with the lower weld pool temperatures of GTA welding prevented aluminum carbide formation. The microstructure of the A356/SiC/20p

laser weld was rather complex, consisting of a region containing resolidified composite, a region with a partial reaction between silicon carbide and aluminum, and a region in the center of the weld where all the silicon carbide reacted to form aluminum carbide.

It has been shown previously that titanium and zirconium can eliminate the formation of aluminum carbide by the formation of their respective carbides. Analysis of the properties of TiC and ZrC show that they are more chemically stable than aluminum carbide and are not subject to dissolution in water. Furthermore, the formation of titanium and zirconium carbides from silicon carbide result in volumetric expansions of five and three percent respectively; significantly less than the twenty-five percent due to the formation of aluminum carbide.

A thermodynamic analysis of additions of titanium to a Al/SiC/20 composite was conducted using the SOLGASMIX chemical equilibrium computer program. The analysis predicted that 22 wt% (15 vol%) addition of titanium to the fusion zone is necessary to prevent the formation of aluminum carbide for composite reinforced with 20 vol% silicon carbide. Titanium additions less than 22 wt% will result in the formation of aluminum carbide. However, if excess titanium is present, the formation of a titanium silicon intermetallic (TiSi) is predicted.

The welds on the 6061/SiC/20w composite made using titanium filler additions have shown that the formation of aluminum carbide can be suppressed. Three welds representing three different levels of titanium additions were analyzed. Weld Ti:A (~53 vol% addition of Ti) exhibited no aluminum carbide platelets. Fine titanium carbide dendrites (1-5 μm in size) were identified using x-ray mapping. Although titanium carbides were found, the high titanium content resulted in titanium aluminide and titanium silicide intermetallic structures in the fusion zone as well as a titanium aluminide matrix. The presence of these intermetallic compounds is expected to lead to a brittle weld due to their characteristic poor ductility. Weld Ti:B (≈ 18 vol% addition of Ti) did not exhibit

aluminum carbide platelets or the titanium aluminum and titanium-silicon intermetallic structures observed in Weld Ti:A. The microstructure of the fusion zone consisted of dendrites and blocky particle in a matrix of titanium and aluminum. The dendrites were found to be a mixture of Ti_xAlC and TiC as determined by EPMA. while the blocky particles were primarily TiC. Weld Ti:C (≈ 11 vol% addition of Ti) did exhibit the aluminum carbide platelets in the fusion zone, as expected from the thermodynamic analysis. EPMA of the weld determined that the aluminum carbide formed becomes less stable as the titanium levels increase.

Weld made using zirconium filler additions showed similar results to those made using titanium filler additions. In Weld Zr:A (≈ 18 vol% addition of Zr) no aluminum carbide was observed. Aluminum carbide platelets were observed however, in Weld Zr:B (≈ 11 vol% addition of Zr). From the experimental observations of the welds made using zirconium filler additions it can be concluded that the optimal level of addition to the fusion zone lies between 11 and 18 vol%.

Chapter 6

RECOMMENDATIONS FOR FUTURE WORK

The amount of laser energy absorbed by the composite has been shown to be very important factor for laser processing of DRA composites. Although the comparisons made using the calculated emissivities provided reasonable results, the calculations involved several assumptions. Determination of the actual emissivities of the composite materials may provide data for predicting the effectiveness of laser processing.

The DRA composites used for the laser cutting experimentation represented only a small sample of different materials. Furthermore, the limited amount of material available prevented full characterization of laser cutting of these materials. A more detailed analysis employing more materials may be warranted.

The experimentation for eliminating the formation of aluminum carbide by filler metal additions of titanium and zirconium were successful; however more study is required. The thermodynamic analysis made using the SOLGASMIX computer program provided an accurate prediction for the optimal level of filler addition. However, further development of the activity and free energy data may provide a better correlation between the prediction and the experimental results. Several compounds were observed in the welds that were not accounted for the in the analysis, and the zirconium additions could not be analyzed because of the lack of activity data. In addition to the thermodynamic analysis, an investigation of the kinetics of the reactions in occurring in the fusion zone may aid in determining the optimal amounts of titanium and zirconium additions. The addition of filler metals by thin shims was an effective way of providing measured amounts of metals into the fusion zone, but the method was difficult to implement. The method may also have resulted in the segregation observed in some of the welds. Development of alternative

methods for addition of the filler metals should be investigated. Finally, characterization of the produced welds is necessary to determine the viability of the process.

REFERENCES

1) J.E. Allison and G.S. Cole, "Metal Matrix Composites in the Automotive Industry", *JOM*, 45 (1) (1993), pp. 19-24.

2) W.H. Hunt, Jr., C.R. Cook, and R.R. Sawtell, "Cost Effective High Performance P/M Aluminum Matrix Composites for Automotive Applications", SAE Paper 910834 (Warrendale, PA: SAE, 1991).

3) F.E. Wawner, "Metal Matrix Composites, Discontinuously Reinforced, Microstructure and Property Correlations", *International Encyclopedia of Composites, Vol. 3*, ed. Stuart M. Lee, (New York: VCH, 1990), pp. 246-259.

4) M.G. McKimpson and T.E. Scott, "Processing and Properties of Metal Matrix Composites Containirg Discontinuous Reinforcement", *Materials Science and Engineering A*, (107) (1989), pp. 93-106.

5) Warren H. Hunt, Jr., "Cost Effective High Performance P/M Aluminum Matrix Composites for Aerospace Applications", presented at: International Conference of P/M Aerospace Materials 1991, November 4-6, 1991, Lausanne, Switzerland.

6) T.M. Osman, J.J. Lewandowski, and W.H. Hunt, Jr., "Microstructure-property Relationships For an Al/SiCp Composite With Different Deformation Histories", *Fabrication of Particulates Reinforced Metal Composites*, (Materials Park, Ohio: ASM, 1990), pp. 209-216.

7) P.W. Jeffrey and S. Holcomb, "Extrusion of Particulate-Reinforced Aluminum Matrix Composites", *Fabrication of Particulates Reinforced Metal Composites*, (Materials Park, Ohio: ASM, 1990), pp. 181-186.

8) T.G. Nieh and J. Wadsworth, "Superplasticity and Superplastic Forming of Aluminum Metal-Matrix Composites", *JOM*, 44 (11) (1992), pp. 46-50.

9) A.P. Divecha, S.G. Fishman, and S.D. Karmarkar, "Silicon Carbide Reinforced Aluminum -- A Formable Composite", *Journal of Metals*, (9) (1981), pp. 12-17.

10) A.L. Geiger and J.A. Walker, "The Processing and Properties of Discontinuously Reinforced Aluminum Composites", *JOM*, 43 (8) (1991), pp. 8-15.

11) Duralcan Composites: Machining Guidelines, Duralcan USA, 1991.

12) J.G. Sylvia, "Abrasive Waterjet Cutting", *ASM Metals Handbook, 9th Edition, Volume 16: Machining*, (Materials Park, Ohio: ASM, 1989), pp. 743-755.

13) R.P. Martukanitz and R.B. Bhagat, "Laser Processing of Discontinuously Reinforced Aluminum Matrix Composites", *The Metal Science of Joining*, eds. M.J. Cieslak, J.H. Prerpezko, S. Kang, and M.E. Glicksman, (Warrendale, PA: TMS, 1992), pp. 241-248.

14) Duralcan Composites: Arc Welding Guidelines, Duralcan USA, 1991.

15) M.K. Surappa and P.K. Rohatgi, "Fluidity of Aluminum-Silicon-Alumina Composite", *Metallurgical Transactions B*, 12 (6) (1981), pp. 327-332.

16) K.B. Das, "Joining of Metal Matrix Composites", *International Encyclopedia of Composites, Vol. 2*, ed. Stuart M. Lee, (New York, NY: VCH, 1990), pp. 460-509.

17) R. P. Martukanitz and P.R. Michnuk, "Sources of Porosity in Gas Metal Arc Welding of Aluminum", *Trends in Welding Research in the United States*, ed. S.A. David, (Materials Park, OH: ASM, 1982), pp. 315-330.

18) H.J. Rack and P. Ratnaparki, "Powder Metal Composites", *International Encyclopedia of Composites, Vol. 4*, ed. Stuart M. Lee, (New York, NY: VCH, 1990), pp. 378-402.

19) R.P. Martukanitz, Applied Research Laboratory - Penn State, Personal Communication

20) *Aluminum: Properties and Physical Metallurgy*, ed. J.E. Hatch, (Materials Park, OH: ASM, 1984), pp. 18-19, 222-223.

21) R.B. Bhagat, "Casting Fiber Reinforced Metal Matrix Composites", *Metal Matrix Composites: Processing and Interfaces*, eds. R.K. Everett and R.J. Arsenault, (New York, NY: Academic Press, 1991), pp. 43-82.

22) B. Altshuller, W. Christy, and B. Wiskel, "GMA Welding of Al-Al$_2$O$_3$ Metal Matrix Composite", *Weldability of Materials*, eds. R.A. Patterson and K.W. Mahin, (Materials Park, OH: ASM, 1990), pp. 305-309.

23) B. Irving, "What's Being Done to Weld Metal-Matrix Composites", *Welding Journal*, 70 (6) (1991), pp. 65-67.

24) C.D. Lundin, J.C. Danko, and C.J. Swindeman, "Fusion Welding of SiC-Reinforced Aluminum Alloy 2024", *Recent Trends in Welding Science and Technology, TWR '89*, eds. S.A. David and J.M. Vitek, (Materials Park, OH: ASM, 1990), pp. 303-307.

25) M.J. Cola, T.J. Leinert, J.E. Gould, and J.P. Hurley, "Laser Welding of a SiC Particulate Reinforced Aluminum Metal Matrix Composite", *Weldability of Materials*, eds. R.A. Patterson and K.W. Mahin, (Materials Park, OH: ASM, 1990), pp. 297-303.

26) N.B. Dahotre, T.D. McCay, and M.H. McCay, "Laser Processing of a SiC/Al-Alloy Metal Matrix Composite", *Journal of Applied Physics*, 65 (12) (1989), pp. 5072-5077.

27) N.B. Dahotre, M.H. McCay, T.D. McCay, and L.F. Allard, "Pulse Laser Processing of a SiC/Al-Alloy Metal Matrix Composite", *Journal of Materials Research*, 6 (3) (1991), pp. 514-529.

28) M.H. McCay, T.D. McCay, N.B. Dahotre, and C.M. Sharp, " Fusion Zone Structure in Laser Welded Al-SiC Composites", *Journal of Laser Applications*, 3 (3) (1991), pp. 35-39.

29) J.H. Develetian, "SiC/Al Metal Matrix Composite Welding by a Capacitor Discharge Process", *Welding Journal*, 66 (6) (1987), pp. 33-39.

30) K.M. Jasim, R.D. Rawlings, R. Sweeney, and D.R.F. West, "Microstructural Changes Associated with the Laser Processing of Al-SiC Composites", *Journal of Materials Science Letters*, 11 (7) (1992), pp. 414-417.

31) D.J. Lloyd, " The Solidification Microstructure of Particulate Reinforced Aluminum/SiC Composites", *Composites Science and Technology*, 35 (1989), pp. 159-179.

32) T.Y. Kosolapova, *Carbides: Properties, Production, and Applications*, (New York, NY: Plenum Press, 1971).

33) A.S. Isaikin, V.M. Chubarov, B.F. Trefilov, V.A. Silaev, and Y.A. Gorelov, , "Compatiblity of Carbon Filaments with a Carbide Coating and an Aluminum Matrix", *Metal Science and Heat Treatment*, 22 (11-12) (1980), pp. 815-817.

34) T. Iseki, T. Kameda, and T. Maruyama, "Interfacial Reactions Between SiC and Aluminum During Joining", *Journal of Material Science*, 19 (1984), pp. 1692-1698.

35) D.M. Schuster, M.D. Skibo, and W.R. Hoover, "Production and Semi-Fabrication of an Aluminum Composite Material: Extrusion and Casting Considerations", *Light Metal Age*, 47 (1/2) (1989), pp. 15-19.

36) A. Banerji and W. Reif, "Development of Al-Ti-C Grain Reinfiners Containing TiC", *Metallurgical Transactions A*, 17 (12) (1986), pp. 2127-2137.

37) M.E. Fine and J.G. Conley, "Discussion of 'On the Free Energy of Formation of TiC and Al_4C_3'", *Metallurgical Transactions A*, 21 (9) (1990), pp. 2609-2610.

38) A. Jarfors, H. Fredriksson, and L. Froyen," On the Thermodynamics and Kinetics of Carbides in the Aluminum-Rich Corner of the Al-Ti-C Phase Diagram", *Materials Science and Engineering A*, 135 (1991), pp. 119-123.

39) A. Jarfors and H. Fredriksson," On the Behavior of TiC Particles in the Al-Rich Corner of the Al-Ti-C Phase Diagram", *Microgravity Science and Technology*, III/4, (1991), pp. 216-221.

40) R.A. Rapp and X. Zheng, "Thermodynamic Consideration of Grain Refinement of Aluminum Alloys by Titanium and Carbon", *Metallurgical Transactions A*, 22 (12) (1991), pp. 3071-3075.

41) H. Yokokawa, N. Sakai, T. Kawada, M. Dokiya, "Chemical Potential Diagram of Al-Ti-C System: Al_4C_3 Formation on TiC Formed in Al-Ti Liquids Containing Carbon", *Metallurgical Transactions A*, 22 (12) (1991), pp. 3075-3076.

42) P. Sahoo and M.J. Koczak, "Analysis of In Situ Formation of Titanium Carbide in Aluiminum Alloys", *Materials Science and Engineering A*, 144 (1991), pp. 37-44.

43) G.H. Reynolds and L. Yang, "Plasma Joining of Metal Matrix Composites", Final Report: U.S. Army Research Office Contract DAAG29-85-C-0027, (San Marcos, CA: MSNW, Inc., 1988).

44) J.T. Luxon, and D.E. Parker, *Industrial Lasers and Their Applications*, (Englewood Cliffs, NJ: Prentice Hall, 1992).

45) D.C. Winburn, *What Every Engineer Should Know About Lasers*, (New York, NY: Marcel Dekker, 1987).

46) *Industrial Laser Handbook*, ed. D. Belforte, (New York, NY: Springer-Verlag, 1992).

47) J. Mazumder, "Laser Welding: State of the Art Review", *Journal of Metals*, (7) (1982), pp. 16-24.

48) "Laser Beam Welding", *Metals Handbook 9th Edition: Volume 6: Welding, Brazing, and Soldering*, (Materials Park, OH: ASM, 1983), pp. 647-671.

49) G.P. Simpson and T.J. Culkin, "Laser Cutting", *Metals Handbook, 9th Edition, Volume 16: Machining*, (Materials Park, OH: ASM, 1989), pp. 735-742.

50) W.W. Duley, *Laser Processing and Analysis of Materials*, (New York, NY: Plenum Press, 1983), p. 71.

51) S.M. Kawli, G.L. Viegelahn, and R. Scheuerman, "Laser Welding of Alumina Reinforced 6061 Aluminum Alloy Composite", *ICALEO'91: Proceedings of the Laser Materials Processing Symposium*, (Orlando, FL: Laser Institute of America, 1992), pp. 156-167.

52) Unpublished research, R.P. Martukanitz and D.J. Smith

53) C.A. Huntington and T.W. Eagar, "Laser Welding of Aluminum and Aluminum Alloys", *Welding Journal*, 62 (4) (1983), pp. 105-107.

54) K.R. Karasek, S.A. Bradley, J.T. Donner, J.L. Schienle and H.C. Yeh. "SiC Whisker Characterization: An Update", *Ceramic Bulletin*, 70 (2) (1991), pp. 224-228.

55) INNOMETAL™ X2080/SiC Composites for Stiffness Critical Applications, Aluminum Company of America.

56) A. J. Moses, *Optical Properties of Materials: Handbook of Electronic Materials, Vol. 1*, (New York, NY: Plenum Press, 1971), pp. 4-5, 72-73.

57) S.D. Dumolt, Ph.D. dissertation, Carnegie-Mellon University, Pittsburgh, PA, 1983.

58) Duralcan Composites for Wrought Products: Mechanical and Physical Property Data, Duralcan USA, 1991.

59) M.W. Chase, et. al, *JANAF Thermochemical Tables*, (Washington, D.C.: National Bureau of Standards, 1986).

60) *Engineering Property Data on Selected Ceramics, Vol. 2, Carbides*, (Columbus, OH: Metals and Ceramic Information Center; Battelle, Columbus Laboratories, 1979).

61) L.S. Darken, R.W. Gurry, *Physical Metallurgy of Metals*, (McGraw-Hill, New York, 1953).

62) M. Hoch and R.J. Usell, Jr.," Thermodynamics of Titanium Alloys: II. Titanium and Aluminum Activities in the BCC β Phase of the Ti-Al System", *Metallurgical Transactions*, 2 (9) (1971), pp. 2627-2632.

63) J.A. Peters, "Development of a Database of Thermochemical Properties for Use With the SOLGASMIX Computer Program", M.S. Thesis, The Pennsylvania State University, (1988).

64) L.L. Oden and R.A.McCune," Phase Equilbria in the Al-Si-C System", *Metallurgical Transactions A*, 18 (12) (1987), pp. 2005-2014.

65) J.L. Murray and A.J. McAlister, "The Al-Si (Aluminum-Silicon) System", *Bulletin of Alloy Phase Diagrams*, 5 (1) (1984), pp. 74-84.

66) *ASM Handbook: Volume 3 Alloy Phase Diagrams*, (Materials Park, OH: ASM, 1992), p. 113.

67) "The C-Ti (Carbon-Titanium) System", Phase Diagrams of Binary Titanium Alloys, ed. J.L. Murray, (Materials Park, OH: ASM, 1987), pp. 47-51.

68) J.L. Murray, "The Si-Ti (Silicon-Titanium) System", Phase Diagrams of Binary Titanium Alloys, ed. J.L. Murray, (Materials Park, OH: ASM, 1987), pp. 289-294.

69) U.R. Kattner, J.C. Lin, and Y.A. Chang, "Thermodynamic Assesment and Calculation of the Ti-Al System", *Metallurgical Transactions A*, 23 (8) (1992), pp. 2081-2090.

70) H.L. Lukas, "Al-Si-C System", Ternary Alloys: Volume 3, ed. G. Petzow and G. Effenberg, (New York, NY: VCH, 1990), pp. 540-548.

71) F.H. Hayes, "Al-C-Ti System", Ternary Alloys: Volume 3, ed. G. Petzow and G. Effenberg, (New York, NY: VCH, 1990), pp. 557-566.

72) J.L. Murray, "The Al-Ti (Aluminum-Titanium) System", Phase Diagrams of Binary Titanium Alloys, ed. J.L. Murray, (Materials Park, OH: ASM, 1987), pp. 12-24.

73) J. Chen, Z. Geng, and B.A. Chin, "The Tensile Properties and Microstructure of Ti-TiC Composites with Al Additions", *High Temperature Ordered Intermetallic Alloys III*, eds. C.T. Liu, et al., (Pittsburgh, PA: Materials Research Society,), pp. 447-453.

74) C.T. Liu, J.O. Stiegler, and F.H. Froes, "Ordered Intermetallics", *ASM Metals Handbook, 10th Edition, Volume 2: Properties and Selection: Nonferrous Alloys and Special-Purpose Materials*, (Materials Park, Ohio: ASM, 1989), pp. 913-942.

Volumetric Change Due To Chemical Reactions

$$4Al + 3SiC \rightarrow Al_4C_3 + 3Si \quad (1$$
$$Ti + SiC \rightarrow TiC + Si \quad (2$$
$$Zr + SiC \rightarrow ZrC + Si \quad (3$$
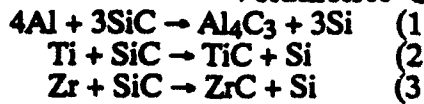
For Reaction 1

$$4Al \frac{26.98 \text{ g}}{\text{mole}} \frac{cm^3}{2.70 \text{ g}} = 39.97 \text{ cm}^3$$
$$3SiC \frac{40.10 \text{ g}}{\text{mole}} \frac{cm^3}{3.21 \text{ g}} = 37.48 \text{ cm}^3$$
$$\left. \right\} = 77.45 \text{ cm}^3$$

$$Al_4C_3 \frac{143.95 \text{ g}}{\text{mole}} \frac{cm^3}{2.36 \text{ g}} = 61.00 \text{ cm}^3$$
$$3Si \frac{28.09 \text{ g}}{\text{mole}} \frac{cm^3}{2.33 \text{ g}} = 36.17 \text{ cm}^3$$
$$\left. \right\} = 97.17 \text{ cm}^3$$

For Reaction 2

$$Ti \frac{47.90 \text{ g}}{\text{mole}} \frac{cm^3}{4.51 \text{ g}} = 10.62 \text{ cm}^3$$
$$SiC \frac{40.10 \text{ g}}{\text{mole}} \frac{cm^3}{3.21 \text{ g}} = 12.49 \text{ cm}^3$$
$$\left. \right\} = 23.11 \text{ cm}^3$$

$$TiC \frac{59.91 \text{ g}}{\text{mole}} \frac{cm^3}{4.94 \text{ g}} = 12.13 \text{ cm}^3$$
$$Si \frac{28.09 \text{ g}}{\text{mole}} \frac{cm^3}{2.33 \text{ g}} = 12.06 \text{ cm}^3$$
$$\left. \right\} = 24.19 \text{ cm}^3$$

For Reaction 3

$$Zr \frac{91.22 \text{ g}}{\text{mole}} \frac{cm^3}{6.49 \text{ g}} = 14.06 \text{ cm}^3$$
$$SiC \frac{40.10 \text{ g}}{\text{mole}} \frac{cm^3}{3.21 \text{ g}} = 12.49 \text{ cm}^3$$
$$\left. \right\} = 26.55 \text{ cm}^3$$

$$ZrC \frac{103.23 \text{ g}}{\text{mole}} \frac{cm^3}{6.73 \text{ g}} = 15.34 \text{ cm}^3$$
$$Si \frac{28.09 \text{ g}}{\text{mole}} \frac{cm^3}{2.33 \text{ g}} = 12.06 \text{ cm}^3$$
$$\left. \right\} = 27.40 \text{ cm}^3$$

Reaction	Volume of Reactants (cm^3)	Volume of Products (cm^3)	Percentage Change Over Inital Volume
1	77.45	97.17	+25.46
2	23.11	24.19	+4.67
3	26.55	27.40	+3.20

APPENDIX B

Activity Data for the SOLGASMIX Analyses

From Hoch and Usell [62], the activity of titanium as a function of mole fraction titanium and temperature is as follows.

$$a_{Ti} = X_{Ti}\exp\left(-11272.14\frac{1}{T} + 2.9547)(1 - X_{Ti})^2\right)$$

The activity of silicon and aluminum as a function of silicon content in an aluminum silicon alloy is shown in Table 1 [65].

Table 1. Activity of Silicon and Aluminum as a Function of Silicon Content [65].

Si Content	Activity	
	Al	Si
100.0	0.000	0.000
65.0	0.232	0.597
60.0	0.219	0.513
50.0	0.414	0.356
39.9	0.506	0.196
30.3	0.595	0.104
20.0	0.759	0.078
9.9	0.893	0.033
0.0	1.000	0.000

Using the quasi-chemical solution model and the activity data for silicon and aluminum, the following equation was generated for aluminum activity.

$$a_{Al} = X_{Al}\exp(-1.429(1 - X_{Ti})^2$$

The activity of silicon as a function of mole fraction of silicon.

$$a_{Si} = X_{Si}\exp(-1.320(1 - X_{Ti})^2$$

A graph of the equations developed from the quasi-chemical solution model are compared to the experimental data in Figure 1.
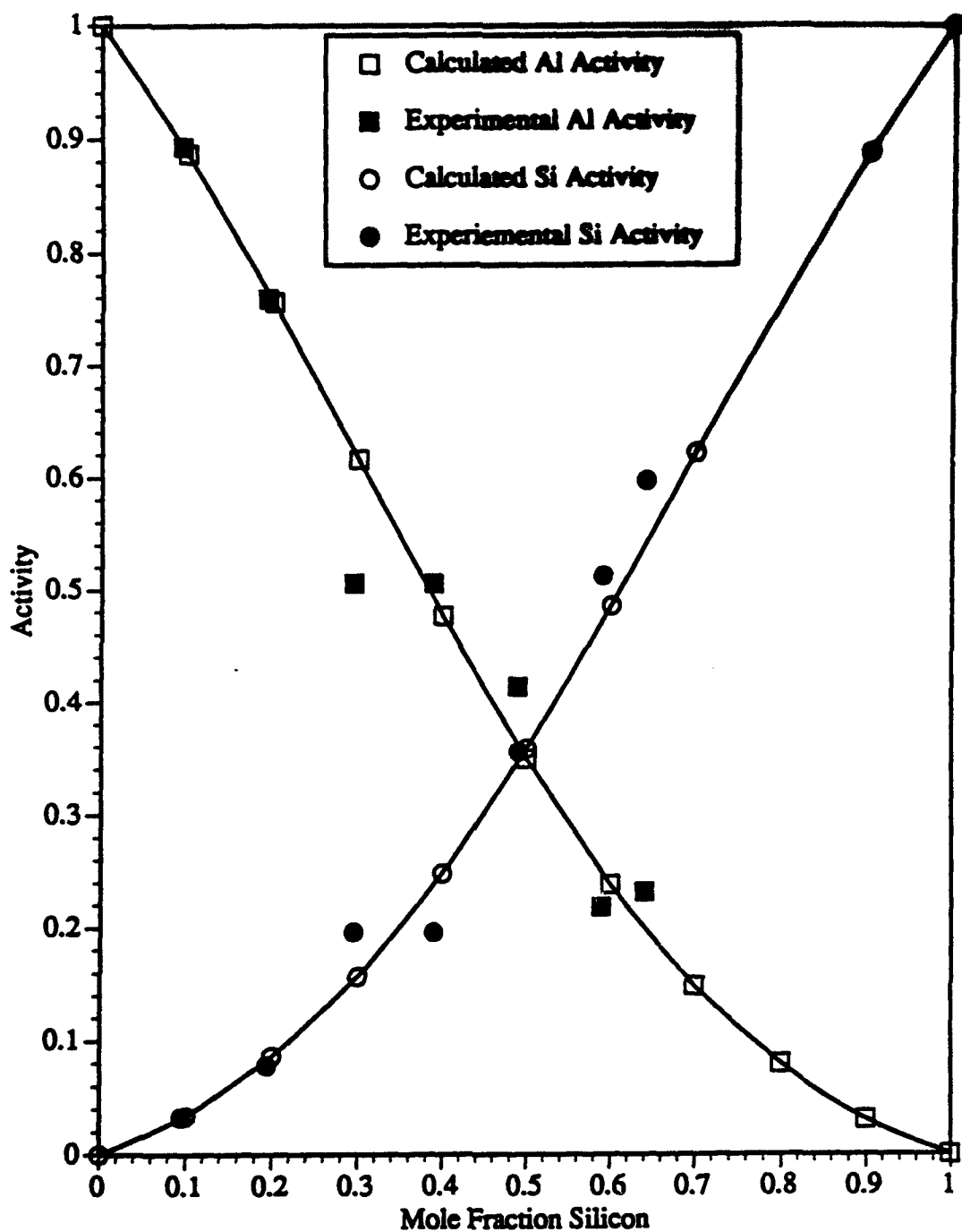
Figure 1. Comparison of the calculated activity values to the experimental values used in the calculations

APPENDIX C

Weight Fractions of Elements for the Compounds in the Al-C-Si-Ti System

Compound	Moles				Mass	Weight Fraction			
	Ti	Al	Si	C	(g/mol)	Ti	Al	Si	C
Al_4C_3	0	4	0	3	143.95	0.00	74.97	0.00	25.03
Ti_2C	2	0	0	1	107.81	88.86	0.00	0.00	11.14
TiC	1	0	0	1	59.91	79.95	0.00	0.00	20.05
Ti_3Si	3	0	1	0	171.79	83.65	0.00	16.35	0.00
Ti_5Si_3	5	0	3	0	323.77	73.97	0.00	26.03	0.00
Ti_6Si_5	6	0	5	0	427.85	67.17	0.00	32.83	0.00
$TiSi$	1	0	1	0	75.99	63.03	0.00	36.97	0.00
$TiSi_2$	1	0	2	0	104.08	46.02	0.00	53.98	0.00
Ti_3Al	3	1	0	0	170.68	84.19	15.81	0.00	0.00
$TiAl$	1	1	0	0	74.88	63.97	36.03	0.00	0.00
Ti_2Al_5	2	5	0	0	230.70	41.53	58.47	0.00	0.00
$TiAl_2$	1	2	0	0	101.86	47.03	52.97	0.00	0.00
$TiAl_3$	1	3	0	0	128.84	37.18	62.82	0.00	0.00
Al_8SiC_7	0	8	1	7	328.00	0.00	65.80	8.56	25.63
Al_4SiC_4	0	4	1	4	184.05	0.00	58.64	15.26	26.10
$Al_4Si_6C_5$	0	4	6	5	336.51	0.00	32.07	50.08	17.84
Ti_2AlC	2	1	0	1	134.79	71.07	20.02	0.00	8.91
Ti_3AlC	3	1	0	1	182.69	78.66	14.77	0.00	6.57